

# Optimization of Injection in COSY

by  
Beñat Alberdi Esuain

A thesis submitted in partial fulfillment for the  
degree of Master of Science in Physics

in the

Physics Institute III B  
Faculty of Mathematics, Computer Science and Natural Sciences, RWTH Aachen University

Supervised by  
Prof. Dr. Jörg Pretz  
and  
Prof. Dr. Christopher Wiebusch

October 29, 2019



# Abstract

The Cooler Synchrotron (COSY) is a particle accelerator and storage ring operated by the Institute for Nuclear Physics (IKP) at Forschungszentrum Jülich. The facility provides polarized and unpolarized beam sources, a cyclotron, an injection beam line and the synchrotron itself, which besides many other features contains electron and stochastic cooling systems. The injection beam line of COSY has been injecting 45 MeV proton and 76 MeV deuteron beams from the cyclotron into the ring since 1991. The optimization of the injection is done by hand and, therefore, the opportunity for improvement is substantial. Currently, a new approach is being developed in order to make this process of optimization more effective.

The main objective is to rely on a thoughtful study of the injection process and simulation tools to set the injection beam line parameters in order to achieve desirable results and match the synchrotron's properties at injection. The different necessary steps to reach this goal are discussed. The process includes the characterization of the beam in the injection beam line, an analysis of the injection beam line lattice and the optimization of its sections using the Bmad software, the calculation of its main parameters and, finally, the matching of the desired ones at injection.

In the end, the obtained results are shown and the conclusions are presented. The work finishes with an outlook which describes the possible steps to take in any future development related to the injection process in COSY.



# Contents

<b>1</b>	<b>Introduction</b>	<b>1</b>
1.1	Overview . . . . .	1
1.2	Motivation . . . . .	1
1.3	Electric Dipole Moments (EDMs) . . . . .	2
1.3.1	Experimental Method . . . . .	4
1.4	Facility . . . . .	5
1.4.1	Sources and Cyclotron . . . . .	6
1.4.2	Injection Beam Line . . . . .	9
1.4.3	COSY . . . . .	10
1.5	Software . . . . .	11
<b>2</b>	<b>Basic Concepts of Accelerator Physics</b>	<b>13</b>
2.1	Coordinate System . . . . .	13
2.2	Charged Particle Dynamics . . . . .	14
2.2.1	Transfer Matrix Formalism . . . . .	16
2.2.2	Beta Function and Emittance . . . . .	19
2.2.3	Periodic Magnetic Structure and Tune . . . . .	21
2.2.4	Local Orbit Bump . . . . .	23
2.3	Charge-exchange Injection . . . . .	25
2.3.1	Injection in COSY . . . . .	27
<b>3</b>	<b>Injection Beam Line Optimization</b>	<b>33</b>
3.1	Beam Characterization in the IBL . . . . .	33
3.1.1	Emittance Measurement Using Quadrupole Scan Method . . . . .	33
3.1.2	Emittance Measurement Using the Slit Scan Method . . . . .	39
3.2	Twiss Parameters and Momentum . . . . .	44
3.3	Quadrupole Optimization . . . . .	47
3.3.1	Optimization . . . . .	48
<b>4</b>	<b>Injection Optimization in COSY</b>	<b>55</b>
4.1	Injection Dipole and Beam Steering . . . . .	55
4.1.1	Steerer Calibration in the IBL . . . . .	57
4.2	Stripping Foil . . . . .	58
4.3	COSY Orbit and Local Bump . . . . .	59
4.3.1	Injection Orbit Bump . . . . .	61
4.4	COSY Acceptance . . . . .	64

<b>5</b>	<b>Results</b>	<b>67</b>
5.1	Phase Space Filling . . . . .	67
5.1.1	Matching of the Twiss Parameters . . . . .	67
5.2	Model Testing . . . . .	69
5.2.1	Injection Optimization . . . . .	72
5.3	Outlook . . . . .	75

# Introduction

## 1.1 Overview

The goal of this work is to analyze and optimize the injection of particles in the Cooler Synchrotron (COSY). This involves both simulations and experimental work. Having more particles in the beam leads to increased statistics and, hence, an optimized time and cost efficiency. The increase of the number of particles (beam intensity) and beam quality in the ring would be beneficial for the internal and external experiments. This work has been carried out within the Jülich Electric Dipole moment Investigation (JEDI) collaboration framework, which is trying to measure the electric dipole moment of charged particles.

This work is structured in 4 chapters and a conclusion. The present chapter, the introduction, is the first one. Here the motivation to carry out the work is given, together with a general overview of the work of JEDI and the COSY facility. Chapter 2 presents the theoretical background necessary to understand the work. The next two chapters, 3 and 4, are about the work that has been carried out in this thesis to understand and optimize the injection. The structure of those chapters follows the stream of particles from the cyclotron to the ring. Finally, the results and conclusions are presented in a separated final chapter.

## 1.2 Motivation

COSY was built in the 1990s in order to provide light ion experiment possibilities to the medium energy particle physics community. It was designed and built including a stochastic cooling system, hence its name: the Cooler Synchrotron. In later times, two electron coolers for different energies have been added. Those systems give the possibility to shrink the beam phase space in a process known as cooling. Even if the use of COSY for heavier ions than deuterons was planned, this was early canceled in favor of GSI in Darmstadt. However, COSY has constantly delivered polarized and unpolarized proton and deuteron beams of up to  $3.7\text{GeV}/c$  momenta during more than 20 years. Some of the experiments carried out in COSY during this time are the WASA [1] and ANKE [2] internal experiments and TOF [3] external experiment.

Currently, COSY still provides a competent facility for the experimental particle physics community, but upgrades are needed to continue being so in the near future. One of this important upgrades is the increase of beam intensity and quality.

Nowadays as an average value  $10^{10}$  particles are accelerated in each cycle in COSY. Nevertheless, the space charge limit sets an upper bound of  $2 \times 10^{11}$  protons in the storage ring [4], an order of magnitude larger than current values. In the year 2003 a big effort was carried out in the whole facility (starting from the source, going through the source beam line, cyclotron and injection beam line and finishing with the synchrotron itself) to improve the injection of particles into the ring. That effort resulted in the highest current achieved in COSY until now, but it also required a lot of effort in optimizing every system along the stream of particles, so it is not considered a practical approach.

It is known that one of the limiting factors for intensity in the ring is the injection of particles from JULIC to COSY. In an routine experiment the injection process does not surpass 20% of efficiency (meaning that less than 20% of the particles at the end of the transfer line are injected and stored in the ring) and it is usually closer to be of around 15%.

The JEDI collaboration bases its precursor experiments for a future Electric Dipole Moment (EDM) measurement in COSY. If measured successfully, it would be a breakthrough specially for particle physics, but also for the general understanding of the universe. Thus, the possibilities are highly exciting. These precursor experiments use polarized deuteron beams, for which the intensity in the ring is even smaller than with unpolarized beams. The lower the intensity the lower the statistics, so the longer the time needed to achieve the same results. The intention to increase cost and time efficiency in those experiments (it would also be beneficial for others) has pushed the collaboration to make an effort to study and optimize the particle injection into the ring.

### 1.3 Electric Dipole Moments (EDMs)

The origin of matter is one of the great mysteries in physics. It is assumed that the physics that governs the universe today is the same as at the time the first particles were created. This leads to the prediction that the same amounts of matter and antimatter were produced at the Big Bang, resulting in a baryonic number equal to zero (see Eq. 1.1). However, all the experimental evidence available seems to indicate that the observable universe contains mostly matter and very few antimatter. In other words, a non-zero positive baryonic number. The baryonic number is given by

$$B = \frac{1}{3} (n_q - n_{\bar{q}}), \quad (1.1)$$

where  $n_q$  and  $n_{\bar{q}}$  represent the number of quarks and antiquarks respectively. The asymmetry between the baryon (matter) and antibaryon (antimatter) numbers in the known universe can be quantified experimentally in different ways and consistently yields a result of [5]

$$\eta = \frac{n_B - n_{\bar{B}}}{n_\gamma} \approx 10^{-10}. \quad (1.2)$$

In order to explain this imbalance, more matter than antimatter must have been created at some point. This baryonic asymmetry is believed to have happened during

the baryogenesis, a process that took place in the early universe. Then, at the time of annihilating with each other the imbalance between matter and antimatter would have resulted in some matter being unable to react with antimatter, thus surviving until our times. This is an indicator that not all the physical laws act the same way with both, something neither the standard model of particle physics or the theory of general relativity provides a sufficient explanation for. There must be some process which favors matter over antimatter. Those processes would exist provided that the three ‘Sakharov conditions’ are met[6]:

1. Baryon number violation.
2. CP symmetry violation.
3. Interactions out of thermal equilibrium.

Among these conditions, the CP violation could be explained by the existence of a permanent electric dipole moment (EDM) in fundamental or integer spin particles. If existing, the permanent EDM would be a fundamental property of those particles and it would be caused by the separation of the center of mass of positive and negative charges inside them. Such separation would break both parity (P) and time (T) invariance (see Figure 1.1) and, assuming that the CPT symmetry is conserved, this would lead to a CP violation. This would cause the matter and antimatter to decay at different decay rates, providing a possible explanation for matter-antimatter asymmetry as observed today.

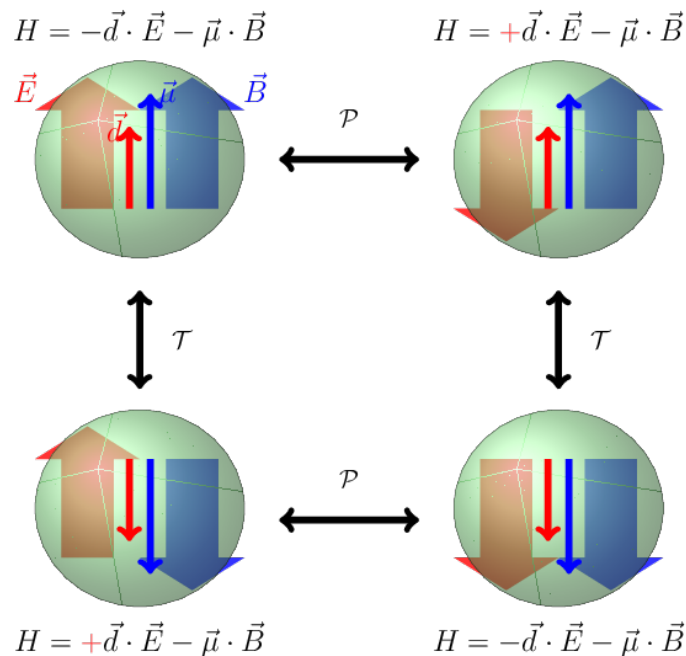


Figure 1.1: Parity ( $P$ ) and time reversal ( $\tau$ ) transformation of a Hamiltonian with an EDM and magnetic moment under  $\mathbf{E}$  and  $\mathbf{B}$  fields. It can be seen that if any of the states is taken as a starting point and then a parity operator and a time reversal operator are applied consecutively (the order does not matter), the final state of the Hamiltonian is different than the initial one.

The JEDI (Jülich Electric Dipole moment Investigation) collaboration at Forschungszentrum Jülich was born with the goal of measuring the EDM of charged hadrons, for which there are not measurements yet. Between the different integer spin particles, the use of charged hadrons provides certain advantages compared to the use of neutrons for example. The lifetime of charged hadrons like protons and deuterons is longer than the one of neutrons. In addition, charged particles can be accelerated and guided using electromagnetic fields. The measurement of an EDM in a single particle is not enough to account for the amount of CP violation necessary to get the current matter-antimatter asymmetry, so the measurement of charged and neutral particle's EDMs are complementary.

### 1.3.1 Experimental Method

The basics of an EDM measurement in any kind of particle is the interaction of an electromagnetic fields  $\mathbf{E}$  and  $\mathbf{B}$  with the electric dipole  $\mathbf{d}$ . If existing, this electric dipole is oriented in the same axis as the spin vector, because this is the only defined axis for a particle. Under the influence of electromagnetic fields the spin vector experiences a torque resulting in a change of its direction. Assuming that the particle also contains a magnetic moment  $\boldsymbol{\mu} = 2(G + 1)\frac{e\hbar}{2m}\mathbf{S}$  (being  $G = (g - 2)/2$  the anomalous g-factor), the evolution of the spin vector for a particle under the influence of electromagnetic fields is described by the Thomas-BMT equation [7][8] (its simplified form where  $\mathbf{v} \cdot \mathbf{B} = \mathbf{v} \cdot \mathbf{E} = 0$  is assumed):

$$\begin{aligned} \frac{d\mathbf{S}}{dt} &= \mathbf{S} \times \boldsymbol{\Omega} \quad \text{with} \\ \boldsymbol{\Omega} &= \frac{e\hbar}{mc} \left[ G\mathbf{B} + \left( G - \frac{1}{\gamma^2 - 1} \right) \mathbf{E} \times \mathbf{v} + \frac{1}{2}\eta(\mathbf{E} + \mathbf{v} \times \mathbf{B}) \right]. \end{aligned} \quad (1.3)$$

Here  $\mathbf{B}$  and  $\mathbf{E}$  represent the magnetic and electric fields in the laboratory frame. Furthermore, the dimensionless factor  $\eta$  has been introduced using the relation  $\mathbf{d} = \eta\frac{e\hbar}{2mc}\mathbf{S}$ . Using 1.3 to analyze the spin vector behavior in a storage ring several cases have to be considered [9]:

- Pure electric field: Using a ring without any magnetic field ( $\mathbf{B}=0$ ) and also adding the condition that the term  $\left( G - \frac{1}{\gamma^2 - 1} \right)$  cancels, Eq. 1.3 simplifies to:

$$\frac{d\mathbf{S}}{dt} = \frac{e\hbar\eta}{2mc}\mathbf{S} \times \mathbf{E}. \quad (1.4)$$

The condition  $G = \frac{1}{\gamma^2 - 1}$  can only happen for particles with  $G > 0$ . This is the case of the proton with the ‘magic’ momentum:  $p_{\text{magic}} = 0.7 \text{ GeV}$ . If horizontally polarized particles with an electric dipole are injected into a storage ring, an EDM would cause a vertical polarization build-up that could be detected.

- Combined electric and magnetic fields: In case of having both electric and magnetic fields the terms including the factor  $G$  can be canceled if

$$G\mathbf{B} + \left( G - \frac{1}{\gamma^2 - 1} \right) \mathbf{E} \times \mathbf{v} = 0$$

is fulfilled. This can happen for particles with any  $G$  value. Such a ring is under consideration in the JEDI collaboration [9].

- Pure magnetic field: Here the electric field is zero and therefore Eq. 1.3 is reduced to

$$\frac{d\mathbf{S}}{dt} = \frac{e\hbar}{mc}\mathbf{S} \times \left( G\mathbf{B} + \frac{1}{2}\eta(\mathbf{v} \times \mathbf{B}) \right). \quad (1.5)$$

In this case the polarization build-up because of an EDM is difficult to detect. The polarization precession in the horizontal plane caused by the term proportional to  $G$  makes the spin projection to be parallel to the momentum 50% of the time and antiparallel the other 50%. Given the electric fields seen by the particle in its rest frame due to the magnetic fields in the laboratory, the polarization build up in the vertical direction caused by the EDM is canceled. However, the symmetry of the projection of the polarization in the momentum direction can be broken using a ‘magic Wien filter’ with the proper frequency. Such an option is being studied by JEDI as an possible application of the currently existing COSY facility.

Thus, for any of the previously mentioned cases, the experimental method consists on injecting horizontally polarized beams in a storage ring and measuring the polarization build up in the vertical plane. The Cooler Synchrotron (COSY) is a purely magnetic synchrotron located in Forzschungszentrum Jülich. This ring is used for the precursor experiments for the EDM measurement. The aim is to later continue with a prototype ring and finally in a ring specially designed for this purpose. In the case of JEDI deuterons are currently used, but there are plans to also include protons in the future.

## 1.4 Facility

The facility is not only composed by the ring COSY. It has different sections, each one with its own purpose. The  $\text{H}^-$  and  $\text{D}^-$  negative ions are first extracted in the sources and then guided to the cyclotron by the Source Beam Line (SBL). The source is different for polarized and unpolarized particles, as the production of polarized beams requires a small collider. Once in the cyclotron, the beams are accelerated up to their injection kinetic energy, which is nominally 45 MeV for  $\text{H}^-$  ions and 76 MeV for  $\text{D}^-$  ions. Then, they are driven through the Injection Beam Line (IBL) and injected into COSY using a charge-exchange injection system.

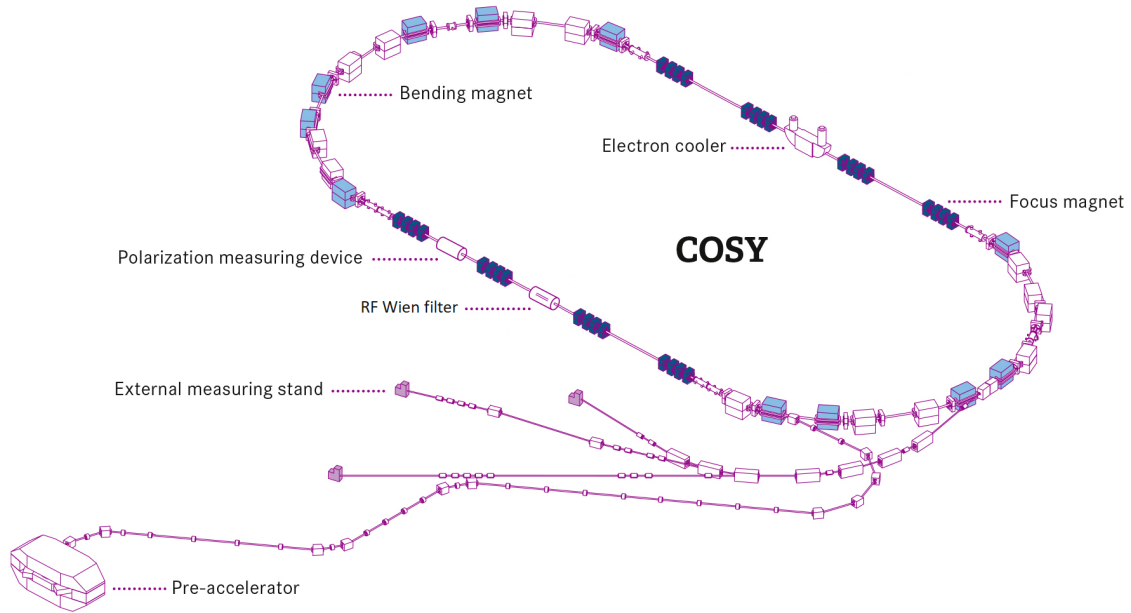


Figure 1.2: Sketch of the full facility excluding the particle source and the transfer line connecting it to the cyclotron, which are both located under it. The cyclotron is called ‘Pre-accelerator’ in this figure.

The facility plane is shown in Figure 1.2. In the following sections this facility plane is dissected and explained in three separated parts for simplicity. The explanations will not go too deep, as it would take very long to explain every section in detail. From now on the name COSY is used only to refer to the synchrotron ring itself, even if it is usually used to denote the whole facility complex. In addition, it is important to keep in mind the nature of the particles in each part of the ensemble. The particles which are extracted from the source, pre-accelerated in the cyclotron and guided to COSY using the IBL are negative charged particles ( $H^-$  or  $D^-$  ions). However, when they are injected in COSY the charge-exchange injection system stripes their electrons, so at the end positive charged particles (protons or deuterons) are accelerated and stored in the ring.

The main components of the accelerator complex are the specialized ion sources, an isochronous cyclotron acting as a pre-accelerator, the approximately 100 m long transfer line from the cyclotron to the ring and the cooler synchrotron itself, which is 184 m long in circumference [10]. Three extraction beam lines serving external experimental areas are also present, but they are not of interest in this work.

### 1.4.1 Sources and Cyclotron

The first stage of the journey of the particles takes place in the beam source. Three specialized ion sources are available, two for unpolarized beams and one for polarized beams. Those sources are shown in Figure 1.3. The operation as an injector in COSY requires beam pulsing with a maximum repetition rate of 0.5 Hz and a macro-pulse duration of 10 to 20 ms. Almost all cyclotron systems operate continuously and the macro-pulsing is generated by switching the extraction voltage for the ion sources. If required, there is a beam chopper in the beam line which can

be used for micro-pulsing in order to reduce the intensity of the beam before it enters the cyclotron. The continuous beams are then bunched by a double gap buncher with sinusoidal voltage (located just below the cyclotron). This matches them to the RF-phase acceptance of the cyclotron. The energy of the particles from the source is approximately 4.5 keV for  $\text{H}^-$  and 7.6 keV for  $\text{D}^-$  ions [11].

The IBA and AEA sources both provide unpolarized  $\text{H}^-$  and  $\text{D}^-$  ions. Both are industrial grade sources and the names come from the companies IBA, Louvain-La-Neuve (Belgium), and AEA, Culham (England). Those two are ‘multi-cusp’ type sources and can be operated independently. They were brought into operation in 1996 and they are able to provide over 300  $\mu\text{A}$  beams in pulsed operation [12]. Before that  $\text{H}_2^+$  beams were used, but the source is no longer operational.

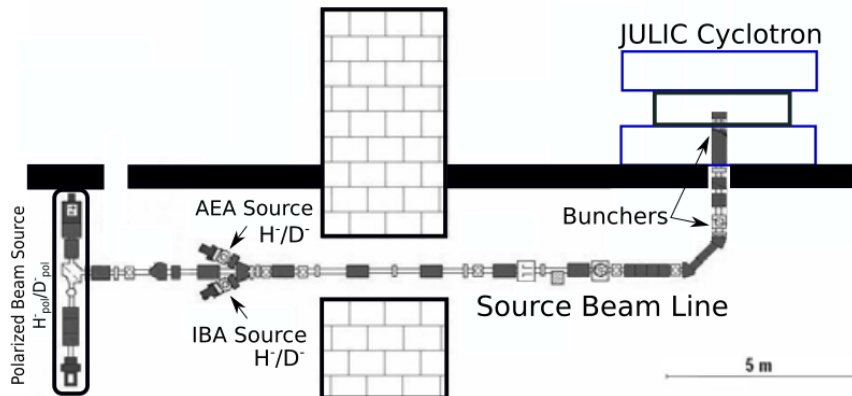


Figure 1.3: The three ion sources, the transfer line from them to the cyclotron and the JULIC cyclotron are shown here. The sources are located in a chamber beneath the cyclotron.

The polarized beam is provided by a colliding beam type source, proposed by Haeberli in 1968 [13]. This source was built under a collaboration of three different groups from Bonn, Erlanger and Cologne universities [14]. It uses the reaction



where deuterium ( $\tilde{\text{D}}^0$ ) can also be used instead of the hydrogen ( $\tilde{\text{H}}^0$ ). An intense neutralized cesium beam is made to collide with the ground state nuclear polarized hydrogen and a charge-exchange process takes place. The resulting polarized ion beam is extracted using a dipole magnet. A sketch of this source is shown in Figure 1.4. It routinely provides a 20  $\mu\text{A}$  beam to the cyclotron, but even if this intensity is lower than for the unpolarized sources, its phase space emittance (a concept which is explained in Sec. 2) is smaller. Polarization levels of  $P > 80\%$  have been measured at COSY.

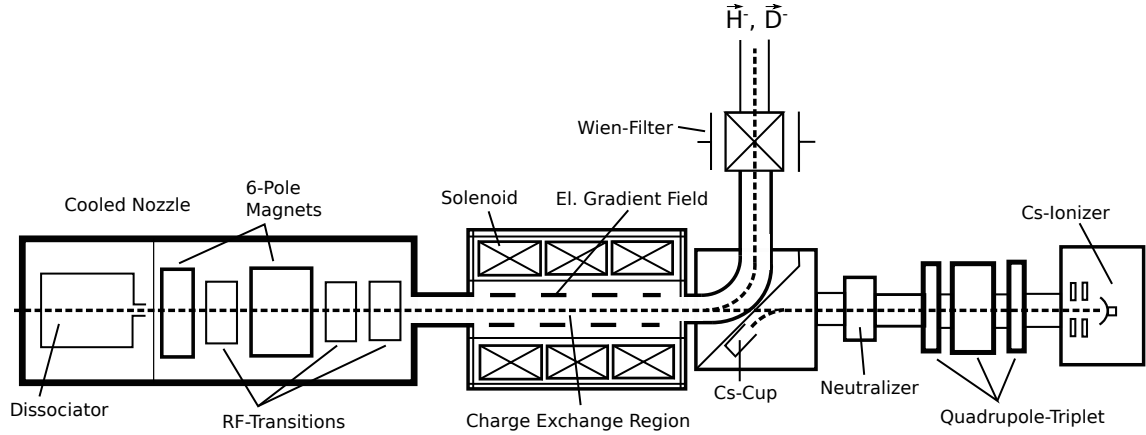
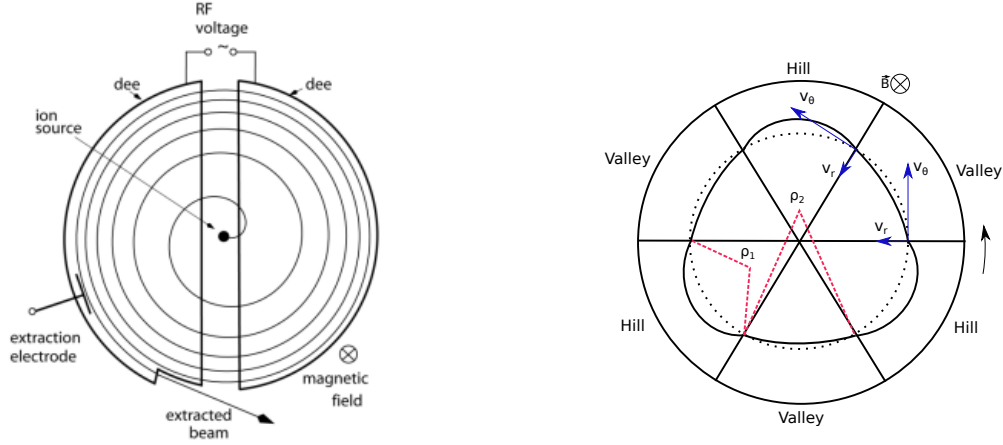


Figure 1.4: The polarized source sketch. The fast  $\text{Cs}^0$  beam comes from the right to the left and the cold polarized  $\vec{\text{H}}^0$  atoms come from the left to the right. Both beams collide at the charge-exchange region and the reaction in Eq. 1.6 takes place. The polarized ion beam is then bent in the reflection chamber and extracted from the source.

The ions extracted from the source are guided by the SBL to the Juelich Light Ion Cyclotron (JULIC). The beam line contains diagnostic systems as Faraday Cups for measuring the beam intensity. These cups are also used as beam stoppers. JULIC is responsible to accelerate the ions up to their injection energies to COSY: 45 MeV and 76 MeV for  $\text{H}^-$  and  $\text{D}^-$  beams respectively. It is an isochronous cyclotron. It has been operational for nuclear physics experiments since 1968, but was refurbished and adapted to work as a pre-accelerator for COSY in 1990-1992. Nevertheless, it is still well suited to perform nuclear physics and irradiation experiments by itself.

Cyclotrons were the first kind of particle accelerators, designed by E. O. Lawrence in 1929–1930. A cyclotron accelerates charged particles outwards from the center along a spiral path. The particles are accelerated by a RF electric field between the magnetic regions and kept in the spiral path using magnetic fields. The working principle of a classic cyclotron can be seen in Fig. 1.5a. The acceleration region lays between the capacitive electrodes known as ‘dees’. It is in these electrodes where the magnetic fields bend the trajectory of the particles. Each time the particle crosses the region between the dees, the electric field polarity changes so that those particles always experience an accelerating force [17].

In the case of a isochronous cyclotron, the particle always takes the same time to travel one loop, so it always arrives at the same RF phase to the accelerating gap. Furthermore, JULIC is a separated sector cyclotron, where the shape of the cyclotron poles itself is used to horizontally focus the beam and compensate the relativistic mass increase [18] and the vertical orbit instability. The particles do not longer travel in circular orbits, as is seen in Fig. 1.5b, but instead experience smaller bending forces in the valleys and stronger bending forces in the hills. The electric field RF used for accelerating the charged particles is known as cyclotron frequency.



(a) Classic 'dee' cyclotron.

(b) Isochronous separated sector cyclotron.

Figure 1.5: Comparison between a classic cyclotron and a separated sector cyclotron.

The transmission through the JULIC cyclotron is of  $\sim 5\%$  for unpolarized beams and  $\sim 15\%$  for polarized ones. In routine operation extracted intensities of  $10 \mu\text{A}$  and  $1 \mu\text{A}$  can be achieved for those beams respectively [16]. The diagnostic systems in JULIC make it possible to measure the beam intensity depending on the cyclotron radius. After acceleration, the particles are extracted and injected into the IBL in  $10 - 20 \text{ ms}$  macro-pulses.

### 1.4.2 Injection Beam Line

The IBL is a  $94 \text{ m}$  long transfer line. It is composed of 8 different sections, each of them with a different purpose. The detailed explanation for each of the sections is given later in Sec. 3. The full IBL contains 42 quadrupole magnets to focus, 12 dipole magnets to bend and 14 steerer magnets to steer the beam. The magnetic elements are powered in groups, with 19 independent power supplies. It was built by SIEMENS in 1992.

There are several Faraday Cups to measure beam intensity along the IBL, the most important ones being the one at the beginning to measure the intensity extracted from the cyclotron and the one at the end to measure the injected intensity at COSY. Most of the beam diagnostics in the IBL is based on the readout of profile grids, located as pairs for both planes at 8 locations along the beam line (beginning of each section). Each grid consists of 30 wires (wire diameter  $0.1 \text{ mm}$ , distance  $1.5 \text{ mm}$ ). Beam viewing systems, composed of scintillating foils and cameras, are also present at the beginning and at the end of the IBL. A slit system located at the exit of the cyclotron is used for filtering the beam and measure the emittance (see Sec. 3.1.1). Finally, three phase probes make energy determination possible by time of flight measurements [21]. Usual transmission efficiency in the IBL ranges from  $70\%$  to over  $90\%$ .

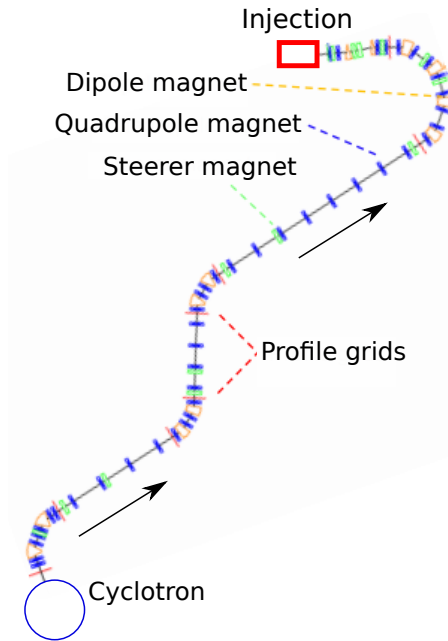


Figure 1.6: IBL sketch.

Apart from the beam transfer from the cyclotron to the ring, the IBL also takes care of matching the beam properties to the requirements at the injection point in COSY. This is achieved using the last section of the transfer line. The theory of the injection process in COSY is explained in Sec. 2.6.

### 1.4.3 COSY

COSY is a synchrotron, a type of accelerator that ramps its components at the same time as the beam gains energy, thus making the same ring useful for different energy particles. It is a race track shaped ring, with two straight sections of 40 m each. 16 quadrupole magnets are placed in each of those straight sections, grouped in four groups of four quadrupoles each [22]. Those quadrupoles make it possible to get a 1 to 1 imaging of the beam in the straight sections. This means that the beam that enters the straight section can be made to exit it with the same phase space as at the entrance. This converts the race track shaped ring into a virtual circular ring, but at the same time it gives the possibility to place internal devices such as stochastic cooling systems and RF cavities in the straight sections. Furthermore, the beam properties can also be adjusted using the same quadrupoles, thus getting favorable conditions to perform different internal experiments in the same straight sections.

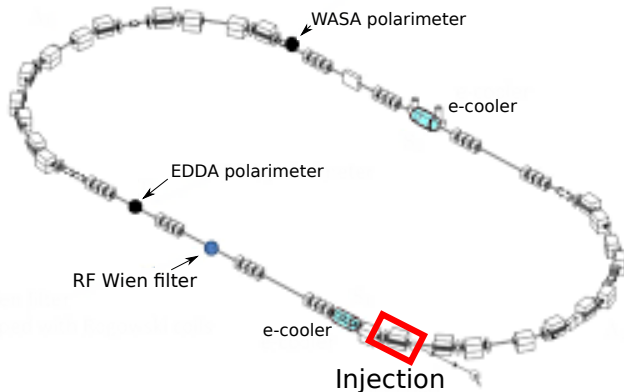


Figure 1.7: Actual status of the COSY ring, with the two electron coolers, Wien filter and EDDA polarimeter. The injection point is marked with a red rectangle.

The arc sections have a length of 52 m each and are composed of three repeated cells (magnet combinations), mirror symmetric themselves. Each of those half-cell sections has the structure quadrupole-dipole-quadrupole-dipole, in which the quadrupole polarities can be changed. This makes the arc six-fold symmetric. Stripping injection is performed at the end of one of these arcs (see Figure 1.7). Furthermore, COSY also contains sextupoles for chromaticity correction. A total of 18 sextupoles are found in the ring and their configuration affects the spin decoherence time, an important magnitude for experiments requiring a long lived polarized beam such as the precursor experiments for the EDM measurement within the JEDI collaboration.

All the components of the accelerator complex, starting from the source to the final ring, work under vacuum conditions. For proper experimental conditions a vacuum pressure of around  $10^{-10}$ - $10^{-11}$  mbar is needed in COSY, but this requirement is softer in the IBL where the pressure has to be below  $10^{-7}$  mbar. The shape of the vacuum chamber is rectangular in the arcs and circular in the straight sections. COSY also contains 29 Beam Position Monitors (BPM) distributed along the ring. These BPMs make it possible to measure the beam orbit. Shottky pick-ups for revolution frequency, tune and chromaticity measurements are present, together with a Ionization Profile Monitor to observe the beam profile. Viewer systems for directly observing the beam are placed in critical locations such as the stripping foil [23].

## 1.5 Software

To finish this chapter an small introduction is given for the software used to perform calculations and simulations. All the tools presented here are open source softwares.

Bmad (also known as ‘Baby MAD’) is a tool for relativistic charged-particle simulations in high energy accelerators and storage rings. Bmad provides a open source library of subroutines which gives the opportunity to calculate the beam optics [24] by taking a lattice (magnetic structure of an accelerator) as an input. Bmad has been

developed at Cornell University's Laboratory for Elementary Particle Physics and has been in use since 1996. It is written in Fortran and it has been selected among other similar software because it allows to study both single and multi-particle dynamics along any beam line. Optimization algorithms are included in the library. In addition, in Bmad is possible to track particles using specifically designed codes. It is developed in a modular, object-oriented structure to maximize flexibility.

In addition, for some tasks during this work the interaction between particles and matter has been taken into account. This is the case when the interaction of the beam with the stripping foil is studied. GEANT4 [25] software is used for this purpose. GEANT4 is a toolkit to simulate the passage of particles through matter. It is a software mainly developed at CERN (*Conseil Européen pour la Recherche Nucléaire*) and it provides all the necessary tools to simulate and at the same time analyze the beam-foil interaction.

Finally, Python is used as the working horse software to analyze the data gathered during the many experimental incursions into COSY. It is also used to produce many of the plots in this work.

# Basic Concepts of Accelerator Physics

In this chapter the theoretical knowledge necessary to understand the rest of the work is presented. It covers the basics for accelerator optics and beam dynamics. A special emphasis is placed in the process of injection. For a deeper understanding of accelerator physics many textbooks are available, e. g. [26] [27] [28].

## 2.1 Coordinate System

An accelerator is an ensemble of elements producing magnetic and electric fields to accelerate and guide particles. It is usually a very complex structure, as apart from the accelerating and guiding equipment many more components are needed for vacuum production, diagnostics and control.

The evolution of a particle under electromagnetic forces can be described and studied by Hamiltonian formalism. The choice of the particular coordinate system does not affect the physical results, but the pursuit of a solution can be mathematically much easier in one system than in another. There are no symmetries around a point or an axis in an accelerator which would make the use of polar or cylindrical coordinates favorable. Instead, there are many elements aligned in a ‘straight’ line, which is called beam line. Most of the times those elements are not arranged according to physical reasons, but following practical considerations. This arrangement determines the ideal path or particles, defined by the physical center of those elements. This ideal trajectory is called **reference orbit**. The coordinate system used in this work is a curvilinear co-moving coordinate system. The coordinate  $z$  goes always parallel to the particles velocity, tangent to its trajectory. The coordinates  $x$  and  $y$  form the transverse plane, perpendicular to the  $z$  direction. Then,  $y$  is defined as the vertical coordinate, pointing upwards. In this configuration the last coordinate  $x$  has to be pointing to the left when one looks in the direction of the particles. This coordinate system is called the Frenet-Serret coordinate system, and is the default system in Bmad. The individual trajectory of the particles is denoted  $s$ , where  $s_i = (x_i, y_i, z_i)$  represents any point within this trajectory.

In accelerator physics the displacement of the particles in the beam in respect to the reference particle is very small compared with the full accelerator dimensions. Therefore, each particles position and momentum at any time is given as a deviation from the reference particles position and momentum, as it can be seen in Fig. 2.1.

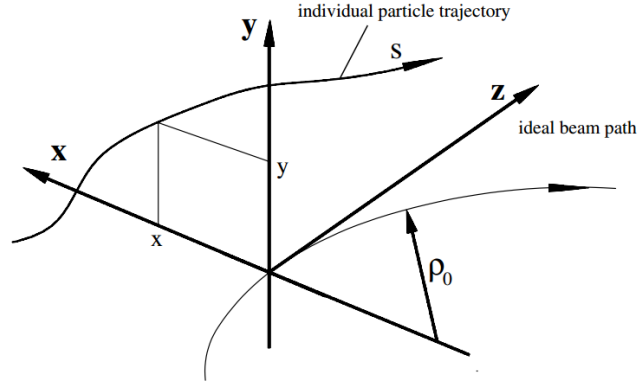


Figure 2.1: Frenet-Serret coordinate system.

## 2.2 Charged Particle Dynamics

In a ring shaped accelerator like COSY the particles trajectory is formed by numerous curves and straight sections of different lengths. Particles follow the resulting close path over and over again totaling a very long path length. However, the individual particles within a beam always have a certain momentum divergence and without taking any measurements those particles would eventually hit the vacuum pipe wall and get lost. Therefore, the particles trajectory needs to be repeatedly corrected by steering the diverging particles back to the ideal trajectory. This is done with the electromagnetic fields and the force acting over the particles in that case is the Lorentz force:

$$\mathbf{F} = e(\mathbf{E} + \mathbf{v} \times \mathbf{B}). \quad (2.1)$$

At relativistic velocities  $\mathbf{E}$  and  $\mathbf{B}$  fields have the same effect if  $\mathbf{E} = c\mathbf{B}$ . To get the same effect as a magnetic field of 1 T and electric field of  $3 \times 10^8 \text{ V m}^{-1}$  is needed. It is actually easy to obtain such magnetic fields, while electric fields of that magnitude are out of reach with ordinary technology. Hence, the bending and focusing of the particles trajectory is usually done using magnetic fields and the electric ones are only used for acceleration.

It is assumed that the particle moves in the  $z$  direction with  $\mathbf{v} = (0, 0, v_z)$  and for simplicity only transverse magnetic fields  $\mathbf{B} = (B_x, B_y, 0)$  are considered here. Then, for a particle going through a magnetic field in the horizontal plane there is a balance between the Lorentz force  $F_x = -ev_z B_y$  and the centrifugal force  $F_x = m\gamma v_z^2 / \rho$ , with  $\rho$  representing the bending radius. After using  $p = m\gamma v_z$  this gives the relation:

$$\frac{1}{\rho(x, y, z)} = \frac{e}{p} B_y(x, y, z). \quad (2.2)$$

There is also a similar expression for the vertical deflection. Now, considering that the displacements of particles in the transverse directions are very small compared to the bending radius of the particles trajectory, the magnetic field can be expanded in the near vicinity of the ideal particle path.

$$B_y(x) = B_{y0} + \frac{dB_y}{dx}x + \frac{1}{2!} \frac{d^2 B_y}{dx^2}x^2 + \frac{1}{3!} \frac{d^3 B_y}{dx^3}x^3 + \mathcal{O}(x^4). \quad (2.3)$$

If this is multiplied by  $e/p$  and the eq. 2.2 is used:

$$\begin{aligned} \frac{e}{p}B_y(x) &= \frac{e}{p}B_{y0} + \frac{dB_y}{dx}x + \frac{1}{2!}\frac{e}{p}\frac{d^2B_y}{dx^2}x^2 + \frac{1}{3!}\frac{e}{p}\frac{d^3B_y}{dx^3}x^3 + \mathcal{O}(x^4) \\ &= \frac{1}{\rho} + kx + \frac{1}{2!}mx^2 + \frac{1}{3!}ox^3 + \mathcal{O}(x^4). \end{aligned} \quad (2.4)$$

In this last equation each term represent a different multipole. The first one is the dipole term, followed by the quadrupole, sextupole, octupole,... terms. Specific magnets are used to obtain such fields. Most of the time a magnet is designed to produce a field represented by only one of the terms. Each multipole has a different effect in the particles path: the dipole field bends the trajectory, a quadrupole field focuses the beam, the sextupole is used for chromaticity correction,... When only the first two terms of eq 2.4 are used for the calculations of the accelerator properties, it is considered to be linear beam optics.

In order to understand how a particle behaves under the influence of such fields the Hamiltonian is derived and then the motion equations obtained from there. The derivation of the Hamiltonian is not shown here, as it is a long process, but it can be followed step by step in [28, p. 23-32] or [27, p. 37-39]. In Frenet-Serret coordinates, after some simplifications and development, the approximation to the Hamiltonian of a charged particle under magnetic fields looks like (the electric potential,  $\phi = 0$ , has been ignored because as it is mentioned before it is usually not used to bend the trajectory of the particles):

$$\tilde{H} \approx -p \left(1 + \frac{x}{\rho}\right) + \frac{1+x/\rho}{2p} [(p_x - eA_x)^2 + (p_y - eA_y)^2] - eA_z, \quad (2.5)$$

where  $\rho$  is the curvature radius of the reference orbit,  $\mathbf{A} = (A_x, A_y, A_z)$  is the vector potential such that  $\mathbf{B} = \nabla \times \mathbf{A}$  and  $p = \sqrt{E^2/c^2 - m^2c^2}$ . It has also been considered that  $p_x, p_y \ll p$ . From Eq. 2.5 the equations of motion for the transverse plane are derived. It is assumed that the accelerator only contains transverse magnetic fields (fields parallel to the particles velocity do not affect the trajectory), hence  $A_x = A_y = 0$ . The magnetic field can then be expressed as

$$\mathbf{B} = B_x(x, y)\hat{x} + B_y(x, y)\hat{y}, \quad (2.6)$$

where the relation to  $\mathbf{A}$  in the Frenet-Serret coordinates is given by

$$B_x = -\frac{1}{h_z} \frac{\partial A_z}{\partial y}, \quad B_y = \frac{1}{h_z} \frac{\partial A_z}{\partial x}, \quad (2.7)$$

with  $h_z = 1 + x/\rho$ . The motion equations are derived from the Hamiltonian using

$$u' = \frac{\partial \tilde{H}}{\partial p_u}, \quad p_u = -\frac{\partial \tilde{H}}{\partial u}, \quad (2.8)$$

where  $u$  stands for any of the transverse coordinates  $x$  or  $y$ . Then, using the magnetic fields from Eq. 2.7 in eq. 2.5 and applying the derivatives in Eq. 2.8:

$$\begin{cases} x'' - \frac{\rho+x}{\rho^2} = \pm \frac{B_y}{B\rho} \frac{p_0}{p} \left(1 + \frac{x}{\rho}\right)^2, \\ y'' = \mp \frac{B_x}{B\rho} \frac{p_0}{p} \left(1 + \frac{x}{\rho}\right)^2. \end{cases} \quad (2.9)$$

Here  $p$  is the individual particle momentum, while  $p_0$  is the momentum of the reference particle.  $B\rho = p_0/e$  is the magnetic rigidity, which describes the ‘resistance’ of a particle to be deflected in a magnetic field. The upper and lower signs correspond to positive and negative charged particles respectively. Then, the fields are expanded up to the first order in  $x$  and  $y$  to calculate the linear beam optics (only dipole and quadrupole fields included):

$$B_y = -B_0 + \frac{\partial B_y}{\partial x}x = \mp B_0 + B_1x, \quad B_x = \frac{\partial B_x}{\partial y}y = B_1y, \quad (2.10)$$

where  $B_0/B\rho = 1/\rho$  is the dipole field which defines the close orbit of the beam in the accelerator. Hence, Eq. 2.9 becomes:

$$\begin{cases} x'' + K_x(z)x = 0, & K_x = 1/\rho^2 \mp K_1(z), \\ y'' + K_y(z)y = 0, & K_y = \pm K_1(z). \end{cases} \quad (2.11)$$

In this last equation  $K_1(s) = B_1/B\rho$  is known as the effective focusing function. If the case of a quadrupole magnet is taken (it has no dipole field, so there is no bending) where  $1/\rho = 0$ , it can be seen that  $K_x = -K_y$ . This shows that an horizontally focusing quadrupole is vertically defocusing, while the opposite is also true. When the periodic boundary conditions of a circular accelerator are applied to Eq. 2.11 the focusing functions  $K_x$  and  $K_y$  are also periodic in  $z$ . This makes Eq. 2.11 a Hill’s equation and its solutions are described by the Floquet theorem [29].

### 2.2.1 Transfer Matrix Formalism

Now the letter  $u$  is used again to represent any of the coordinates  $x$  or  $y$ . Eq. 2.11 takes the form:

$$u'' + K_u(z)u = 0. \quad (2.12)$$

Usually accelerator components have uniform or nearly uniform magnetic fields, so the functions  $K_u(z)$  are constant in  $z$ . Taking into account that in a circular accelerator  $K_u$  has to be periodic with the periodicity  $L$  given by the orbit length ( $K_u(z + L) = K_u(z)$ ), the solution for the Hill’s equation is:

$$u(z) = \begin{cases} a \cos(\sqrt{K}z + b), & K > 0, \\ az + b, & K = 0, \\ a \cosh(\sqrt{-K}z + b), & K < 0. \end{cases} \quad (2.13)$$

The constants  $a$  and  $b$  are determined by the initial values  $u_0$  and  $u'_0$ .  $u' = \frac{du}{dz}$  represents the angle of the projection of the particles trajectory in the  $z - u$ -plane. From now on  $u'$  is used as the second axis of the  $u$  coordinate phase space instead of the momentum projection. Now, consider

$$\mathbf{u}(z) = \begin{Bmatrix} u(z) \\ u'(z) \end{Bmatrix} \quad (2.14)$$

as the betatron state vector. Then, the solution of Eq. 2.11 can be written as

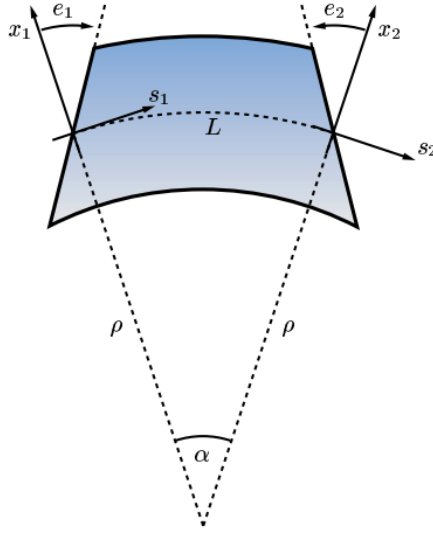


Figure 2.2: Dipole magnet with face angles  $e_1$  and  $e_2$  [24].

$$\mathbf{u}(z) = M(z|z_0)\mathbf{u}_0(z), \quad (2.15)$$

where  $M(z|z_0)$  is the betatron transfer matrix. In the case of a constant focusing function  $K$ , the transfer matrix looks like:

$$M(z|z_0) = \begin{cases} \begin{pmatrix} \cos \sqrt{K}l & \frac{1}{\sqrt{K}} \sin \sqrt{K}l \\ -\sqrt{K} \sin \sqrt{K}l & \cos \sqrt{K}l \end{pmatrix}, & K > 0 : \text{focusing quadrupole,} \\ \begin{pmatrix} 1 & l \\ 0 & 1 \end{pmatrix}, & K = 0 : \text{drift space,} \\ \begin{pmatrix} \cosh \sqrt{|K}l & \frac{1}{\sqrt{|K|}} \sinh \sqrt{|K|}l \\ -\sqrt{|K|} \sinh \sqrt{|K|}l & \cosh \sqrt{|K|}l \end{pmatrix}, & K < 0 : \text{defocusing quadrupole,} \end{cases} \quad (2.16)$$

where  $l = z - z_0$ . The matrix for a pure dipole magnet with its faces perpendicular to the trajectory of the particle is obtained by making  $K_x = 1/\rho^2$  and the result is:

$$M_x(z|z_0) = \begin{pmatrix} \cos \theta & \rho \sin \theta \\ -\frac{1}{\rho} \sin \theta & \cos \theta \end{pmatrix}, \quad (2.17)$$

where  $\theta = l/\rho$  is the bending angle and  $\rho$  is the bending radius. If the faces are not perpendicular to the beam horizontal and vertical focusing and defocusing effects appear. Those effects can be represented by using the transfer matrix

$$M_{e_1} = \begin{pmatrix} 1 & 0 & 0 & 0 \\ \frac{\tan e_1}{\rho} & 1 & 0 & 0 \\ 0 & 0 & 1 & 0 \\ 0 & 0 & -\frac{\tan e_1}{\rho} & 1 \end{pmatrix}, \quad (2.18)$$

where the angles  $e_1$  and  $e_2$  are shown in Fig. 2.2. The advantage of expressing the solution of Eq. 2.11 in matrix notation is that the solution of an interval made up

of sub-intervals is just the product of the transfer matrices of the sub-intervals. For example if  $z_1 \in (z_0, z_2)$ :

$$M(z_2|z_0) = M(z_2|z_1)M(z_1|z_0). \quad (2.19)$$

Using these matrices, particle motion can be tracked through the accelerator elements. Each component of the accelerator can be represented by a matrix as it has been shown in Eq. 2.16 and 2.17. A couple of important characteristics of such 2x2 matrices are:

- $\det M = 1$ ,
- $|\text{Trace}(M)| \leq 2$ .

These conditions come from the stability requirements of the particle motion in the accelerator and are proven in [27, p. 48-50]. The matrix  $M(z|z_0)$  only depends on the function  $K$  between  $z$  and  $z_0$ . Until now the phase spaces  $x$  and  $y$  have been treated separately. This is accurate as long as there is no coupling, which can be given for example by the existence of longitudinal fields in the accelerator (only transverse fields have been considered in the derivation of the Hamiltonian). In any case, if  $x$  and  $y$  are coupled it is necessary to use 4x4 matrices instead of 2x2 ones:

$$\begin{pmatrix} x \\ x' \\ y \\ y' \end{pmatrix} = M_{4x4}(z|z_0) \begin{pmatrix} x_0 \\ x'_0 \\ y_0 \\ y'_0 \end{pmatrix}, \quad (2.20)$$

but in the case of a decoupled system  $M_{4x4}$  reduces to

$$M_{4x4}(z|z_0) = \begin{pmatrix} M_x(z|z_0) & 0 \\ 0 & M_y(z|z_0) \end{pmatrix}, \quad (2.21)$$

with  $M_x(z|z_0)$  and  $M_y(z|z_0)$  being the 2x2 transfer matrices from before. The same logic is followed when also including the longitudinal phase space. In that case, a 6x6 matrix is necessary:

$$\begin{pmatrix} x \\ x' \\ y \\ y' \\ z \\ \frac{\Delta p}{p} \end{pmatrix} = M_{6x6}(z|z_0) \begin{pmatrix} x_0 \\ x'_0 \\ y_0 \\ y'_0 \\ z_0 \\ \frac{\Delta p}{p}|_0 \end{pmatrix}. \quad (2.22)$$

This last matrix codes all the information about the linear beam behavior in an accelerator section from  $z_0$  to  $z$ . Off momentum particles ( $\frac{\Delta p}{p} \neq 0$ ) are also considered here. The effects of the momentum deviation are neglected in drift spaces and quadrupoles (this is only an approximation, the dependence of the beam focusing on the particles momenta is a higher order correction). However, the effect caused by momentum deviation in bending dipole fields has to be taken into account and it is known as **dispersion** ( $D(z)$ ). Off-momentum particles follow dispersive trajectories in the accelerator, with a displacement in the bending plane given by  $x_D = D(z)\Delta p/p$ . This trajectories are in general not of the same length as the ideal

orbit. Then, the path length is a function of the momentum. The relation between the deviation of the path length and the momentum deviation of particles is known as **momentum compaction factor** and is given by:

$$\alpha = \frac{\Delta L/L}{\Delta p/p} = \frac{1}{L_0} \oint \frac{D(z)}{\rho(z)} dz, \quad (2.23)$$

where  $L_0$  is the ideal path length and  $\rho(z)$  is again the bending radius. This last expression is derived in [26, p. 76-77].

## 2.2.2 Beta Function and Emittance

Up to now the individual behavior of the particles through an arbitrary structure of magnets has been studied. This is not enough to understand the properties of a beam with many particles. The collective beam conduct is the decisive factor when developing a system of beam optics, so the techniques need to be extended to understand the composite beam. For this purpose it is necessary to go back to Hill's equation in its simplest form (Eq. 2.11), without taking into account any momentum deviation and making  $1/\rho = 0$ . Then  $K_x(z) = -K_1(z) = -K_y(z)$ , with  $K_1 = B_1/B\rho$  being the effective focusing. Now, Hill's equation in the horizontal plane looks like:

$$x''(z) + K_x(z)x(z) = 0. \quad (2.24)$$

The solution for this differential equation is given by [26, p. 77-78]:

$$x_i(z) = \sqrt{\epsilon_i} \sqrt{\beta(z)} \cos [\Psi(z) + \phi_i], \quad (2.25)$$

where  $\epsilon$  is a constant which is called **emittance** and  $\beta(z)$  is the **beta function**. In addition,  $\phi_i$  represents the phase for an arbitrary particle  $i$ , and the function  $\Psi(z)$  is given by:

$$\Psi(z) = \int_0^z \frac{d\sigma}{\beta(\sigma)}. \quad (2.26)$$

The separation of  $\epsilon$  and  $\beta(z)$  in Eq. 2.25 is done on an *ad hoc* basis, even if it seems mathematically arbitrary at this point. The maximum amplitude of the sinusoidal motion is given by

$$E(z) = \pm \sqrt{\epsilon\beta(z)}. \quad (2.27)$$

Now, if the derivative respect to  $z$  of Eq. 2.25 is calculated the next equation is obtained:

$$x'_i(z) = -\frac{\sqrt{\epsilon}}{\sqrt{\beta(z)}} \left[ -\frac{\beta'(z)}{2} \cos(\Psi(z) + \phi_i) + \sin(\Psi(z) + \phi_i) \right]. \quad (2.28)$$

Define  $\alpha \equiv -\beta'(z)/2$  and then combine Eq. 2.25 and Eq. 2.28 to get rid off the function  $\Psi(z)$  in the expression. If the general relation  $\cos^2 \mu + \sin^2 \mu = 1$  is also used the result gets the form:

$$\frac{x_i^2}{\beta(z)} + \left( \frac{\alpha(z)}{\sqrt{\beta(z)}} x_i + \sqrt{\beta(z)} x'_i \right)^2 = \epsilon_i. \quad (2.29)$$

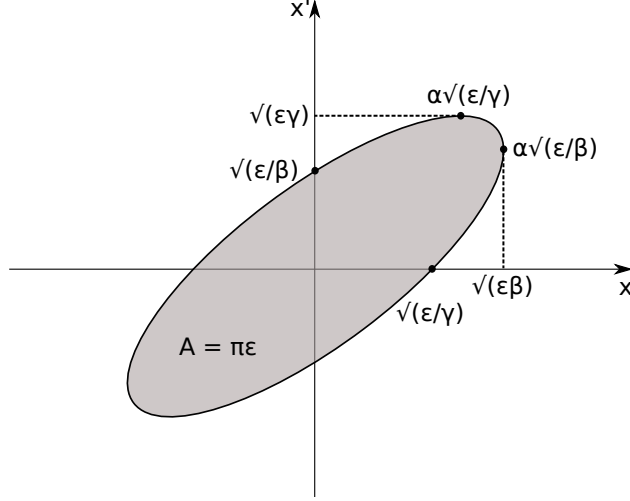


Figure 2.3: The phase space ellipse in  $x - x'$ -plane.

Finally, by defining

$$\gamma \equiv \frac{1 + \alpha^2(z)}{\beta(z)}, \quad (2.30)$$

Eq. 2.29 now looks like:

$$\gamma(z)x_i^2(z) + 2\alpha(z)x_i(z)x_i'(z) + \beta(z)x_i'^2(z) = \epsilon_i. \quad (2.31)$$

This is the general equation for an ellipse in the  $x - x'$ -plane with an area given by  $A = \pi\epsilon_i$ . So the integration constant called emittance which is first used in Eq. 2.25 now takes a new meaning: it is within a factor  $\pi$  the area of the ellipse.  $\beta$ ,  $\alpha$  and  $\gamma$  are known as the **Courant-Snyder parameters** or **twiss parameters**. Then, for a particle with certain initial conditions  $\mathbf{X}_0 = (x_0, x'_0)$  at  $z_0$ , its evolution can be tracked along the accelerator by solving Eq. 2.31 and the trajectory vector  $\mathbf{X}$  describes an ellipse in phase space. Each particles trajectory describes its own ellipse. However, as the functions  $\beta$ ,  $\alpha$  and  $\gamma$  are equal for all the particles in any position of the accelerator (they are defined by the focusing function  $K$ , which is a property of the accelerator and not of the beam) all the individual ellipses in the same position  $z$  have the same shape, but different amplitude. The amplitude depends on  $\mathbf{X}_0 = (x_0, x'_0)$ .

Up to now all calculations have been done for the  $x$  axis, but the same procedure can be followed for  $y$  and the results are identical. Every particle describes its own phase ellipse in the  $y - y'$ -plane, whose shape will depend on the focusing function  $K$  in  $y$  and its amplitude on the initial conditions  $\mathbf{Y}_0 = (y_0, y'_0)$ .

It has been shown that each particle has its own associated emittance, but there are many particles in the beam moving within different amplitude ellipses in phase space. It is not possible to measure every particle's trajectory individually, so a collective emittance of the beam is defined instead. For this purpose it is assumed that the equilibrium distribution of transverse charge density within the beam is defined by a Gaussian distribution:

$$\rho(x, y) = a \exp\left(-\frac{x^2}{2\sigma_x^2} - \frac{y^2}{2\sigma_y^2}\right). \quad (2.32)$$

In Eq. 2.32 the horizontal and vertical beam sizes are defined by  $\sigma_x$  and  $\sigma_y$ , which correspond exactly to a standard deviation on the particle distribution. Using the maximum sinusoidal amplitude shown before in Eq. 2.27 an emittance ( $\epsilon_{STD}$ ) can be assigned to all the particles which lie within one standard deviation from the beam center by the relation

$$\sigma(z) = \sqrt{\epsilon_{STD}\beta(z)} \quad (2.33)$$

for any of the two transverse coordinates. It can be calculated by using  $\epsilon_{STD} = \sigma^2/\beta(z)$ . From now on the emittance of one standard deviation is used to represent the emittance of the entire beam and it will be denoted using simply  $\epsilon$ . Eq. 2.33 now defines the **envelope** of the beam. The  $\beta(z)$  function depends on the focusing at each position  $z$ . This can be considered as a measurement of the cross section of the beam and the two signs only indicate that there is an envelope at both sides of the beam center. According to Louville's theorem [30], the phase-space distribution function is constant along the trajectories of the system, which means that it is constant in time. This theorem stands as long as the particles obey the canonical equations of motion, which is generally true in accelerators. This implies that the emittance is conserved along the accelerator. So, when  $\beta(z)$ ,  $\alpha(z)$  and  $\gamma(z)$  change along the trajectory of the beam, the ellipse shape and position change with them following Eq. 2.31, but the area of the ellipse always stays constant.

Finally, it is necessary to mention that any accelerator needs to have enough space in the transverse plane of its vacuum pipe for the beam. This defines the **geometrical acceptance** of the accelerator and it is given by the biggest ellipse that can fit in the vacuum pipe. Being  $d$  the distance from the vacuum pipe center to the walls:

$$A = \frac{d^2}{\beta}|_{min}. \quad (2.34)$$

### 2.2.3 Periodic Magnetic Structure and Tune

In closed lattice accelerators the beam sees the same magnetic structure in every revolution. Then, the focusing function is periodic, with  $K(z) = K(z + L)$ . In that case, the solution of Eq. 2.11 is the same, but this time  $\beta(z)$ ,  $\alpha(z)$  and  $\gamma(z)$  are also periodic with the same periodicity as  $K(z)$ . However, in an open lattice such as a transfer line between two accelerators, the function  $\beta(z)$  at any point  $z$  is determined by the initial values of  $\beta$ ,  $\alpha$  and  $\gamma$  at  $z_0$ .

The number of betatron oscillations (oscillations around the beam axis  $z$ ) that a particle undergoes per revolution in a closed lattice is known as **tune**. The relation between the tune and the betatron phase advance is

$$Q = \frac{\Delta\Psi}{2\pi} = \frac{1}{2\pi} \oint \frac{dz}{\beta(z)}, \quad (2.35)$$

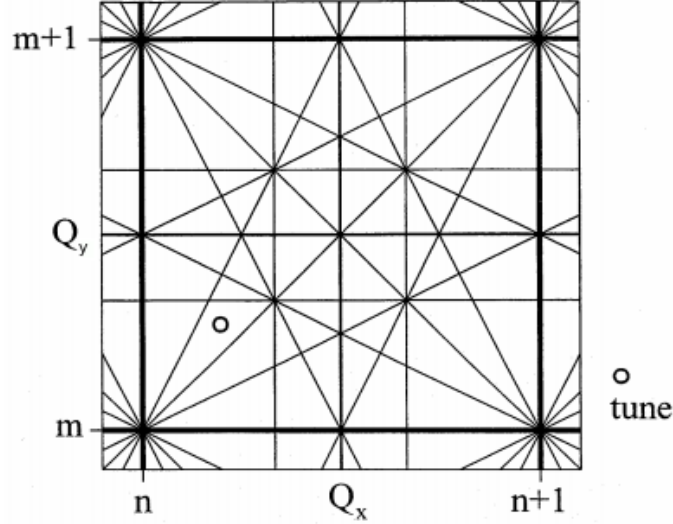


Figure 2.4: Tune diagram with  $Q_x$  in the horizontal axis and  $Q_y$  in the vertical axis. All coupled resonances up to third order are shown together with a possible working point [26, p. 112].

where  $\Delta\Psi = \Psi(z + L) - \Psi(z)$ . If  $nQ$  is an integer number for an arbitrary value of  $n$ , it means that each  $n$  revolutions the particle goes through the same position of the accelerator with the same betatron phase (which means same amplitude) and experiences the same forces. Then, the amplitude of the oscillations is enhanced until the particle is lost. This is called optical resonance. The lower the value of  $n$  is the bigger the strength of the resonance. The integer number  $n$  determines which multipole drives the resonance. Being  $p$  an arbitrary integer number:

- $Q = p \Rightarrow$  dipole,
- $2Q = p \Rightarrow$  quadrupole,
- $3Q = p \Rightarrow$  sextupole,
- $4Q = p \Rightarrow$  octupole.

However, an accelerator has two tune values:  $Q_x$  and  $Q_y$ . This makes reality even more complex. For higher orders of multipoles the betatron phases in both transverse directions are coupled and optical resonance occurs if

$$nQ_x + mQ_y = p, \quad (2.36)$$

where  $n$ ,  $m$  and  $p$  are integer numbers. These are called the coupled resonances and  $|n| + |m|$  is known as the resonance order. Therefore, choosing the proper  $Q_x$  and  $Q_y$  values is essential in an accelerator. This pair of values is called working point and has to be as far as possible from optical resonances. In Fig. 2.4 the working point is placed in a diagram together with the lines defining the solutions for Eq. 2.36. This working point can be used to compare the real accelerator and a model of it, as it is done in Chapter 5.

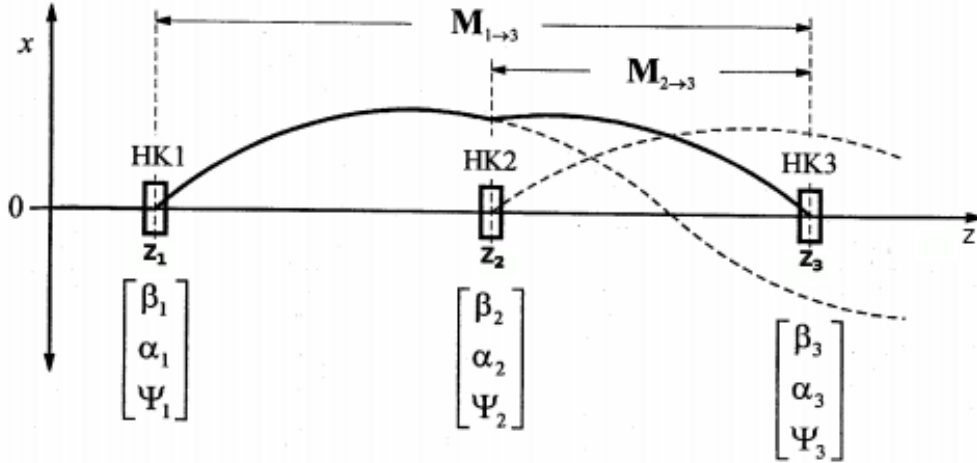


Figure 2.5: Local bump produced with the magnets HK1, HK2 and HK3. The values of the  $\beta$ ,  $\alpha$  and  $\Psi$  functions in the same positions as the magnets are also highlighted [26, p. 129].

Unfortunately, not all particles travel with the same momentum within a beam. This momentum deviation causes particles to have slightly different tunes. The spread of the tune values caused by momentum deviations is known as **chromaticity**.

## 2.2.4 Local Orbit Bump

It is often necessary to shift the beam deliberately in a certain position  $z$  of the accelerator without affecting the rest of the ring. This is called an **orbit bump**. It is always performed using small dipole magnets which are added to the existing lattice of the accelerator. Those magnets are able to kick the beam by a certain angle  $\kappa$ . In the case of COSY an horizontal orbit bump is used at injection. The magnets responsible to create such bump have the ability to increase and decrease the dipole fields very fast and are called **bumper magnets**. In theory, a local orbit bump can be performed using 2, 3 or 4 magnets. The more are used, the better the control of the orbit shift. With only two magnets the orbit bump is only possible if they are located in certain positions, determined by the lattice. With three magnets it is almost always possible to create a local orbit bump, but only the displacement at a certain point or the angle at the same point can be controlled, never both at the same time. Finally, with four magnets the displacement and angle of the bumped orbit at any position are under control. In COSY there are 3 bumper magnets available, so only the theory related to a three magnet bump is shown here. [26, p. 127-135] has a full theoretical description of the three cases.

In Fig. 2.5 the working principle of the three magnet local bump is shown. The first of the magnets, named HK1, kicks the beam out of the ideal orbit with an angle  $\kappa_1$ . Then, as a result of the focusing (remember that there are more lattice elements between the magnets, even if those are not shown in Fig. 2.5 for simplicity) the beam starts to perform oscillations around the ideal orbit. Then, it is again kicked by the second magnet HK2 and finally HK3 is responsible to bring the beam back to the ideal orbit path. Consider that the beam is originally in the ideal path when it

reaches the first magnet and then is kicked by an angle  $\kappa_1$  horizontally. The initial state is now

$$\mathbf{X}_1 = \begin{pmatrix} x_1 \\ x'_1 \end{pmatrix} = \begin{pmatrix} 0 \\ \kappa_1 \end{pmatrix}. \quad (2.37)$$

Then, the state in the position  $z_3$  of Fig. 2.5 is given by:

$$\begin{pmatrix} x_3 \\ x'_3 \end{pmatrix} = M(z_3|z_1) \begin{pmatrix} x_1 \\ x'_1 \end{pmatrix}, \quad (2.38)$$

where  $M(z_3|z_1)$  is the transfer matrix between  $z_1$  and  $z_3$ . Then, in order to be back at the ideal orbit the state of the beam at  $z_3$  has to be given by

$$\mathbf{X}_3 = \begin{pmatrix} 0 \\ -\kappa_3 \end{pmatrix} \quad (2.39)$$

and the be kicked by the last magnet HK3 by an angle  $\kappa_3$ . In addition, the magnet HK2 is located between HK1 and HK3. The effect of the kick  $\kappa_2$  at  $z_2$  to a beam traveling in the ideal orbit would be seen in  $z_3$  as:

$$\begin{pmatrix} x_3 \\ x'_3 \end{pmatrix} = M(z_3|z_2) \begin{pmatrix} 0 \\ \kappa_2 \end{pmatrix}. \quad (2.40)$$

These two corrections to the ideal orbit in the positions  $z_1$  and  $z_2$  by the magnets HK1 and HK2 respectively can be added to obtain the state in  $z_3$ , which has to be the one given in Eq. 2.39 in order to have a local bump.

$$\begin{aligned} X_3 &= M(z_3|z_1) \begin{pmatrix} 0 \\ \kappa_1 \end{pmatrix} + M(z_3|z_2) \begin{pmatrix} 0 \\ \kappa_2 \end{pmatrix} \\ &= \begin{pmatrix} a_{11} & a_{12} \\ a_{21} & a_{22} \end{pmatrix} \begin{pmatrix} 0 \\ \kappa_1 \end{pmatrix} + \begin{pmatrix} b_{11} & b_{12} \\ b_{21} & b_{22} \end{pmatrix} \begin{pmatrix} 0 \\ \kappa_2 \end{pmatrix} \\ &= \begin{pmatrix} 0 \\ -\kappa_3 \end{pmatrix}. \end{aligned} \quad (2.41)$$

Eq. 2.41 gives a system of equations from where  $\kappa_2$  and  $\kappa_3$  can be calculated as a function of  $\kappa_1$ :

$$\kappa_2 = -\frac{a_{12}}{b_{12}}\kappa_1, \quad (2.42)$$

$$\kappa_3 = -\left(a_{22} - \frac{a_{12}}{b_{12}}b_{22}\right)\kappa_1. \quad (2.43)$$

Hence, as it can be seen in Eq. 2.42 and Eq. 2.43, the necessary kicks for a local bump are only dependent on the transfer matrix elements. The transfer matrix is determined by the lattice only, so the kick strengths depend on the accelerator components and not on the beam orbit. The amplitude of the displacement can be chosen by choosing the appropriate  $\kappa_1$  value.

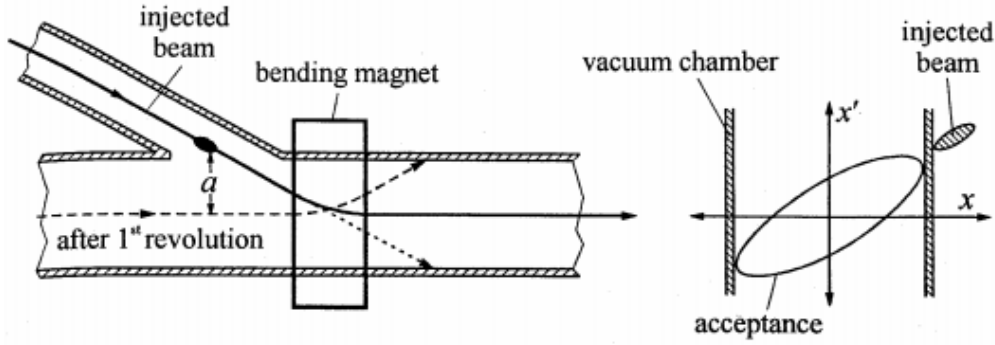


Figure 2.6: Sketch of injection process on the left. The acceptance of the accelerator together with the emittance of the injected beam on the right [26, p. 141].

## 2.3 Charge-exchange Injection

Now that the most basic concepts of beam dynamics are explained, the injection process is studied theoretically. Injection covers the final stage of the transfer of the beam from one accelerator to another, either from a linear to a circular machine or from one circular machine to another. The design aims are to achieve the transfer with little beam loss and with the minimum or defined dilution of the beam emittances. However, any particle injected outside the accelerators acceptance will hit the vacuum pipe wall at some point and will be lost. Injection can therefore be a complicated process as the injected beam has to be placed into (or at least close to) the orbit of the circular machine, without significantly disturbing the orbiting beam.

The main problem of injection is that an injected beam always lies out of the acceptance of the accelerator just before entering the vacuum chamber (see Fig. 2.6), as  $a > d$ . Without the help of a bending magnet the injected beam would eventually hit the vacuum chamber. Thus, is necessary to have such a magnet to precisely match the angle and position of the orbit. However, the magnet has to be switched off before the beam completes one revolution or it will be deflected again and hit the wall. This requires magnets which can ramp their field very fast and then decrease it again before the beam competes a revolution. This job is performed by the previously mentioned bumper magnets. Furthermore, when particles are injected they take a finite volume in phase space, given by

$$\Delta V = \Delta x \Delta x' \Delta y \Delta y' \Delta z \frac{\Delta p}{p}. \quad (2.44)$$

This leads to the main rule of injection: a particle can not be injected in the same phase space volume of an existing particle without losing the already present one.

When the emittance of the injected beam is smaller than the acceptance of the machine and the particles circulating in the accelerator do not lose energy significantly, injection can continue filling different sections of the phase space which are adjacent but separated. This is the so called 'stacking' method and is usually done with protons and heavy ions because of their low energy loss due to synchrotron radiation. It can be performed in separated injections or in a multi-turn continuous

injection. The former is the case in COSY.

A popular and effective method of injection is the charge-exchange injection method. It consists on driving negatively charged ions into an stripping foil. This stripping foil stripes the electrons from the ions and then protons (or deuterons) go into the accelerator. However, apart from stripping the electrons this foil also causes the particles to experience multiple scattering and energy losses. The analytical formula for the root mean square scattering angle in a target is given by [31, p. 644]

$$\theta_{rms} \approx \pi N \left( \frac{2zZe^2}{pv} \right)^2 \ln(204Z^{-1/3}) t, \quad (2.45)$$

where  $N$  is the number of atoms per unit volume of the target,  $z$  and  $Z$  are the charge of the projectile and the target, respectively,  $e$  the electronic charge,  $p$  and  $v$  the momentum and velocity of the projectile and  $t$  the target thickness. The mean energy loss for such a charge-exchange foil and  $0.1 \leq \beta\gamma \leq 1000$  is well described using the Bethe-Bloch formula [32, p. 447]

$$\left\langle -\frac{dE}{dx} \right\rangle = K z^2 \frac{Z}{A} \frac{1}{\beta^2} \left[ \frac{1}{2} \ln \frac{2m_e c^2 \beta^2 \gamma^2 T_{max}}{I^2} - \beta^2 - \frac{\delta(\beta\gamma)}{2} \right], \quad (2.46)$$

where

Table 2.1: Variables used in the Bethe-Bloch formula 2.46.

Symbol	Definition	Value or Unit
$K$	$4\pi N_A r_e^2 m_e c^2$	$0.307\,075 \frac{\text{MeVcm}^2}{\text{g}}$
$z$	charge number of incident particle	
$Z$	atomic number of target	
$A$	atomic mass number of target	$\frac{\text{g}}{\text{mol}}$
$\beta$	speed normalized to $c$	$\beta = \frac{v}{c}$
$m_e$	electron rest mass	511 keV
$c$	speed of light	$299.792 \frac{\text{km}}{\text{s}}$
$\gamma$	Lorentz factor	$\gamma = \frac{1}{\sqrt{1-\beta^2}}$
$T_{max}$	Maximum energy transfer to electron	eV
$I$	mean excitation energy	eV
$\delta(\beta\gamma)$	density effect correction to ionization energy loss	

This leads to a root mean square momentum deviation per passage through the foil

$$\delta_{rms} = \frac{\Delta p}{p} = \frac{\gamma}{1+\gamma} \frac{\Delta E_k}{E_k}, \quad (2.47)$$

where  $E_k$  is the kinetic energy. The effect of this two phenomena in the transverse and longitudinal emittances of the beam is studied in [33]. After  $n$  passages through the foil:

$$\epsilon_n = \epsilon_0 + \frac{n}{2} \left( \beta \theta_{rms}^2 + \frac{D^2}{\beta} \delta_{rms}^2 + \beta D'^2 \delta_{rms}^2 \right), \quad (2.48)$$

where  $\beta$  is the value of the function  $\beta(z)$ ,  $D$  is the dispersion and  $D'$  is the derivative of the dispersion at the stripping foil position. Then, the emittance of the beam

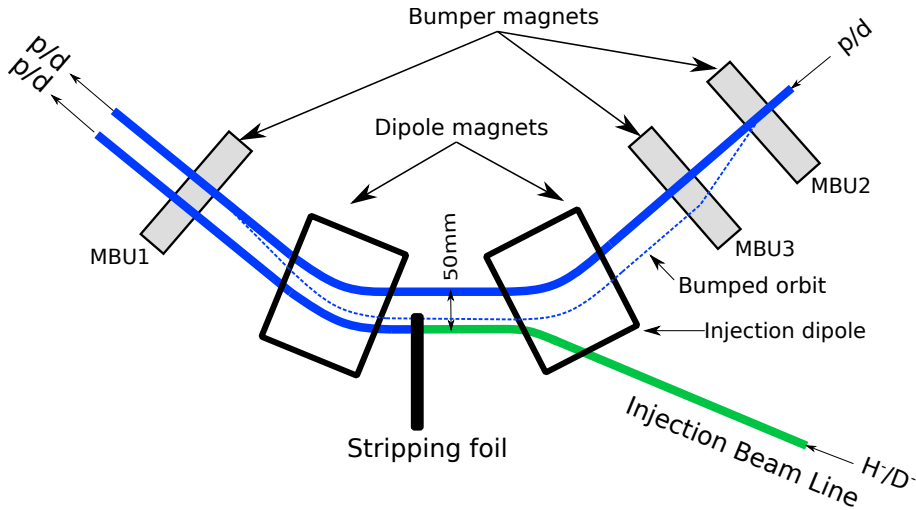


Figure 2.7: Sketch of injection in COSY. The beam coming from the IBL is shown in green color, while the beam circulating at COSY is shown in blue. After hitting the stripping foil the injected beam loses its electrons and becomes a proton/deuteron beam, hence its blue color.

hitting the stripping foil grows linearly with the number of times the beam passes through it. If the foil is then placed in the orbit of the circulating beam this can lead to a big emittance increase and, therefore, when the accelerator acceptance is surpassed by the beam emittance, to beam losses. Hence, the stripping foil is usually located at a certain offset from the ideal orbit.

### 2.3.1 Injection in COSY

As many particles as possible have to be injected in the COSY ring for optimal beam intensity. Injection is performed using a multi-turn charge-exchange method in which  $H^-$  and  $D^-$  ions coming from the cyclotron are driven into a stripping foil. COSY has around 184m in circumference. With  $\gamma$  and  $\beta$  being the relativistic  $\gamma$  factor and the normalized velocity respectively, the revolution frequency for 45 MeV protons is given by:

$$E_k = (\gamma - 1)m_{\text{proton}} = 45 \text{ MeV} \Rightarrow \gamma \approx 1.048 \Rightarrow \beta = \frac{1}{\gamma} \sqrt{\gamma^2 - 1} \approx 0.2992,$$

so

$$f_{\text{rev}} = \frac{L}{\beta c} \approx 2 \times 10^{-6} \text{ s} = 2 \mu\text{s}.$$

This means that the first particles being injected at COSY during a 20 ms injection cycle have completed around  $10^4$  revolutions by the time the last particles are injected. A very similar result is obtained for 76 MeV deuterons.

The stripping foil is made up a  $20 \mu\text{g cm}^{-2}$  deep  $C^{12}$  [34]. It is located in the same vacuum pipe but at a certain horizontal offset from the COSY nominal orbit to avoid beam losses. A sketch of the injection process is shown in Fig. 2.7.

As it can be seen in Fig. 2.7 the beam of  $H^-$  or  $D^-$  ions coming from the cyclotron (blue line) enters the injection dipole (see Fig. 2.8) from a side and it is bent to the

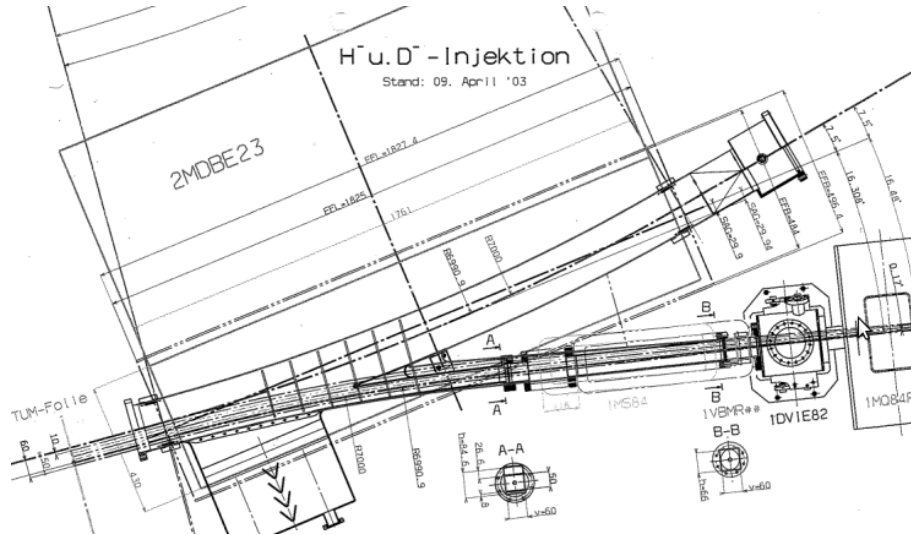


Figure 2.8: Technical drawing of the injection dipole (dipole number 23) in COSY [35].

left. On the other hand, the beam which is already circulating at COSY (remember that it is a multi-turn injection) is bent to the opposite direction, as it has the opposite charge. Therefore, both beams are placed in parallel directions. It is after this bending that the injected beam hits the stripping foil and is stripped of its electrons, but the cycling beam does not hit the stripping foil because of the horizontal offset between both beams (see Fig. 2.12). The offset between the injected and circulating beam can be controlled using the three bumper magnets. These bumper magnets distort the orbit of the circulating beam in COSY and create a local orbit bump, thus controlling the distance between both beams. The injection sequence is the following:

- The  $H^-$  (or  $D^-$ ) beam comes from the cyclotron through the IBL and enters the injection dipole, which places the injected beam parallel to the orbit in COSY, but at an horizontal nominal offset of  $\Delta x = 50$  mm, following the path towards the edge of the stripping foil.
- The orbit in COSY is horizontally bumped using the three injection bumper magnets. The orbit bump is a compensated bump, so that it does not affect the orbit outside the injection section. With this bump, the orbit is placed at the same position as the injected beam, hitting the stripping foil edge.
- The injection begins as the same time as the intensity in the bumper magnets start to decrease linearly to 0. This decrease in intensity takes the same time as the duration of the injection macro-pulse. Hence, the orbit bump is maximum when injection starts and after 20 ms the orbit is back at its original position (see Fig. 2.9).

The reduction of the bump allows the injected beam to ‘paint’ different sections of the horizontal acceptance phase space. As the orbit shifts away from the injection beam axis the injected particles are accepted into different phase space sections as seen in Fig 2.10.

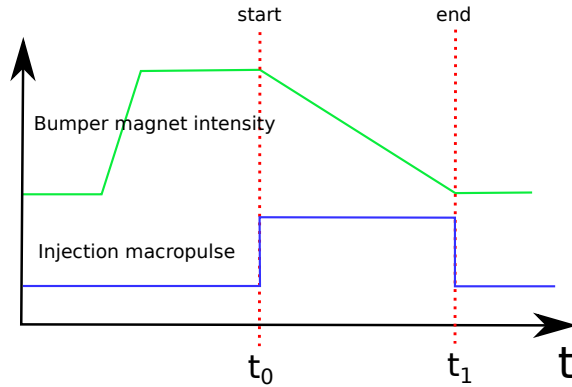


Figure 2.9: Injection macro-pulse (in blue) and the bumper magnet intensity (in green). The injection takes place from  $t_0$  to  $t_1$ , where usually  $t_1 - t_0 = 20$  ms.

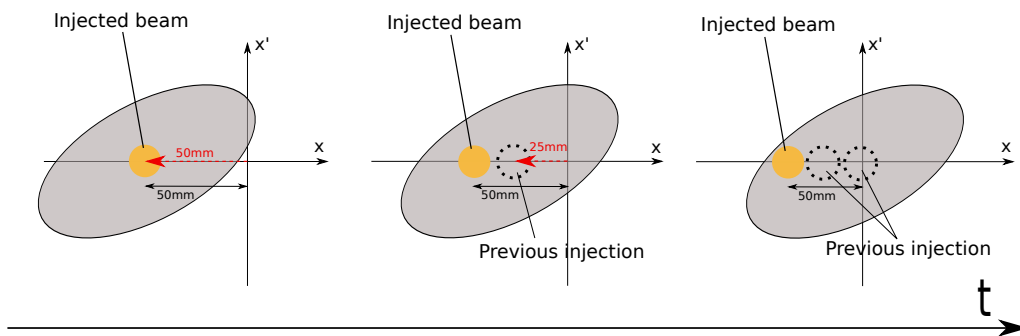


Figure 2.10: Sketch of the phase space filling process for the  $x - x'$  phase space. The gray shadow represents the acceptance of the ring. The orange shadow represents the emittance of the injected beam. The evolution of the injection process is shown from left to right, starting from the situation when the bump is maximum and the orbit matches the injected beam position and finishing at the situation when the bump has already disappeared.

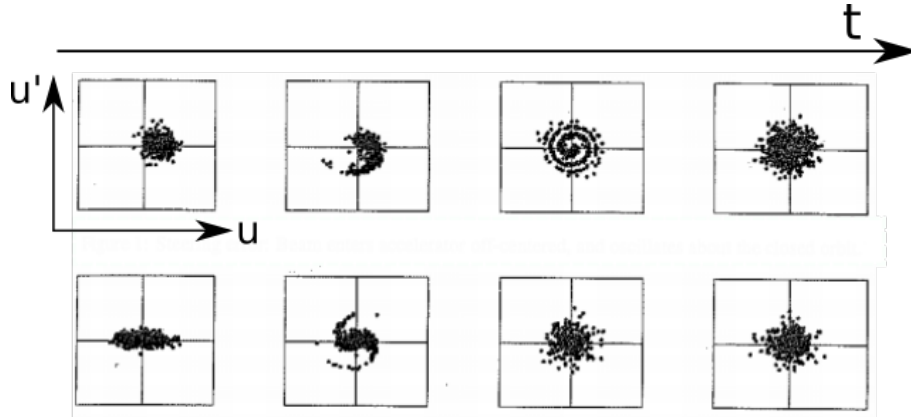


Figure 2.11: The top four images show the evolution of the phase space (from left to right) for an off-axis injected beam and the four bottom images show the evolution of a beam with mismatched twiss parameters ( $\beta$ ,  $\alpha$  and  $\gamma$ ). The coordinate  $u$  stands for  $x$  or  $y$ . The phase space area at the end is bigger than at the beginning for both cases [36].

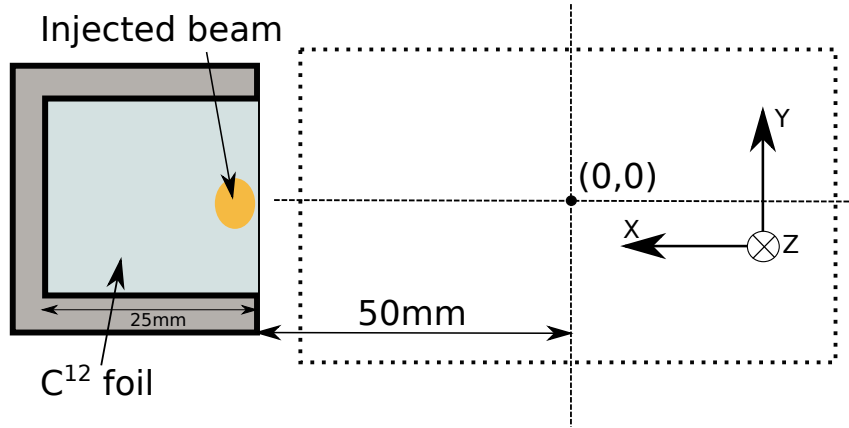


Figure 2.12: Schematic view of the stripping foil inside the vacuum chamber of COSY. The ideal orbit goes through the (0,0) point in the image. The injected beam is shown hitting the edge of the stripping foil.

The emittance of a beam which is injected off axis in an accelerator grows following the betatron motion equations (Eq. 2.13) as the particles oscillate around the orbit of the accelerator. The same occurs if the angles of both beams do not match. The evolution of a beam which has been injected off-axis is shown in Fig. 2.11, together with a beam with mismatched twiss parameters. At the same time, the number of revolutions that the orbiting beam hits the stripping foil is limited by moving it away from the foil as fast as possible. This prevents the beam emittance to grow too much, as it would happen if the beam would hit the stripping foil for an arbitrarily large number of turns  $n$  (see Eq. 2.48).

The injection process explained until now concerns the horizontal plane injection. Regarding to the vertical plane the acceptance of the machine is smaller so the phase space area is filled easier. This makes the injection simpler and it is enough to match the vertical emittance of the injected beam with the vertical acceptance of COSY. The momentum deviation of the injected beam, which is given by the cyclotron,

cannot be easily manipulated and the filling of the longitudinal acceptance of COSY ( $\frac{\Delta p}{p} = 0.5\%$ ) is then fulfilled by the energy losses in the stripping foil.



# Injection Beam Line Optimization

In this chapter the focus lies on the optimization of the Injection Beam Line (IBL). The optimization of the IBL first requires to have all the information about the beam coming out of the cyclotron. For that purpose different experiments and results are presented. Then, with the help of the computer software Bmad, the IBL is optimized for injection. Not all the measurements in this chapter were carried out in the same beam times, thus the beam could have small differences between them.

## 3.1 Beam Characterization in the IBL

As it is mentioned before, the IBL is a transport line from the cyclotron to the synchrotron. It is an open lattice. In order to analyze the properties of the beam along the IBL the initial conditions have to be known. These initial conditions are given by the source and cyclotron configurations and are dependent on many parameters such as extraction voltages and cyclotron frequency. It is important to determine the characteristics of the beam at the beginning of the IBL so that its evolution can be calculated using simulations based on the IBL settings. In order to measure the properties of the beam when it comes out of the cyclotron, several methods can be used. In this case the emittance is measured first and then, once a reasonable result is found, the twiss parameters ( $\beta$ ,  $\gamma$  and  $\alpha$ ) are calculated. Finally, the energy and momentum uncertainty are measured and the image of the beam in the IBL is then complete.

The emittance measurement is carried out using two different and independent methods and afterwards the results are compared. These methods are the **quadrupole scan method** and the **slit scan method**. An unpolarized  $H^-$  beam is used in both methods because of beam availability, but the methods are equally applicable for any type of  $D^-$  beam.

### 3.1.1 Emittance Measurement Using Quadrupole Scan Method

#### Setup

The quadrupole scan method is used to calculate the transverse emittances of the beam. It consists of varying the quadrupole strength and analyzing how this affects the beam size in the measurement point, which is located a certain drift distance  $D$  after the quadrupole. A sketch of the system is visible in Fig. 3.1.

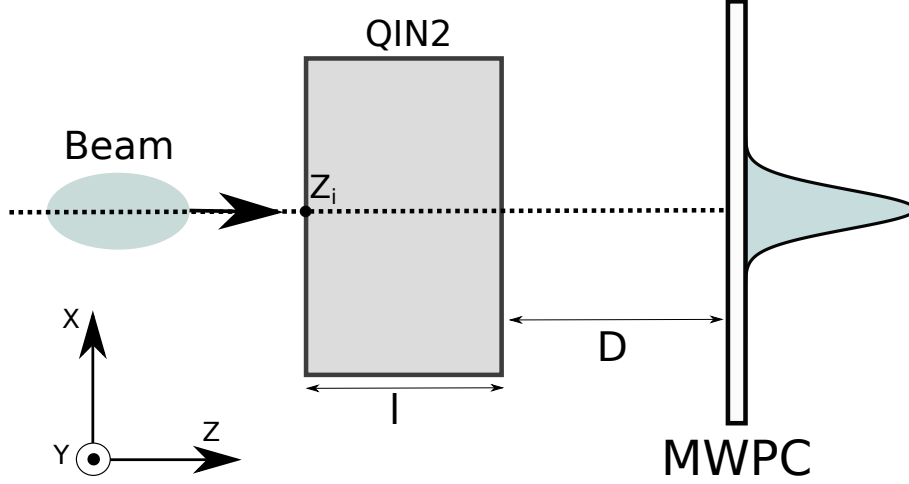


Figure 3.1: Quadrupole scan sketch. The quadrupole is represented by the gray box in the center.

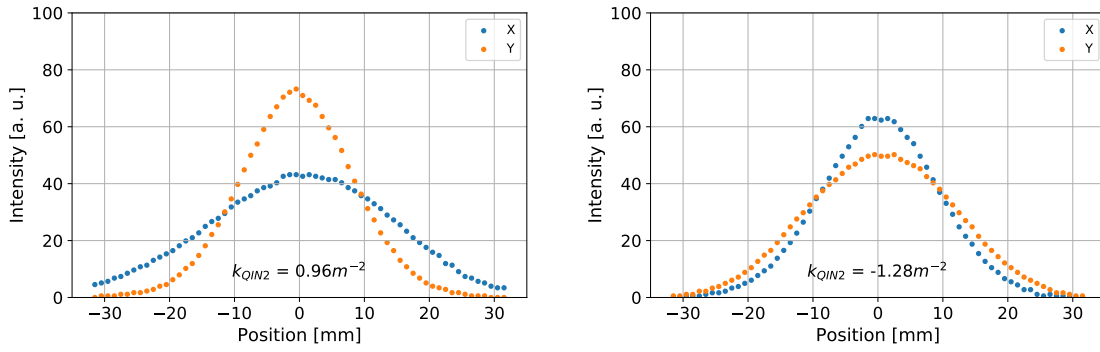


Figure 3.2: Measured beam profiles for  $x$  and  $y$  at the MWPC for  $k_{QIN2} = 0.96 \text{ m}^{-2}$  and  $k_{QIN2} = -1.28 \text{ m}^{-2}$ .

The beam profile is recorded by a Multi Wire Proportional Chamber (MWPC). In this experiment the quadrupole QIN2 is used and the drift distance is of  $D = 2.3 \text{ m}$ . The experimental setup is located in an external area connected to the IBL. The MWPC measures the beam intensity by 64 wires in  $x$  axis and another 64 wires in  $y$  axis. These wires are separated by 1 mm from each other. Fig. 3.2 shows the recorded intensity for different quadrupole strength values.

It can be seen that the beam profile matches the expected Gaussian shaped profile approximation at the location of the MWPC. The measured data is fitted with the function in Eq. 3.1 to calculate the beam width.

$$f(x) = a \cdot \exp\left(-\frac{(x-\mu)^2}{2\sigma^2}\right). \quad (3.1)$$

The standard deviation of the fitted Gaussian function is considered to be the beam size ( $\sigma_{\text{rms}} \equiv \sigma$ ). This process is repeated for different quadrupole strengths, from -20% to 16% of the maximum intensity in steps of 4%. Thus, the beam size for  $x$  and  $y$  axes is obtained from the fits for each quadrupole strength value. Fig. 3.3 shows the variation of the beam size squared as a function of the quadrupole strength  $k_{QIN2}$ .

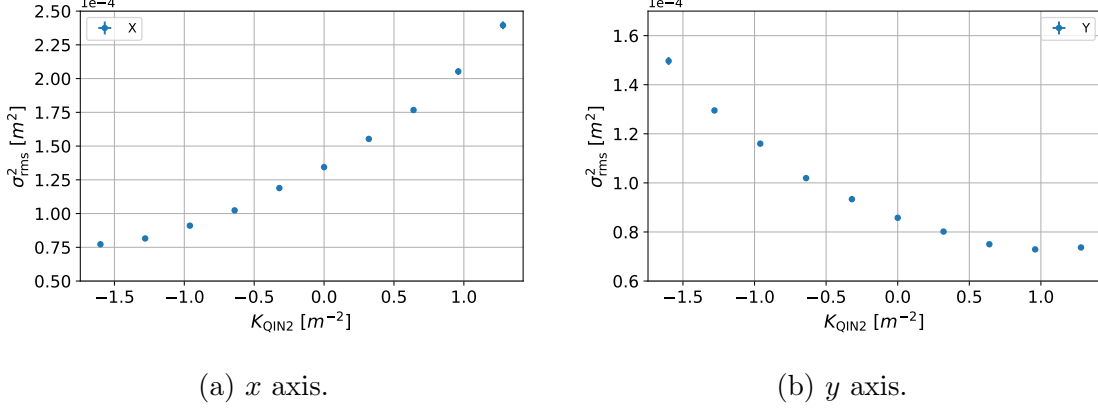


Figure 3.3: Beam size squared as a function of QIN2 strength.

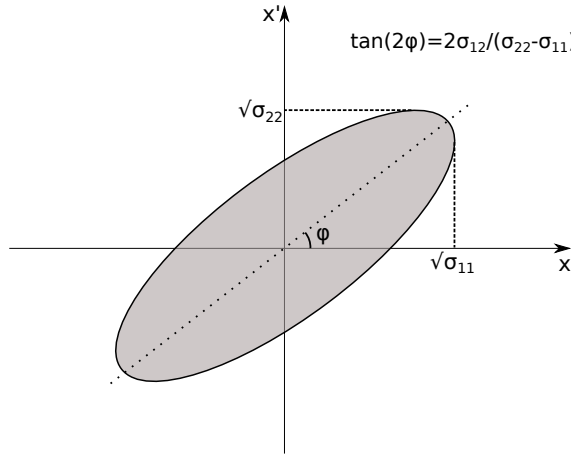


Figure 3.4: Beam matrix element representation in phase space.

### Emittance Calculation

The relation between the beam width at the MWPC and the quadrupole strength can be obtained by using the transfer matrix formalism [37].  $\sigma_{\text{beam}}$  is the matrix which describes the ellipse in the phase space for axis  $x$  or  $y$  (see Fig. 3.4):

$$\sigma_{\text{beam}} = \begin{pmatrix} \sigma_{11} & \sigma_{12} \\ \sigma_{21} & \sigma_{22} \end{pmatrix}, \quad (3.2)$$

where  $\sigma_{12} = \sigma_{21}$ .

From literature it is known that  $\langle x^2 \rangle$  is related to  $\sigma_{11}$  as shown in Eq. 3.3. The same is true for the case of  $y$  instead of  $x$ . All the emittance calculation process is explained here for  $x$  axis, but is identical for  $y$  axis.

$$\sigma_{11} = \int \int dx dx' f(x, x') x^2 = \langle x^2 \rangle \text{ if } \langle x \rangle = 0. \quad (3.3)$$

In the same way,  $\sigma_{12} = \sigma_{21} = \langle xx' \rangle$  and  $\sigma_{22} = \langle x'^2 \rangle$ . For a Gaussian distribution centered at 0 the variance  $\langle x^2 \rangle$  is equal to  $\sigma^2$ , so  $\sigma_{11}$  is directly equal to the measured  $\sigma_{\text{rms}}^2$ . Furthermore,  $\sigma_{\text{beam}}$  is related to the emittance by

$$\begin{aligned}
\epsilon &= \sqrt{|\sigma_{\text{beam}}|} = \sqrt{\sigma_{11}\sigma_{22} - \sigma_{12}^2} \\
&= \sqrt{\langle x^2 \rangle \langle x'^2 \rangle - \langle xx' \rangle^2}.
\end{aligned} \tag{3.4}$$

As explained in Sec. 2.2.2 the emittance is conserved under conservative forces where Louiville theorem applies, which is the case of the IBL, so the position  $z$  of the calculation does not affect the result. Being  $D$  the drift distance between the quadrupole and the MWPC and  $l$  the effective length of the quadrupole QIN2, an expression for the beam width squared ( $\sigma_{\text{rms}}^2 = \langle x^2 \rangle$ ) as a function of the quadrupole strength  $k$  is derived using

$$\begin{aligned}
M &= \begin{pmatrix} 1 & D \\ 0 & 1 \end{pmatrix} \cdot \begin{pmatrix} \cos(\sqrt{k}l) & \frac{1}{\sqrt{k}} \sin(\sqrt{k}l) \\ -\sqrt{k} \sin(\sqrt{k}l) & \cos(\sqrt{k}l) \end{pmatrix}, \\
\sigma_{\text{beam}} &= M \cdot \sigma_{\text{beam}}^i \cdot M^T,
\end{aligned} \tag{3.5}$$

where  $\sigma_{\text{beam}}^i$  is the beam matrix at the position  $z_i$  just before entering the quadrupole. Eq 3.6 is solved and the expression for the first matrix element is the following one:

$$\begin{aligned}
\sigma_{11} = \langle x^2 \rangle &= \sigma_{11}^i \left( \cos(\sqrt{k}l) - \sqrt{k}D \sin(\sqrt{k}l) \right)^2 \\
&+ \sigma_{12}^i \left( \cos(\sqrt{k}l) - \sqrt{k}D \sin(\sqrt{k}l) \right) \left( \frac{1}{\sqrt{k}} \sin(\sqrt{k}l) + D \cos(\sqrt{k}l) \right) \\
&+ \sigma_{22}^i \left( \frac{1}{\sqrt{k}} \sin(\sqrt{k}l) + D \cos(\sqrt{k}l) \right)^2 = \sigma_{\text{rms}}^2.
\end{aligned} \tag{3.6}$$

Eq. 3.6 gives the beam size squared as a function of quadrupole strength  $k$  and the beam parameters in front of the quadrupole. The next step is to fit Eq. 3.6 into the data from Fig. 3.3a and 3.3b so that the initial beam parameters are calculated from the fit coefficients. Then the beam emittance is calculated from them. The problem comes with the negative values of  $k$ , which lead to square root of negative values in Eq. 3.6. This is usually solved using a different matrix containing cosh and sinh functions and some minor changes. This solution arises the need to fit different functions for negative  $k$  and positive  $k$  values. In order to make the process simpler, the sinusoidal functions are expanded into polynomials using Taylor's expansion around 0.

**Second Order Approximation** The sinusoidal functions are expanded up to the second term. Using only one term can also be considered, but it makes the calculations less accurate. On the other hand, more terms can be considered in the Taylor expansion, but in that case the expressions become longer and not practical to handle.

$$\sin(\alpha) \approx \alpha - \frac{\alpha^3}{6} + \mathcal{O}(\alpha^5), \tag{3.7}$$

$$\cos(\alpha) \approx 1 - \frac{\alpha^2}{2} + \mathcal{O}(\alpha^4). \tag{3.8}$$

Now these approximations are substituted in Eq. 3.6 and the result is given in Eq. 3.9.

$$\begin{aligned}
\sigma_{11}(k) = & \left[ \sigma_{11}^i \frac{l^6 D^2}{36} \right] \cdot k^4 - \left[ \left( \frac{l^5 D}{6} + \frac{D^2 l^4}{3} \right) \sigma_{11}^i + 2 \left( \frac{D^2 l^5}{12} + \frac{D l^6}{36} \right) \sigma_{12}^i \right] \cdot k^3 \\
& + \left[ \left( \frac{l^4}{4} + l^2 D^2 + \frac{4 l^3 D}{3} \right) \sigma_{11}^i + 2 \left( 7 \frac{l^4 D}{12} + \frac{l^5}{12} + \frac{2 D^2 l^3}{3} \right) \sigma_{12}^i + \left( \frac{l^6}{36} + \frac{D^2 l^4}{4} + \frac{D l^5}{6} \right) \sigma_{22}^i \right] \cdot k^2 \\
& - \left[ (l^2 + 2 l D) \sigma_{11}^i + 2 \left( 2 D l^2 + \frac{2 l^3}{3} + D^2 l \right) \sigma_{12}^i + \left( D^2 l^2 + \frac{4 D l^3}{3} + \frac{l^4}{3} \right) \sigma_{22}^i \right] \cdot k \\
& + \left[ \sigma_{11}^i + 2 (D + l) \sigma_{12}^i + (l + D)^2 \sigma_{22}^i \right].
\end{aligned} \tag{3.9}$$

This expression describes the behavior of  $\sigma_{rms}^2 = \sigma_{11}$  as a function of the quadrupole strength  $k$ , up to the fourth order. The data in Figure 3.3 is fitted by a fourth order polynomial ( $Ak^4 + Bk^3 + Ck^2 + Ek + F$ ). Equating this fourth order polynomial to Eq. 3.9 gives the relations between the beam matrix components and the fit coefficients. Those relations are

$$\sigma_{11}^i = \frac{36A}{l^6 D^2}, \tag{3.10}$$

$$\sigma_{12}^i = - \frac{B + \left( \frac{l^5 D}{6} + \frac{D^2 l^4}{3} \right) \sigma_{11}^i}{2 \left( \frac{D^2 l^5}{12} + \frac{D l^6}{36} \right)}, \tag{3.11}$$

and then 3 equations are left from which  $\sigma_{22}^i$  can be extracted. Using one of them:

$$\sigma_{22}^i = \frac{C - \left( \frac{l^4}{4} + l^2 D^2 - \frac{4 l^3 D}{3} \right) \sigma_{11}^i - 2 \left( 7 \frac{l^4 D}{12} + \frac{l^5}{12} + \frac{2 D^2 l^3}{3} \right) \sigma_{12}^i}{\frac{l^6}{36} + \frac{D^2 l^4}{4} + \frac{D l^5}{6}}. \tag{3.12}$$

Now, the last two coefficients from the fit which are not used to determine the beam matrix elements can be related to the other 3 coefficients:

$$E = - \left[ (l^2 + 2 l D) \sigma_{11}^i + 2 \left( 2 D l^2 + \frac{2 l^3}{3} + D^2 l \right) \sigma_{12}^i + \left( D^2 l^2 + \frac{4 D l^3}{3} + \frac{l^4}{3} \right) \sigma_{22}^i \right], \tag{3.13}$$

$$F = \sigma_{11}^i + 2 (l + D) \sigma_{12}^i + (l + D)^2 \sigma_{22}^i. \tag{3.14}$$

In Eq. 3.13 and 3.14  $\sigma_{11}^i$ ,  $\sigma_{12}^i$  and  $\sigma_{22}^i$  are replaced with the expressions from Eq 3.10, 3.11 and 3.12. Then, the coefficients  $E$  and  $F$  are shown as a function of the coefficients  $A$ ,  $B$  and  $C$  plus the constants  $l$  and  $D$ . Thus, the fit does not really contain 5 independent coefficients, but only 3 instead. The results of such fits are shown in Fig. 3.5.

The uncertainties are propagated from the fit coefficients to the emittance by the relation in Eq. 3.4. The calculation is the following: first  $P_0$ ,  $P_1$ ,... are used to express the coefficients of Eq. 3.9

$$P_0 \equiv \frac{36}{D^2 l^6},$$

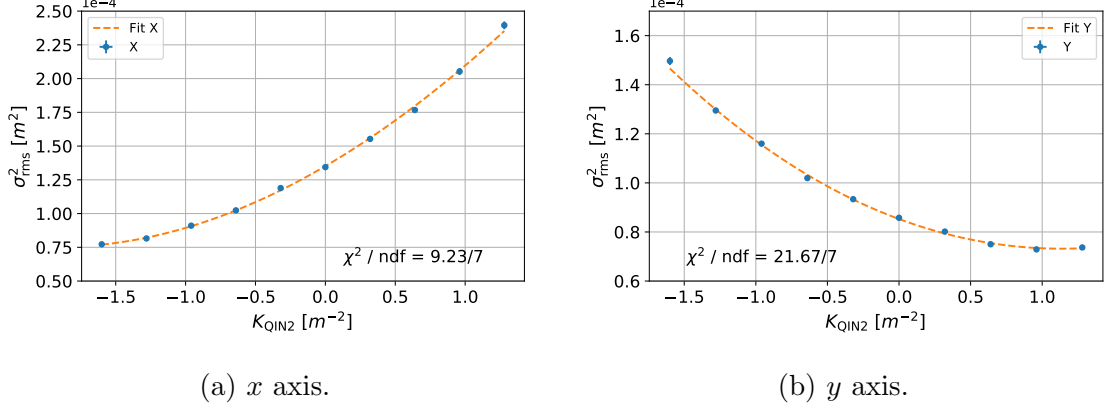


Figure 3.5: Beam size squared as a function of QIN2 strength with fourth order polynomial fit. The  $\chi^2$  test shows that the fit of the data points by the model falls inside the standard deviation for the  $x$  axis, but it lies outside for the  $y$  axis. Both fits are performed with the same assumptions in the measurement uncertainties.

$$\begin{aligned}
P_1 &\equiv \frac{l^4}{4} + l^2 D^2 + \frac{4l^3 D}{3}, \\
P_2 &\equiv 2 \left( \frac{7l^4 D}{12} + \frac{l^5}{12} + \frac{2D^2 l^3}{3} \right), \\
P_3 &\equiv \frac{l^6}{36} + \frac{D^2 l^4}{4} + \frac{Dl^5}{6}, \\
P_4 &\equiv \frac{l^5 D}{6} + \frac{D^2 l^4}{3}, \\
P_5 &\equiv 2 \left( \frac{D^2 l^5}{12} + \frac{Dl^6}{36} \right).
\end{aligned}$$

Then, the beam matrix elements are expressed as a function of the fit coefficients  $A$ ,  $B$  and  $C$  in addition to the constant coefficients  $P_0, P_1, \dots$  :

$$\sigma_{11}^i = P_0 A, \quad (3.15)$$

$$\sigma_{12}^i = -\frac{B + P_4 \sigma_{11}^i}{P_5} = -\frac{B + P_4 P_0 A}{P_5}, \quad (3.16)$$

$$\sigma_{22}^i = \frac{C - P_1 \sigma_{11}^i - P_2 \sigma_{12}^i}{P_3} = \frac{C - P_1 P_0 A + P_2 \frac{B + P_4 P_0 A}{P_5}}{P_3}. \quad (3.17)$$

So  $|\sigma_{\text{beam}}|$  is expressed as:

$$|\sigma_{\text{beam}}^i| = \sigma_{11}^i \sigma_{22}^i - (\sigma_{12}^i)^2 = \frac{P_0 A}{P_3} \left[ C - P_1 P_0 A + \frac{P_2}{P_5} (B + P_4 P_0 A) \right] - \frac{(B + P_4 P_0 A)^2}{P_5^2}. \quad (3.18)$$

Here the derivatives  $\frac{\partial |\sigma_{\text{beam}}|}{\partial A}$ ,  $\frac{\partial |\sigma_{\text{beam}}|}{\partial B}$ ,  $\frac{\partial |\sigma_{\text{beam}}|}{\partial C}$  are taken considering that all the coefficients  $P_0, P_1, \dots$  are constant. The uncertainty is given by

$$\delta_{|\sigma_{\text{beam}}|} = \left[ \left( \frac{\partial |\sigma_{\text{beam}}|}{\partial A} \delta_A \right)^2 + \left( \frac{\partial |\sigma_{\text{beam}}|}{\partial B} \delta_B \right)^2 + \left( \frac{\partial |\sigma_{\text{beam}}|}{\partial C} \delta_C \right)^2 + 2 \frac{\partial |\sigma_{\text{beam}}|}{\partial A} \frac{\partial |\sigma_{\text{beam}}|}{\partial B} \sigma_{AB} + 2 \frac{\partial |\sigma_{\text{beam}}|}{\partial A} \frac{\partial |\sigma_{\text{beam}}|}{\partial C} \sigma_{AC} + 2 \frac{\partial |\sigma_{\text{beam}}|}{\partial B} \frac{\partial |\sigma_{\text{beam}}|}{\partial C} \sigma_{BC} \right]^{\frac{1}{2}}, \quad (3.19)$$

where  $\sigma_{ij}$  represents the covariance between the parameters  $i$  and  $j$ . Finally,

$$\delta_\epsilon = \frac{\delta_{|\sigma_{\text{beam}}|}}{2\sqrt{|\sigma_{\text{beam}}|}}. \quad (3.20)$$

The measured emittances and the corresponding uncertainties are shown in Table 3.1.

Table 3.1: Emittance results for **quadrupole scan method**.

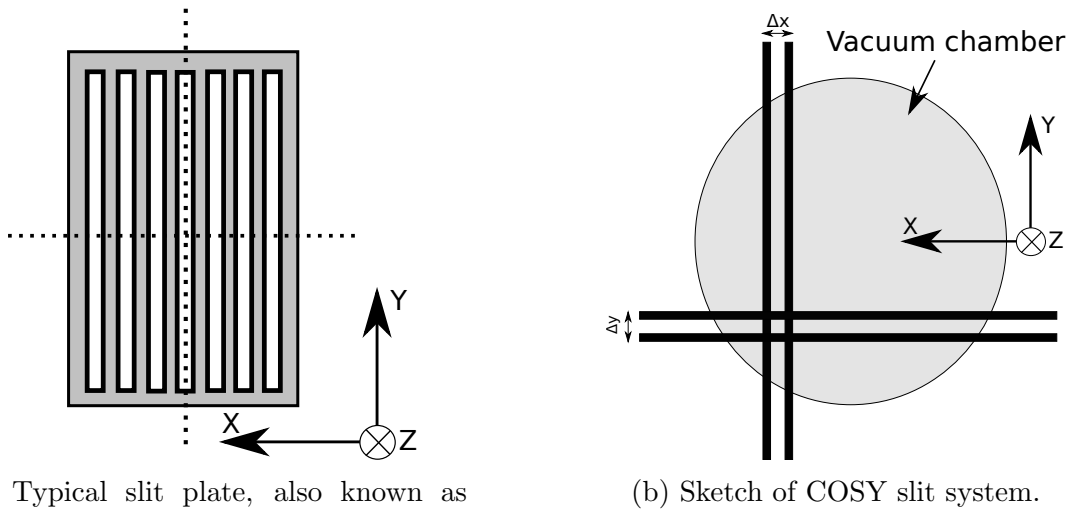
Axis	A [ $m^{10}$ ]	B [ $m^8$ ]	C [ $m^6$ ]	$\epsilon$ [mm · mrad]
X	$(4.1 \pm 0.1) \times 10^{-9}$	$(-5.0 \pm 0.2) \times 10^{-7}$	$(1.44 \pm 0.06) \times 10^{-5}$	$18.9 \pm 0.4$
Y	$(2.0 \pm 0.1) \times 10^{-9}$	$(-2.8 \pm 0.1) \times 10^{-7}$	$(1.00 \pm 0.05) \times 10^{-5}$	$14.8 \pm 0.4$

### 3.1.2 Emittance Measurement Using the Slit Scan Method

#### Setup

The slits method is a commonly used method for emittance measurement. It consists on cutting the incident beam through slits and then measuring the partial beams (beamlets) which go through in a screen located at a certain distance  $L$ . It is important to note that this measurement technique does not rely on any interference between the beamlets that go trough different slits. Then, instead of using many slits at the same time, only one can be used at a time. The principle can be seen in Fig. 3.7. The smaller the width of the slit is the better for the measurement, a point source beam would be the optimal case.

In the case of COSY there is not any slit plate as the one shown in Fig. 3.6a along the IBL. However, there is a configurable slit system after the cyclotron which allows to construct a 1 mm wide slit (1 mm is the minimum, it can also be wider) in both  $x$  and  $y$  directions (see Fig. 3.6b). This slits can then be moved to scan the beam. This way the measurement can be done for different slit positions and the results are equivalent to the ones obtained with a multiple slit plate. A sketch of the measurement principle in COSY can be seen in Fig. 3.7. Furthermore, this configuration allows for a more precise measurement than the multiple slit plate system, because all the beam can be scanned without leaving gaps between slit positions. For the experiment the  $x$  direction slit is moved along the axis while the slit in  $y$  is left totally open, so that it does not disturb the beam. Once all the beam is scanned in  $x$  direction the process is repeated for the slit in  $y$ , this time being the slit in  $x$  the one which is left completely open.



(a) Typical slit plate, also known as beam mask. In this case, the slits are distributed uniformly along the  $x$  axis.

(b) Sketch of COSY slit system.

Figure 3.6: Comparison of two slit systems, the one from [39] on the left and the one in COSY on the right.

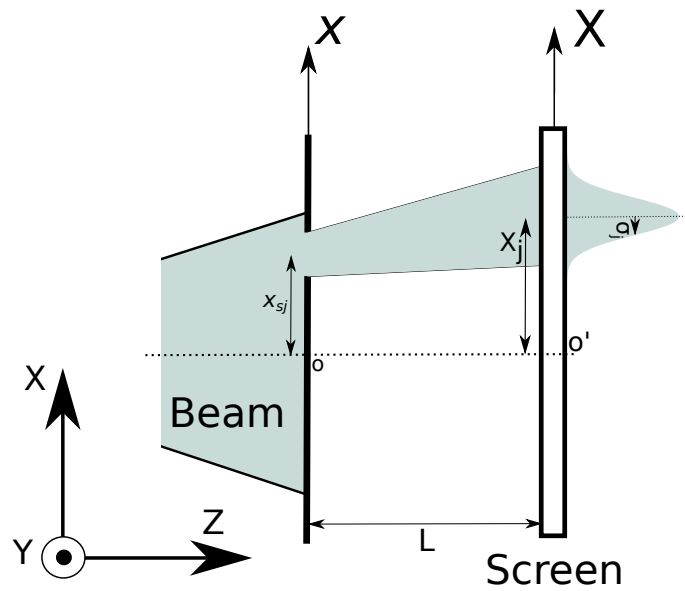


Figure 3.7: Sketch of a slit measurement. The incident beam comes from the left and impacts with the slit plate. The beamlets that go through the slits are then measured in a screen after traveling the distance  $L$ . Measured quantities  $X_i$  and  $x_i$  are shown,  $x'_i$  is derived from them.

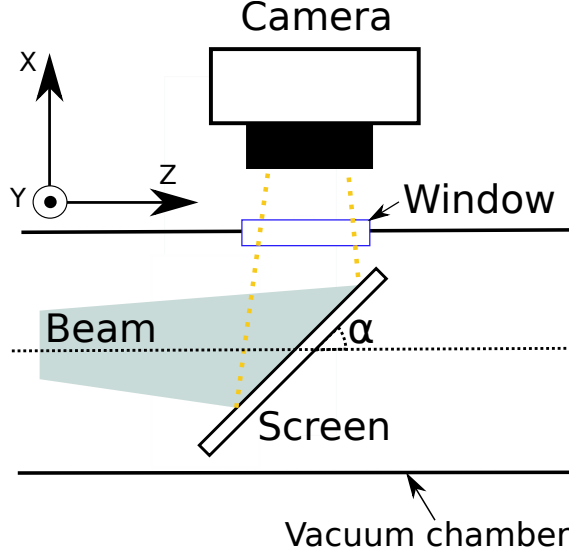


Figure 3.8: The scintillation foil, called screen, and camera sketch.

The beam going through the slit is recorded using a scintillation foil, called 'screen', which is rotated  $\alpha \approx \frac{\pi}{4} \text{rad}$  respect to the  $z$  axis (see Fig. 3.8). When the beam hits the foil light is emitted by scintillation. This light is captured by a camera and saved as an image. The images taken for different slit positions are analyzed with a specially in-house designed software and the beam distribution in the screen is extracted.

### Emittance Calculation

The objective is to calculate the emittance of the beam using the information from the screen and slit positions. Fig. 3.10 only shows the  $y$  axis scan case, but the same process is also repeated for the  $x$  direction.

All the calculations shown here are done for the  $x$  axis, but the procedure for  $y$  is identical. As it can be seen in Fig. 3.7,  $x$  is the coordinate of the slit plate and the position of the slit is denoted  $x_{sj}$ . For the screen the coordinate  $X$  is used. Then, being  $M$  the total number of particles before the slit,  $(x_i, y_i)$  and  $(x'_i, y'_i)$  describe the transverse position and momenta for the particle number  $i = 1, 2, \dots, M$ .  $x'_i$  is defined as

$$x'_i \equiv \frac{X_i - x_i}{L}. \quad (3.21)$$

As it is shown in Sec. 3.1.1, the emittance is defined by Eq. 3.22:

$$\epsilon_x = \sqrt{\langle x^2 \rangle \langle x'^2 \rangle - \langle xx' \rangle^2}, \quad (3.22)$$

where

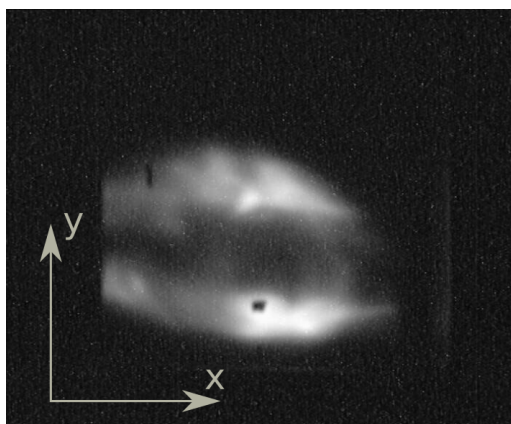


Figure 3.9: Full beam image without any filtering with slits. There are markers in the foil at 1 cm distance from the center in the horizontal and vertical directions. The apparent distance difference from the center to the markers shown here is due to the tilting of the foil in  $z$  direction. The markers are used for calibration. It can be seen that the beam center is shifted away from the scintillation foil center. A double structure can also be appreciated in the vertical direction. This effect is caused by the cyclotron and cannot be completely avoided.

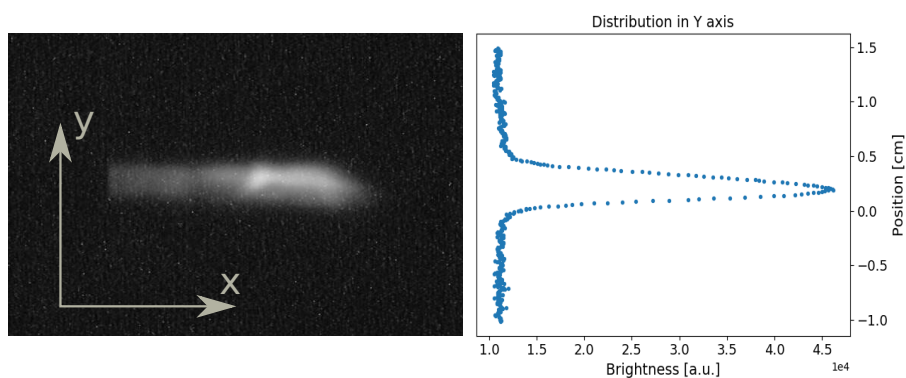


Figure 3.10: On the left side the image of the beam after going through the horizontal slits is shown. The distribution in the right side corresponds to the projection of the brightness into the  $y$  axis.

$$\begin{aligned}
\langle x^2 \rangle &\equiv \frac{1}{M} \sum_{i=1}^M (x_i - \bar{x})^2, \\
\bar{x} &\equiv \frac{1}{M} \sum_{i=1}^M x_i, \\
\langle xx' \rangle &\equiv \frac{1}{M} \sum_{i=1}^M (x_i - \bar{x})(x'_i - \bar{x}').
\end{aligned} \tag{3.23}$$

If a mask (slit plate) is placed in front of the incident beam, it is clear that the number of particles behind this mask is  $N \leq M$ . Then,  $N$  forms a subset of the beam. The emittance is calculated for this subset and how accurate the calculation is depends on how close is  $N$  from  $M$ . In this case, as there is a movable slit instead of a slit plate, most of the beam is scanned, so it can be said that  $N \approx M$ . From now on, only the subset emittance is discussed, but keeping in mind that if  $N = M$  the subset emittance and the total emittance of the beam are equal.

The first task is to express the variables shown in Eq. 3.23 as a function of the measurable quantities in the experiment. Being  $j$  the subscript representing each of the slit positions, those quantities are:

- $x_{sj} = j^{\text{th}}$  slit position.
- $n_j =$  Number of particles going through the  $j^{\text{th}}$  slit and reaching the screen.
- $\bar{X}_j =$  Mean position of the beamlet going through the  $j^{\text{th}}$  slit in the screen.
- $\sigma_j =$  Rms width of the beamlet going through the  $j^{\text{th}}$  slit in the screen.
- $N =$  The total number of particles going through all slit positions.

Being  $p$  the total number of slit positions used to scan the beam, clearly:

$$n_1 + n_2 + \dots + n_p = N. \tag{3.24}$$

The detailed mathematical derivation of the following formulas from the expressions in Eq. 3.23 is found in [39], here only the result is shown. In order to obtain the measurable quantities  $\bar{X}_j$ ,  $\sigma_j$  and  $n_j$  from the data, a Gaussian type function is fitted and the background subtracted to each of the obtained distributions (one for each slit position). The mean position and rms width of the fit, together with the corresponding uncertainties, are directly related to  $\bar{X}_j$  and  $\sigma_j$  of the beamlet. The number of particles  $n_j$  that go through the  $j^{\text{th}}$  slit is proportional to the measured brightness (integral of the fitted Gaussian function). The uncertainties in the fit parameters ( $\delta_\mu$ ,  $\delta_\sigma$  and  $\delta_{n_j}$ ) are propagated to the calculated values  $\langle x^2 \rangle$ ,  $\langle xx' \rangle$  and  $\langle x'^2 \rangle$  using the standard Gaussian error propagation. It is also proven in [39] that the emittance results obtained with this method are independent of the origin of the coordinates in  $x$  and  $X$ . Thus, the only requisite is that  $x$  and  $X$  have the same units. Then, the emittance reads:

$$\begin{aligned}
\epsilon_x^2 &= \langle x^2 \rangle \langle x'^2 \rangle - \langle xx' \rangle^2 \\
&\approx \frac{1}{N^2} \left\{ \left[ \sum_{j=1}^p n_j (x_{sj} - \bar{x})^2 \right] \left[ \sum_{j=1}^p \left[ n_j \sigma_{x'_j}^2 + n_j (\bar{x}'_j - \bar{x}')^2 \right] \right] - \left[ \sum_{j=1}^p n_j x_{sj} \bar{x}'_j - N \bar{x} \bar{x}' \right]^2 \right\},
\end{aligned} \tag{3.25}$$

and the corresponding uncertainty is given by

$$\begin{aligned}
\delta_\epsilon &= \frac{1}{2\epsilon} \delta_{\epsilon^2} \\
&= \frac{1}{2\epsilon} \sqrt{(\langle x^2 \rangle \delta_{\langle x'^2 \rangle})^2 + (\langle x'^2 \rangle \delta_{\langle x^2 \rangle})^2 + (2 \langle xx' \rangle \delta_{\langle xx' \rangle})^2}.
\end{aligned} \tag{3.26}$$

The results obtained by the slit scan method are shown in Table 3.2.

Table 3.2: Emittance results for **slit scan method**, where  $u$  represents any of the coordinates  $x$  or  $y$ .

Axis	$\langle u^2 \rangle$ [mm <sup>2</sup> ]	$\langle u'^2 \rangle$ [mrad <sup>2</sup> ]	$\langle uu' \rangle$ [mm · mrad]	$\epsilon$ [mm · mrad]
X	11.2 ± 0.4	40 ± 10	11 ± 1	18.8 ± 0.2
Y	25.5 ± 0.4	8 ± 5	-5.0 ± 0.4	13.2 ± 0.2

It can be seen that the results from Table 3.1 and 3.2 are compatible within the errors for the  $x$  axis, even if the measurement methods are independent from each other and they are carried out in different beam times. On the other hand, the results in  $y$  are within  $4\sigma$  from each other, this could be an indicator that there is some process which affects the emittance measurement in  $y$  axis in any of the two methods. The results are summarized in Fig. 3.11.

## 3.2 Twiss Parameters and Momentum

In order to have all the information about the beam when it goes through the IBL, the twiss parameters are needed. As it is mentioned in Sec. 2.2.2, the evolution of the  $\beta(z)$  functions along an open lattice depends on the initial parameters  $\beta_0$  and  $\alpha_0$  for any of the transverse directions. Thus, taking into account that the emittance measurements using the slits are done some drift distance before the beginning of the IBL, the twiss parameters at that position can be calculated. The twiss parameters will be denoted  $\beta_{\text{IBL}}$ ,  $\alpha_{\text{IBL}}$  and  $\gamma_{\text{IBL}}$  when the values correspond to the initial position of the IBL and  $\beta_0$ ,  $\alpha_0$  and  $\gamma_0$  when they belong to the slit positions. Eq. 2.27 gives the relation between the beam size squared, the  $\beta(z)$  function at the same point and the emittance.  $\langle u^2 \rangle$  is calculated in Table 3.2 for  $x$  and  $y$ . In addition, it is mentioned before that for Gaussian distribution centered at 0  $\langle u^2 \rangle = \sigma_u^2$ . Thus, from Eq. 2.27 the twiss parameters at the slit positions are derived:

$$\langle u^2 \rangle_0 = \beta_0 \epsilon \Rightarrow \beta_0 = \frac{\langle u^2 \rangle_0}{\epsilon}, \tag{3.27}$$

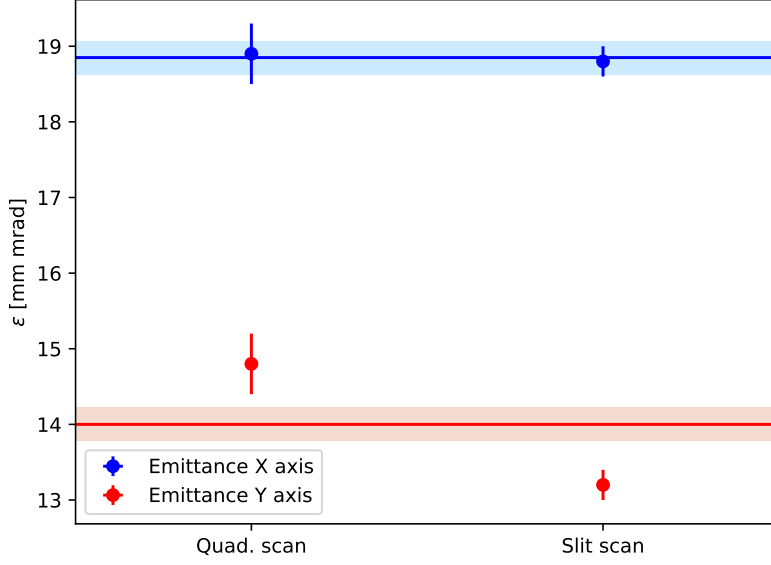


Figure 3.11: The results from the two emittance measurement methods are shown here. The horizontal lines represent the average values for the emittances in  $x$  (blue) and  $y$  (red), with the corresponding uncertainty shown by the shadowed region.

$$\langle uu' \rangle_0 = -\alpha_0 \epsilon \Rightarrow \alpha_0 = -\frac{\langle uu' \rangle_0}{\epsilon}, \quad (3.28)$$

$$\langle u'^2 \rangle_0 = \gamma_0 \epsilon \Rightarrow \gamma_0 = \frac{\langle u'^2 \rangle_0}{\epsilon}. \quad (3.29)$$

If the transfer matrix and initial conditions are known, using the evolution matrix given in [26, p.87] the twiss parameters of any other point in the lattice can be calculated. There is only drift space between the slits and the beginning of the IBL. For a drift space of length  $D$  the transfer matrix is

$$M = \begin{pmatrix} m_{11} & m_{12} \\ m_{21} & m_{22} \end{pmatrix} = \begin{pmatrix} 1 & D \\ 0 & 1 \end{pmatrix}. \quad (3.30)$$

The relation between the twiss parameters at the slit positions and the twiss parameters at the beginning of the IBL is given by:

$$\begin{pmatrix} \beta_{\text{IBL}} \\ \alpha_{\text{IBL}} \\ \gamma_{\text{IBL}} \end{pmatrix} = \begin{pmatrix} m_{11}^2 & 2m_{11}m_{12} & m_{12}^2 \\ -m_{11}m_{21} & m_{11}m_{22} + m_{12}m_{21} & -m_{22}m_{12} \\ m_{21}^2 & -m_{22}m_{21} & m_{22}^2 \end{pmatrix} \begin{pmatrix} \beta_0 \\ \alpha_0 \\ \gamma_0 \end{pmatrix} = \begin{pmatrix} 1 & -2D & D^2 \\ 0 & 1 & -D \\ 0 & 0 & 1 \end{pmatrix} \begin{pmatrix} \beta_0 \\ \alpha_0 \\ \gamma_0 \end{pmatrix}. \quad (3.31)$$

Hence, the  $\beta$ ,  $\alpha$  and  $\gamma$  values at the beginning of the IBL can be calculated for both  $x$  and  $y$  directions.

$$\beta_{\text{IBL}} = \beta_0 - 2D\alpha_0 + D^2\gamma_0, \quad (3.32)$$

$$\alpha_{\text{IBL}} = \alpha_0 - D\gamma_0, \quad (3.33)$$

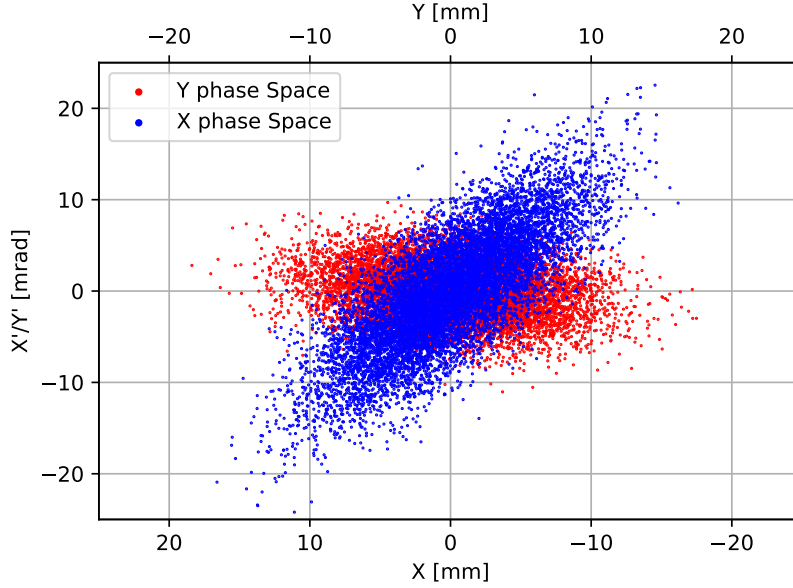


Figure 3.12:  $x$  and  $y$  phase spaces at the beginning of the IBL.  $10^4$  particles are randomly placed inside Gaussian distribution functions determined by the twiss parameters shown in Table 3.3.

$$\gamma_{\text{IBL}} = \gamma_0. \quad (3.34)$$

The drift distances are  $D_x = 312$  mm and  $D_y = 242$  mm. The results are given in Table 3.3.

Table 3.3: Twiss parameters at the beginning of the IBL.

	$\beta_{\text{IBL}}[\text{m}]$	$\alpha_{\text{IBL}}$	$\gamma_{\text{IBL}}[\text{m}^{-1}]$
X	$1.17 \pm 0.06$	$-1.2 \pm 0.1$	$2.1 \pm 0.5$
Y	$1.78 \pm 0.04$	$0.23 \pm 0.01$	$0.6 \pm 0.4$

The values of  $\beta_0$ ,  $\alpha_0$  and  $\gamma_0$  in Table 3.3 are calculated independently. However, there is a relation between them given by Eq. 2.30, which can be used as a quick check that the results are sensible.

$$\beta_0\gamma_0 - \alpha_0^2 - 1 = \begin{cases} 0.0 \pm 0.8 \text{ in } x, \\ 0.0 \pm 0.7 \text{ in } y. \end{cases} \quad (3.35)$$

As it is seen in Eq. 3.35 both results are compatible with 0, which is the expected value given by Eq. 2.30. Finally, the initial  $x$  and  $y$  phase spaces of the beam at the beginning of the IBL are shown in Fig. 3.12.

### Kinetic Energy and Momentum Deviation

The kinetic energy of the  $\text{H}^-$  beam is also measured. This is done by measuring the time of flight between two phase probes that are found along the IBL. Once the distance between both phase probes is known the kinetic energy is calculated using

$$E_k = m(\gamma - 1)c^2 = m \left( \frac{1}{\sqrt{1 - \left(\frac{v}{c}\right)^2}} - 1 \right) c^2 = m \left( \frac{1}{\sqrt{1 - \left(\frac{d}{tc}\right)^2}} - 1 \right) c^2, \quad (3.36)$$

where  $d$  is the distance between the phase probes,  $t$  is the measured time of flight and  $m$  is the mass of the particles. The momentum deviation is also calculated from the energy uncertainty. The measured kinetic energy for  $H^-$  particles is

$$E_k = (45.125 \pm 0.007) \text{ MeV}. \quad (3.37)$$

Therefore, using the relation  $(E_k + E_0)^2 = p^2 c^2 + E_0^2$  and Eq. 2.47 the momentum deviation in the IBL is given by

$$\frac{\Delta p}{p} = 0.08\%. \quad (3.38)$$

### 3.3 Quadrupole Optimization

The next step is the optimization of the lattice in the IBL. As it is mentioned in Sec. 1.4.2, the IBL is composed by 8 sections, each of them with its own purpose. It starts at the exit of the cyclotron, in the position of the first profile grid, and it finishes in the stripping foil. The main magnets in the IBL are dipole magnets for beam bending and quadrupole magnets for beam focusing. There are also several steering magnets to steerer the beam if necessary, but they are not taken into account in this optimization. The optimization process consists on tuning the magnetic field values so that the transfer beam line fulfills some characteristic behavior. Not all the magnets can be freely tuned. The field strength of the dipole magnets can not be changed for example, as doing so would change the path of the beam, which is enclosed by a rigid vacuum pipe. Then, the free parameters are the quadrupole strengths, noted as  $k$ . This magnitude is used to indicate the amount of focusing that a quadrupole applies to a beam, independently of the beam composition and energy. When a specific particle and fixed energy beam goes through the quadrupoles, the magnetic field gradient required to focus the beam as specified by the value  $k$  is given by the product of  $k$  with the magnetic rigidity  $B\rho$ :

$$g \left[ \frac{T}{m} \right] = k \left[ \frac{1}{m^2} \right] B\rho [Tm]. \quad (3.39)$$

For 45 MeV protons  $B\rho = 0.98 \text{ Tm}$  and for 76 MeV deuterons  $B\rho = 1.80 \text{ Tm}$ . Then, the optimization of the quadrupole strength can be done without taking into account the type of beam traveling through the IBL. The sign of  $k$  indicates if the quadrupole is focusing (+) or defocusing (-) in the  $x$  plane for a positive charge particle. The ions traveling through the IBL are always negative charge particles, because the charge-exchange injection method requires so, hence a positive  $k$  value indicates a defocusing quadrupole in the horizontal plane and vice versa.

However, even if all the quadrupole strengths can be tuned, it is not possible to do it individually. Quadrupoles are not powered with an individual power supply

each, but instead they are powered in groups to make things easier. For most of the sections in the IBL (sections 2 to 7) all quadrupoles in the same section share the same power supply, but the polarity is alternated. This means that for example in the case of the second section all 4 quadrupoles (named  $QI2X$ , where  $X$  is the quadrupole number) have the same absolute current but alternated sign:

$$I_{QI21} = -I_{QI22} = I_{QI23} = -I_{QI24}. \quad (3.40)$$

This implies that the  $k$  values of these quadrupoles in the optimization have to be kept equal in absolute value. The  $k$  value for all the section is denoted  $k_{2x}$  and its sign represents the sign of the first quadrupole in the section. Furthermore, the quadrupole strength values can not take arbitrarily large absolute values, as the power supplies have certain limits. Those limits for 100% and -100% capacities of the power supplies are calculated and included in the optimization code.

### 3.3.1 Optimization

For the optimization an ideal Bmad model of the IBL is used. The parameters in this model are the original design parameters from SIEMENS. The last part of the transfer line includes the injection dipole. Given the difficulty to define this dipole as a usual dipole magnet in Bmad, its 6x6 transfer matrix is experimentally determined in [35] and shown in Eq. 3.41. Then, the matrix is implemented in the code.

$$M_{\text{dipole}} = \begin{pmatrix} 0.309 & 1.695 & 0 & 0 & 0 & 0.130 \\ -0.509 & 0.433 & 0 & 0 & 0 & 0.153 \\ 0 & 0 & 1.758 & 3.231 & 0.0 & \\ 0 & 0 & 0.571 & 1.618 & 0 & 0 \\ -0.114 & -0.203 & 0 & 0 & 1 & -0.004 \\ 0 & 0 & 0 & 0 & 0 & 1 \end{pmatrix}. \quad (3.41)$$

This transfer matrix is applicable from the position of the last viewer in the last section of the IBL ( $z = 91.04$  m) to the stripping foil. The sectioning of the IBL can be seen in Fig. 3.13. The optimization process is dissected for the first two sections, the rest of them follow the same logic as one of the first two sections. Therefore, only the purpose of each section is explained.

#### Section 1

The first section of the IBL is designed as an achromat. An achromat is a lattice that does not add dispersion to the beam. The bending magnets introduce a dispersion in the beam because different momentum particles are not bent by the same angle (see Sec. 2.2). This dispersion introduced in the bending magnets has to be countered by the quadrupole magnets and the face angles of the dipoles. In transfer matrix formalism, the dispersion vector (the dispersion and its derivative form the dispersion vector:  $\mathbf{d} = (D, D')$ ) is composed by the elements  $M_{16}$  and  $M_{26}$  of the 6x6 matrix. In addition, it is highly preferable to achieve a diagonal transfer matrix for the whole section, with the diagonal elements as close to 1 or -1 as possible. This last condition ensures that the 6 dimensional phase space will be the same (diagonal elements equal to 1) or a mirror image (diagonal elements equal

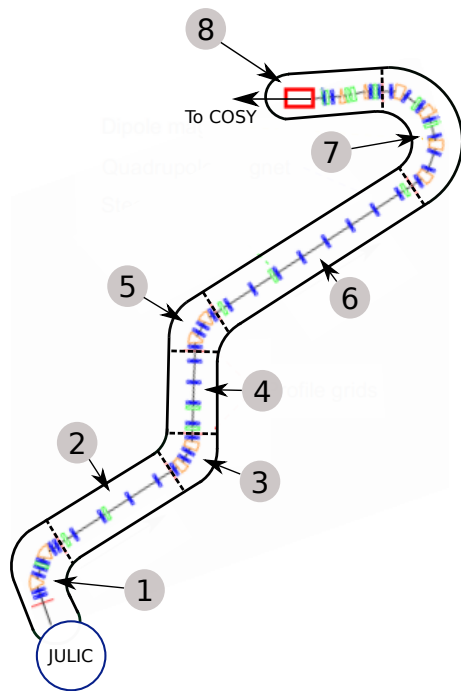


Figure 3.13: Sketch of the IBL divided in 8 sections.

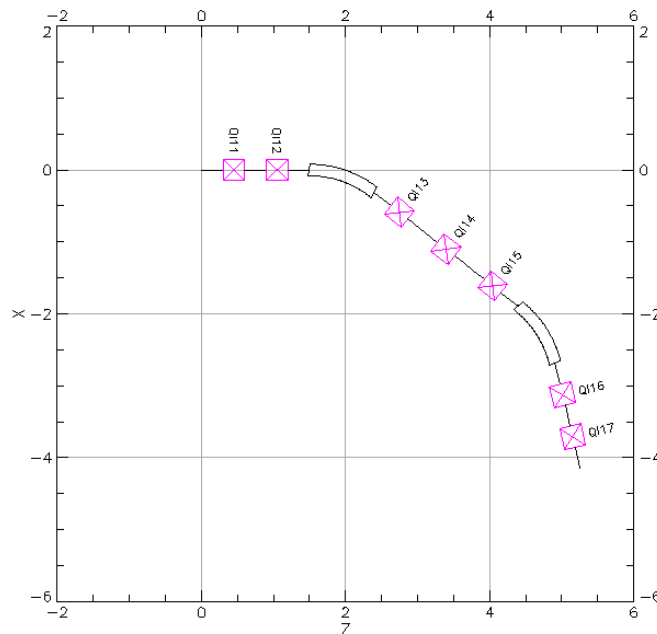


Figure 3.14: Section 1 from the IBL in the  $x - z$ -plane. Pink boxes represent quadrupole magnets and black rectangles represent dipole magnets. The beam origin is at  $(x, z) = (0, 0)$  and the initial velocity is  $\mathbf{v} = v(0, 1)$ .

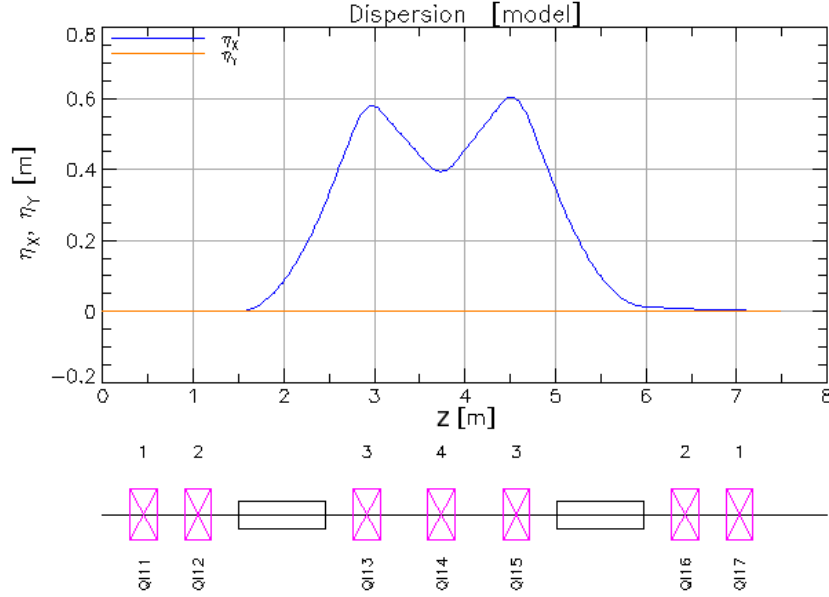


Figure 3.15: Dispersion in  $x$  and  $y$  along  $z$  for section 1 of the IBL.

to -1) at the end of the section as the one at the beginning.

Section 1 is different to the rest (except to section 8, which is used to match the beam properties to COSY) because not all the quadrupoles are powered by the same power supply. They are powered symmetrically with

$$I_{Q111} = I_{Q117}, \quad I_{Q112} = I_{Q116}, \quad I_{Q113} = I_{Q115} \quad (3.42)$$

and  $I_{Q114}$  is powered individually. See Fig. 3.14 to identify the quadrupoles. The reason to do it this way is that this gives more room to fit the parameters of the beam coming from the cyclotron to the transfer line. The dispersion along the trajectory for the quadrupole strength values obtained in the optimization is shown in Fig. 3.15.

The obtained  $k$  values are shown in Table 3.4. Then, the 6x6 transfer matrix for section 1 is:

$$M_{\text{section1}} = \begin{pmatrix} 0.99 & 0.18 & 0 & 0 & 0 & -8 \cdot 10^{-4} \\ -0.04 & 0.99 & 0 & 0 & 0 & -9 \cdot 10^{-3} \\ 0 & 0 & -0.99 & 0.05 & 0 & 0 \\ 0 & 0 & 0.11 & -0.99 & 0 & 0 \\ 9 \cdot 10^{-3} & 8 \cdot 10^{-4} & 0 & 0 & 1 & 0 \\ 0 & 0 & 0 & 0 & 0 & 1 \end{pmatrix}. \quad (3.43)$$

## Section 2

Section 2 is designed as a FODO structure. A FODO structure is an alternating focusing and defocusing quadrupole magnet structure. It is a straight section of 17m and is constructed with 4 magnets. Section 2 is designed to obtain a diagonal transfer matrix with  $\pi$  phase advance, which is the equivalent to stating that the diagonal elements have to be equal to  $-1$  (in the blocks corresponding to  $x$  and  $y$

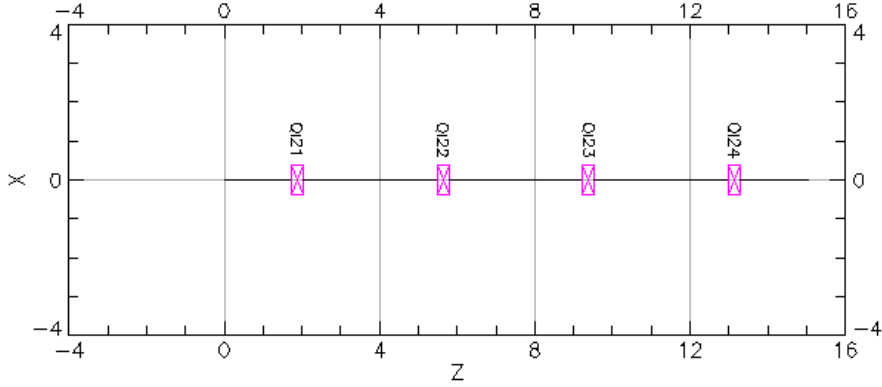


Figure 3.16: Section 2 in the IBL in the  $x - z$ -plane. the beam origin and velocity are the same as in Fig. 3.14.

phase spaces). Section 2 is shown in Fig. 3.16. There is no bending in this section so dispersion does not have to be considered. All the quadrupoles here are powered by the same power supply. The optimization results are in Table 3.4 and after the optimization the transfer matrix looks like

$$M_{\text{section2}} = \begin{pmatrix} -1.00 & 0.00 & 0 & 0 & 0 & 0 \\ 0.00 & -1.00 & 0 & 0 & 0 & 0 \\ 0 & 0 & -1.00 & 0.00 & 0 & 0 \\ 0 & 0 & 0.00 & -1.00 & 0 & 0 \\ 0 & 0 & 0 & 0 & 1 & 0 \\ 0 & 0 & 0 & 0 & 0 & 1 \end{pmatrix}. \quad (3.44)$$

The FODO sections have the characteristic that the optimization gives two results of the same absolute value but opposite sign. With both  $k$  values the same transfer matrix is obtained. This gives the possibility to choose any of them, and the criteria is that when all sections are put together the solution which makes the  $\beta$  functions smaller is chosen. This solution is related to the last quadrupole of the previous section, because if QI17 is a defocusing quadrupole in the horizontal direction then it is logical that QI21 is chosen as a focusing one, or vice versa.

### Sections 3 to 7

The rest of the sections in the IBL up to section 7 are categorized in one of the two first section categories, either achromats or FODO structures with  $\pi$  or  $2\pi$  phase advances. A short summary is given here:

- Sections 3, 4 and 5 form an achromat section all together. To proceed with the optimization first the middle section, section 4, is optimized as a FODO structure of  $\pi$  phase advance. In this part all 4 quadrupoles are powered by the same power supply, it is very similar to section 2. Once the quadrupole strengths for section 4 are fixed, sections 3 and 5 are added to the simulation and all the system composed of sections 3, 4 and 5 is optimized together as an achromat. Sections 3 and 5 are bending sections, but they bend the beam in opposite directions. Thus, a chicane is formed when merging them together. All quadrupoles in sections 3 and 5 are powered with the same power

supply, so there are only two free parameters to optimize in the whole 3,4 and 5 combination:  $k_{4x}$  and  $k_{3x5x}$ . A unitary diagonal matrix is also possible to achieve here.

- Section 6 is another FODO structure, but this time is composed of 8 quadrupole magnets which are powered by the same power supply. Section 6 is optimized to get a  $2\pi$  phase advance, with a diagonal and unitary transfer matrix.
- Finally, section 7 is another bending section. It is made up of 4 identical quadrupole-dipole-quadrupole structures, where all quadrupoles are again powered together. It is optimized as an achromat, but it is not possible to achieve a diagonal unitary matrix in  $y$  phase space.

Section 8 is responsible to match the  $\beta$  function and the dispersion in  $x$  and  $y$  planes to the values at injection point in COSY. However, the COSY model is analyzed in the next chapter, so the optimization of section 8 is done once the necessary information is given. The quadrupole strengths obtained in the optimization of sections 1 to 7 are shown in Table 3.4 under the column ‘Optics 1’.

Table 3.4: Results for IBL optimization.

Section #	Variable name	Optics 1 [ $\frac{1}{\text{m}^2}$ ]
1	$k_{11-17}$	3.44
1	$k_{12-16}$	-3.66
1	$k_{13-15}$	5.62
1	$k_{14}$	-5.05
2	$k_{2x}$	$\pm 1.29$
4	$k_{4x}$	$\pm 2.13$
3 & 5	$k_{3x-5x}$	3.91
6	$k_{6x}$	$\pm 1.46$
7	$k_{7x}$	2.17

Using the values of the twiss parameters at the beginning of the IBL obtained in Sec. 3.2 the  $\beta$  function and the dispersion along the IBL are calculated for the optimized IBL and the results are shown in Fig. 3.17.

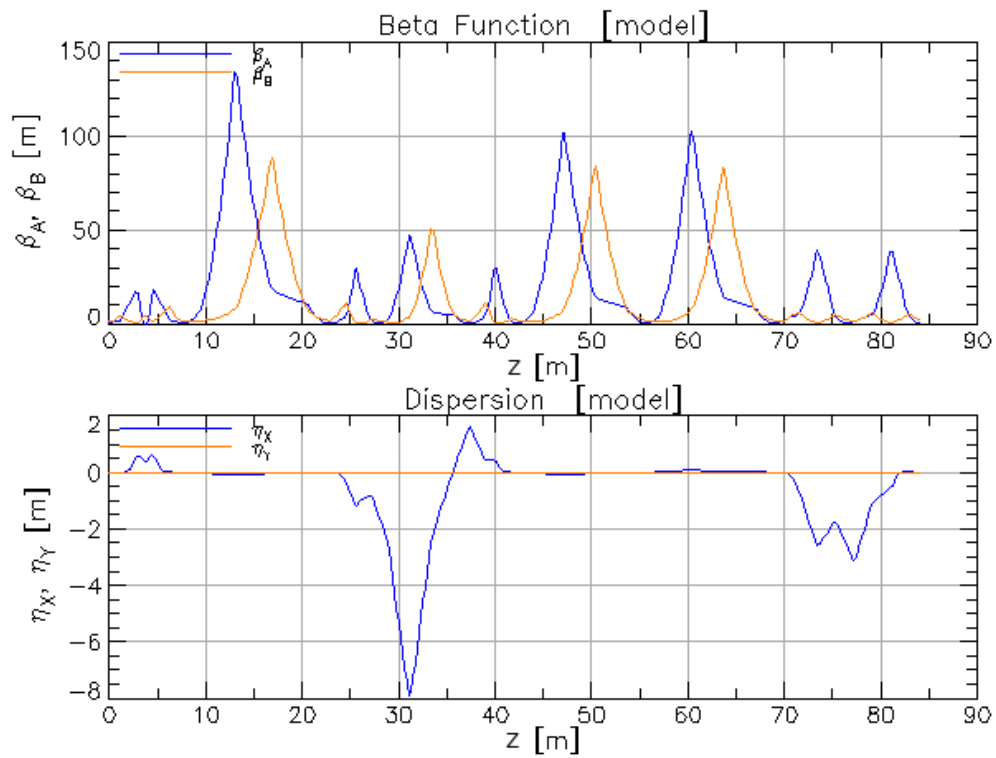


Figure 3.17:  $\beta$  functions and dispersions along the IBL for Optics 1.  $\beta_a = \beta_x$  and  $\beta_b = \beta_y$ .



# Injection Optimization in COSY

This chapter includes the analysis and simulation of the process of injection itself. The last section of the IBL is also included here because it is responsible to match the injected beam parameters to COSY. For the calculations related to the ring an already available model is used, but some meaningful changes are applied.

## 4.1 Injection Dipole and Beam Steering

In Sec. 2.3.1 the purpose of the injection dipole is explained. The injection dipole is one of the 24 dipoles responsible to bend the beam in the ring. Therefore, it has to apply a bending of exactly  $\alpha = 360/24 = 15^\circ$  to the proton or deuteron beam circulating in COSY. It is a rectangular magnet. The beam enters the dipole face with an angle (see Fig. 2.2) of  $7.5^\circ$  and leaves it with the same angle but opposite sign, completing the  $15.0^\circ$  bending. However, the injected beam coming from the IBL enters the injection dipole from one of its sides (see Fig. 2.8). As a consequence, this beam has to go through a long section of fringe fields, which are the field components not described by the simple box approximation of the magnet.

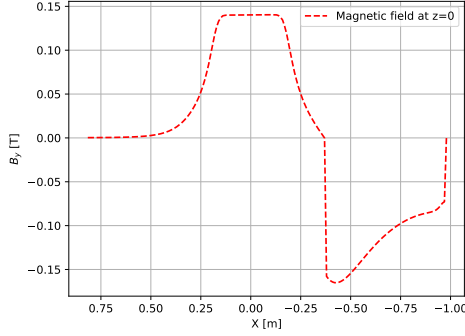
In order to study the effects of these fields in the injected beam, a 3D field map for the injection dipole has been calculated by Jürgen Böker. Placing the origin of the coordinates in the center of the horizontal iron poles, the effective length of the magnet is calculated for the two vertical planes going through the center. Here  $x$  is the direction parallel to the short face of the rectangular magnet and  $z$  is the one parallel to the long face. The coordinate system of the beam is respected, so the positive  $z$  direction points in the COSY beam direction and the positive  $x$  points out of the ring. The effective length is given by:

$$l_{\text{eff}} = \frac{\int B dl}{B_{\text{max}}}. \quad (4.1)$$

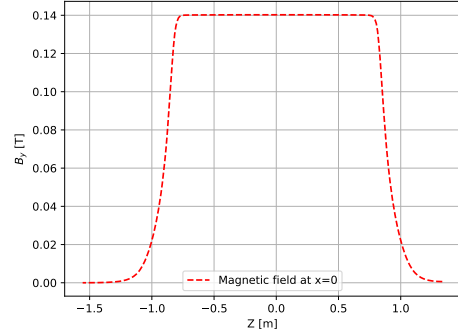
An interpolation between the mesh points of the 3D map is used. The field map is scaled to the warm magnet field maximum value ( $B_{\text{max}} = 0.140\,25$  T). A magnet is called ‘warm’ if it has been previously ramped and contains remnant magnetic fields, otherwise it is defined as ‘cold’. The results are shown in Fig. 4.1. To calculate the effective length in  $x$  only the positive part of the axis is used (see Fig 4.1a) and then symmetry is applied, because the iron of the magnet affects the field shape for negative  $x$  values.

$$l_{\text{eff}-z} = 1.823\,29 \times 10^3 \text{ mm.}$$

$$l_{\text{eff}-x} = 0.499\,51 \times 10^3 \text{ mm.}$$



(a) Vertical field in  $x$  for  $z = 0$ . The left positive peak corresponds to the field that the particle beams experience. On the right side the negative field region corresponds to the return field inside the iron yoke.



(b) Vertical field in  $z$  for  $x = 0$ .

Figure 4.1: Vertical magnetic field component in  $x$  and  $z$ .

Using this same field map the bending angle is calculated for the injected beam and the circulating beam. For both of them the initial position and directions are taken from the ideal orbit direction and angle before entering the dipole magnet. Then, the evolution under the field map is calculated using a fourth order Runge-Kutta method [41] to solve the differential equation given by [42]:

$$\frac{d^2x}{dz^2} = -\frac{B_y(x, z)}{B\rho} \left( 1 + \left( \frac{dx}{dz} \right)^2 \right)^{3/2}. \quad (4.2)$$

The resulting beam trajectories are shown in Fig. 4.2. The circulating beam has an angle of  $e_{\text{COSY}_i} = 7.5^\circ$  with respect to the  $z$  direction when entering the dipole magnet. Here the subscript  $i$  denotes the initial angle, while the subscript  $f$  denotes final one. According to the calculations the output angle is  $e_{\text{COSY}_f} = -7.491^\circ$ , so there is a deficit of  $0.009^\circ$  in the bending of the COSY beam for a warm magnet. This magnitude corresponds to  $0.15 \text{ mrad}$ . If instead the field map is scaled for a cold magnet ( $B_{\text{max}} = 0.1391 \text{ T}$ ), the exit angle from the dipole for  $e_{\text{COSY}_i} = 7.5^\circ$  entering angle is  $e_{\text{COSY}_f} = -7.367^\circ$ . This difference corresponds approximately to  $4.1 \text{ mrad}$ , a considerable gap from the nominal value. Hence, the magnet always needs to be ramped several times when COSY is started to achieve the warm field.

The injected beam has an exit angle of  $e_{\text{injected}_f} = -7.680^\circ$  for a warm magnet. It is clear that if the two beams have to be parallel at the exit of the dipole magnet the bending is not strong enough for the injected beam. The angular difference between two beams at the exit is given by

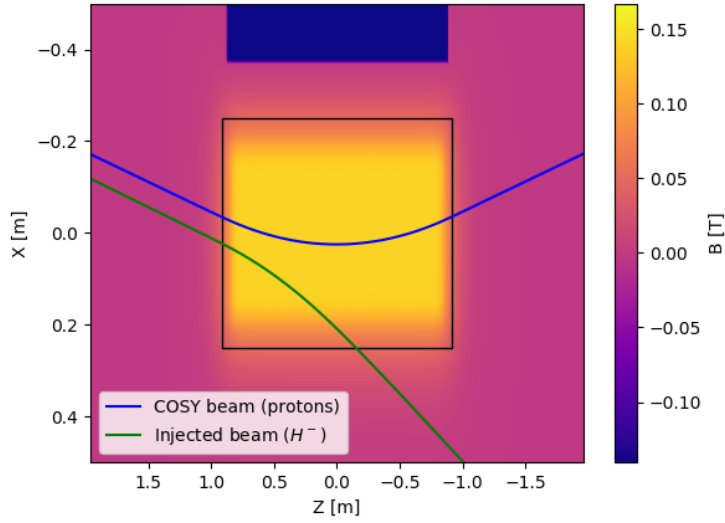


Figure 4.2: Trajectory of circulating beam (blue) and injected beam (green). The black rectangle represents the hard edges of the injection dipole magnet given by the effective lengths in  $x$  and  $z$ . The blue field region at the top represents the return field inside the iron. Both trajectories go from right to the left.

$$e_{\text{COSY}_f} - e_{\text{injected}_f} = 0.189^\circ = 3.2 \text{ mrad.}$$

Furthermore the nominal horizontal distance between the injected beam and the COSY beam at the stripping foil is 50 mm as it is mentioned in Sec. 2.3.1. The calculation using the field map shows that at the location of the stripping foil:

$$\Delta d = 54.5 \text{ mm.}$$

So, assuming ideal conditions at the entrance of the dipole field, the bending angle of the COSY beam is close to the nominal value but the bending of the injected beam is not enough to place both beams in parallel directions. In addition, the distance between two beams is bigger than expected.

#### 4.1.1 Steerer Calibration in the IBL

The horizontal distance between the edge of the stripping foil and the COSY nominal orbit can be manually changed (see Fig. 2.12). Thus, having a injected beam at a different distance from the orbit does not avoid injection but it affects the beam properties: the further the beam is injected from the orbit the bigger the betatron oscillations the particles experience, as it can be derived from Eq. 2.13. As the beam envelope is given by the amplitude of these oscillations (see Eq. 2.27), the big betatron oscillations cause the beam to be wider in  $x$  direction. If the injected beam phase space surpasses the geometrical acceptance of the ring the particles lying outside are lost.

In order to control the distance and angle between the ideal COSY orbit and the injected beam, steerer magnets are placed in the last section of the IBL. These

magnets are calibrated using the viewer located in the stripping foil and two more cameras located along section 8 of the IBL. Three magnets are calibrated: S82, S81A and S84. There is another steerer magnet which was unavailable at the time of the calibration but is now operational: S83. This last one is not calibrated. The calibration is carried out by changing the current intensity going through the magnets and observing how the corresponding kick affects the beam position in the viewers, located at certain distances from the steerer magnets. The results of the calibration are given in Table. 4.1 for H<sup>-</sup> beams. It is straightforward to calculate the equivalent for D<sup>-</sup> beams from those values.

Table 4.1: Results of the steerer calibration for H<sup>-</sup> beams. The sign of the kick uses the same sign convention as Bmad, a positive kick bends a positive beam to the left and vice versa.

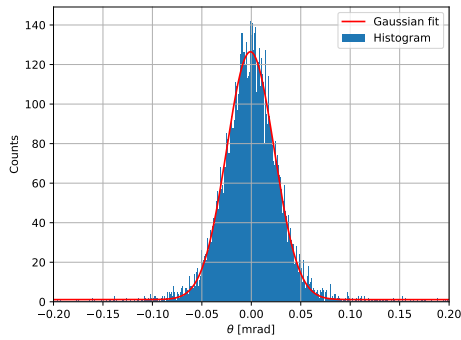
Steerer name	Kick [mrad] / I [%]
S82	$(-3.0 \pm 0.2) \times 10^{-2}$
S81A	$(15.0 \pm 0.4) \times 10^{-2}$
S84	$(-6.5 \pm 0.5) \times 10^{-2}$

This gives the possibility to place the beam in the desired horizontal position and angle with respect to the nominal orbit. It is possible to change the position and not the angle, or to change the angle without changing the position for example. A model is used to do the calculations for the required kicks. The behavior of steerers S82 and S81A is reproducible using the available model for the IBL, but this is not the case for the steerer 84. Steerer 84 is located inside the field of the injection dipole magnet and this interaction is not included in the current model.

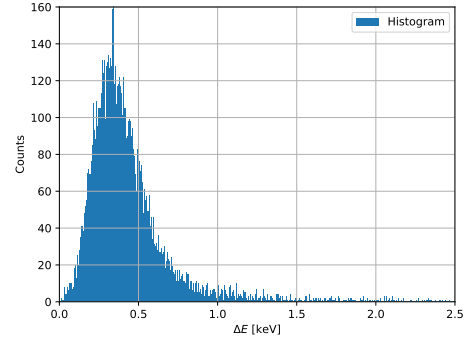
## 4.2 Stripping Foil

The stripping foil has a stripping efficiency of more than 90% for 45 MeV H<sup>-</sup> and D<sup>-</sup> beams [44]. However, if once the beam is injected it hits the stripping foil repetitively the emittance in  $x$  and  $y$  grows according to Eq. 2.48. To get the rms scattering angle and energy loss per passage of the particles through the foil the GEANT4 software is used (see Sec. 1.5).

For the simulations  $10^4$  particles are shot against the  $20 \mu\text{g cm}^{-2}$  C<sup>12</sup> foil. The resulting histograms for the scattering angle in the  $x$  plane and the energy loss for an incident beam of 45 MeV protons are shown in Fig. 4.3. The scattering angle is the same for  $x$  and  $y$  planes, as there is no asymmetry in the scattering (no incident angle is considered). A normal distribution is obtained. For the energy loss a Landau type distribution is observed [43]. The rms scattering angle ( $\theta_{\text{rms}}$ ) in plane and the most probable energy loss caused by a passage through the foil ( $\Delta E$ ) for 45 MeV protons and 76 MeV deuterons are given in Table 4.2.



(a) Histogram of the distribution of the scattered angle in the  $x - z$ -plane. A Gaussian fit to calculate the rms value is shown in red.



(b) Histogram for the energy loss distribution.

Figure 4.3: GEANT4 simulation results for 45 MeV protons.

Table 4.2: Results of GEANT4 simulations for the stripping foil.

	$\theta_{rms}$ [mrad]	$\Delta E$ [keV]
p	$(2.40 \pm 0.02) \times 10^{-2}$	$0.348 \pm 0.002$
d	$(1.45 \pm 0.01) \times 10^{-2}$	$0.408 \pm 0.002$

$\delta_{rms}$  is then calculated using Eq. 2.47. These results are used in Eq. 2.48 for the emittance growth calculation. However, the  $\beta$  functions and the dispersion at the stripping foil are still unknown. For that, a COSY model is presented in Sec. 4.3. The results obtained in the simulations are of the same order of magnitude than the ones obtained using the analytical approximations in Eq. 2.45 and 2.46, with the differences always being smaller than a factor 2. For the following calculations the simulation results are used.

### 4.3 COSY Orbit and Local Bump

The COSY ring is represented in a model in Bmad. The magnet misalignments have been measured this year in COSY and those have been included in the model. The resulting  $\beta$  functions, dispersion and orbit for the injection settings are plotted in Fig. 4.4.

The result shows that at the stripping foil (initial point of  $x$  axis in Fig. 4.4)  $\beta_x = 14.148$  m and  $\beta_y = 7.043$  m. Dispersion vectors are  $(D_x, D'_x) = (6.383$  m, 0.136) and  $(D_y, D'_y) = (-0.018$  m,  $-0.003)$ . Using these values and the results in Table 4.2 the emittance growth per passage through the foil is given by

$$\frac{d\epsilon}{dn} = \frac{1}{2} \left( \beta \theta_{rms}^2 + \frac{D^2}{\beta} \delta_{rms}^2 + \beta D'^2 \delta_{rms}^2 \right) \approx \begin{cases} 4 \times 10^{-3} \text{ mm mrad} & \text{in } x - x' \text{ phase space,} \\ 2 \times 10^{-3} \text{ mm mrad} & \text{in } y - y' \text{ phase space} \end{cases} \quad (4.3)$$

for protons, and

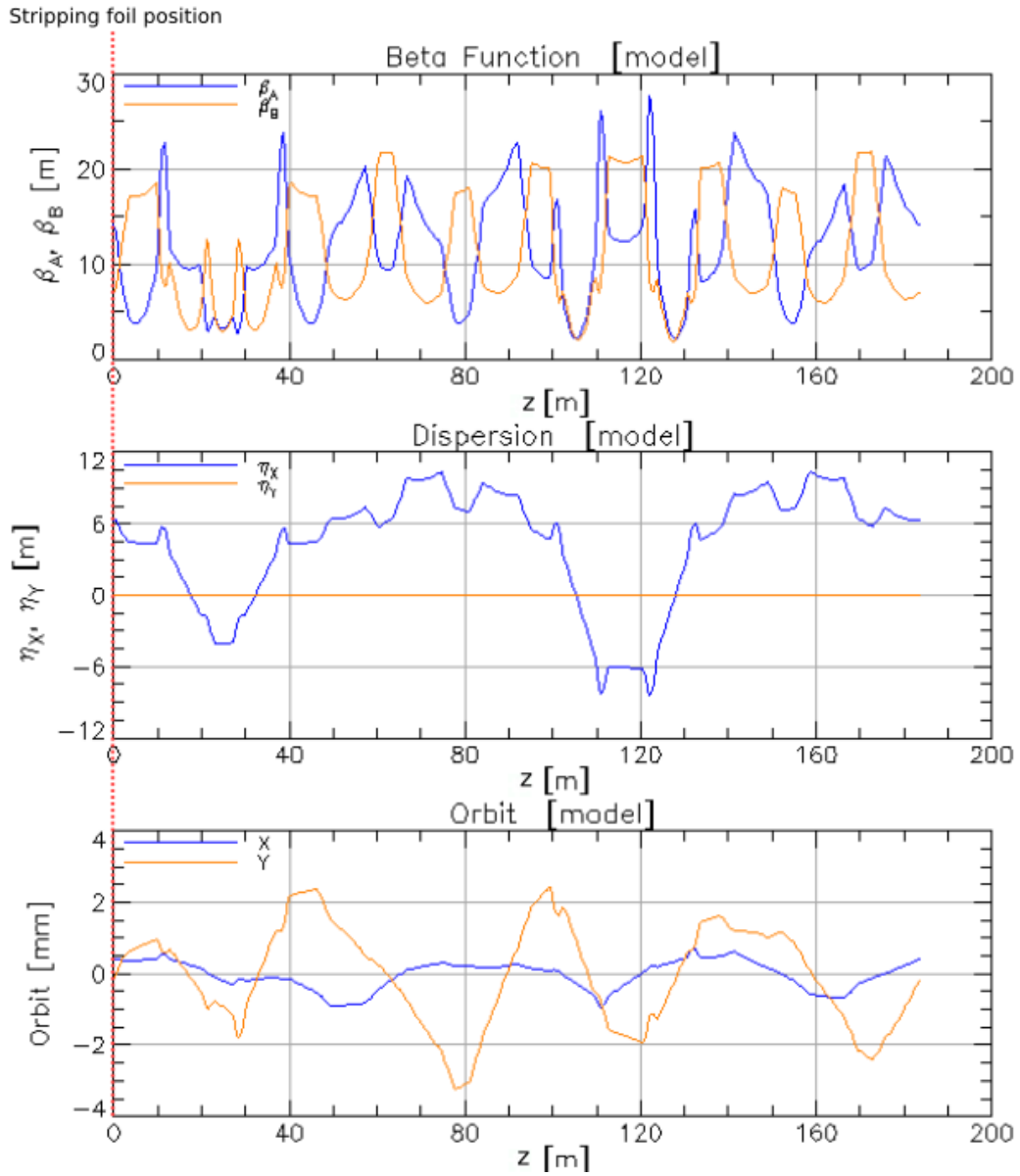


Figure 4.4:  $\beta$  functions (top), dispersion (center) and orbit respect to the ideal lattice orbit (the ideal lattice orbit does not include the magnet misalignments).

$$\frac{d\epsilon}{dn} \approx \begin{cases} 1 \times 10^{-3} \text{ mm mrad} & \text{in } x - x' \text{ phase space,} \\ 1 \times 10^{-3} \text{ mm mrad} & \text{in } y - y' \text{ phase space} \end{cases} \quad (4.4)$$

for deuterons. Furthermore, now that the  $\beta$  values in the stripping foil are known, the optimization for the last section of the IBL is performed to match (as good as possible) those values at injection. The results are given in Table 4.3.

Table 4.3: Results for optimization of the last section in the IBL.

Section #	Variable name	Optics 1 [ $\frac{1}{\text{m}^2}$ ]
8	$k_{81}$	0.42
8	$k_{82}$	1.33
8	$k_{83}$	3.26
8	$k_{84}$	-3.24

### 4.3.1 Injection Orbit Bump

Shifting the COSY orbit horizontally to match the injected beam position is done using three bumper magnets as it is explained in Sec. 2.3.1. The kick required in those bumper magnets depends only on the COSY lattice and is calculated using Eq. 2.42 and 2.43. In the last two equations the matrix elements represent the transfer of the beam from the position of the first bumper to the position of the last one. To create the bump at the injection section of COSY the bumper magnets MBU1, MBU2 and MBU3 are used. The respective kicks are called  $\kappa_{\text{MBU1}}$ ,  $\kappa_{\text{MBU2}}$  and  $\kappa_{\text{MBU3}}$ . In COSY the magnet numbering begins at the stripping foil, so the orbit bump is not created by the magnet MBU1 but by MBU2 (see Fig. 2.7). This happens because the orbit needs to be already shifted at the stripping foil and, thus, it is created by MBU2, then corrected by MBU3 before going through the injection point and is finally closed by MBU1 (see Fig. 4.5) after the stripping foil position. Therefore, to compare with the kicks in Eq. 2.42 and 2.43:

$$\kappa_{\text{MBU2}} = \kappa_1, \quad \kappa_{\text{MBU3}} = \kappa_2, \quad \kappa_{\text{MBU1}} = \kappa_3.$$

In order to have a closed orbit bump in COSY the required relations between the kick strengths are:

$$\frac{\kappa_{\text{MBU3}}}{\kappa_{\text{MBU2}}} = -\frac{a_{12}}{b_{12}} = -0.428, \quad (4.5)$$

$$\frac{\kappa_{\text{MBU1}}}{\kappa_{\text{MBU2}}} = -(a_{22} - \frac{a_{12}}{b_{12}}b_{22}) = 0.531. \quad (4.6)$$

Then, the value  $\kappa_3 = \kappa_{\text{MBU3}}$  determines the amplitude of the orbit bump. In this case, the orbit bump needs to be big enough to reach the stripping foil edge, where the injected beam is located. The position of the injected beam can be changed using the steering magnets S82, S81A and S84 and, in addition, the stripping foil can be manually displaced to different distances from the nominal orbit. The result for a 50 mm shift in the positive  $x$  direction is shown in Eq. 4.7:

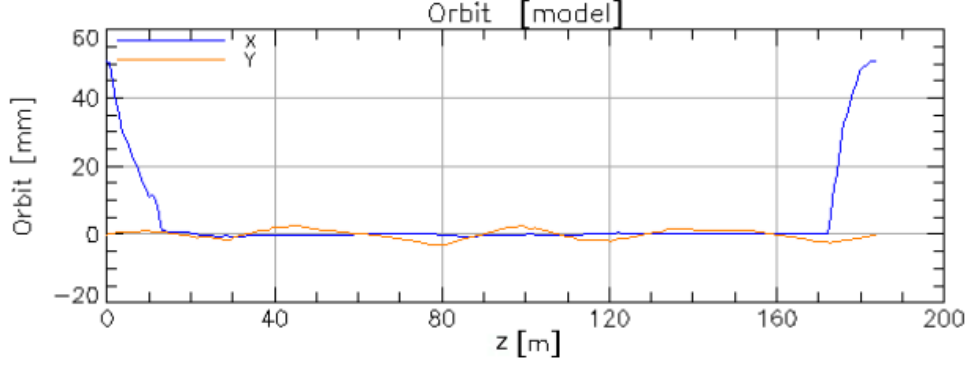


Figure 4.5: Orbit bump at injection section in COSY.  $z = 0$  m is the stripping foil position. MBU2 is located at  $z \approx 172.1$  m and it kicks the orbit horizontally. MBU3 is located at  $z \approx 179.6$  m and corrects the bump in order to have a 50 mm offset in the stripping foil. Finally, MBU1, which is located at  $z \approx 13.1$  m, closes the bump and returns the orbit to its original position.

$$\kappa_{MBU3} = 8.139 \text{ mrad}. \quad (4.7)$$

The orbit bump is then shown in Fig. 4.5. However, even if the amplitude of the bump can be controlled, it is not possible to do so with the angle, because only three bumper magnets are available. The linear relation between the orbit bump amplitude in the stripping foil and the angle respect to the ideal orbit is shown in Fig. 4.6.

The amplitude chosen for the bump is given by the distance from the stripping foil edge to the COSY beam orbit. At the beginning the orbit is shifted inside the stripping foil. After the injection begins the bump is reduced linearly from the original shift value to zero, as explained in 2.3.1. Then, the time the beam in COSY hits the stripping foil is given by how far its edge is placed from the orbit and how deep does the orbit go inside the stripping foil. Hence, the time the beam center spends inside the stripping foil is given by

$$t_{\text{in}} = \Delta l_{\text{in}} \frac{t_{\text{mac}}}{\Delta l_{\text{tot}}} = (\Delta l_{\text{tot}} - \Delta l_{\text{out}}) \frac{t_{\text{mac}}}{\Delta l_{\text{tot}}}, \quad (4.8)$$

where  $\Delta l_{\text{tot}}$  is the bump amplitude,  $\Delta l_{\text{out}}$  is the distance between the nominal orbit and the foil edge and  $t_{\text{mac}}$  is the injection macro-pulse duration (as long as it is kept at the same value as the ramping down of the bumper magnets). A sketch of the horizontal orbit bump can be seen in Fig. 4.7.

Thus, the number of revolutions the beam hits the stripping foil is given by  $n = t_{\text{in}} f_{\text{rev}}$ . The emittance growth because of the beam-foil interaction is given by the product of  $n$  with Eq. 4.3 or Eq. 4.4, depending on the beam composition. As the intention is to fill the acceptance phase space of COSY with the injected beam the emittance growth because of beam-foil interaction is not a desirable effect. Thus, the orbit bump has to be calculated to hit the foil on the edge so that it minimizes  $\Delta l_{\text{in}}$  and consequently also  $t_{\text{in}}$ . In addition, the further the stripping foil edge is located from the nominal orbit the smaller is  $t_{\text{in}}$ , but then the betatron oscillations

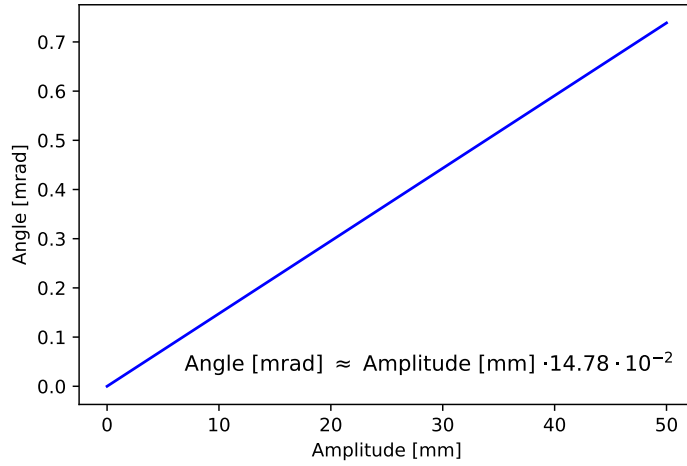


Figure 4.6: Orbit bump angle respect to the ideal orbit as a function of its amplitude.

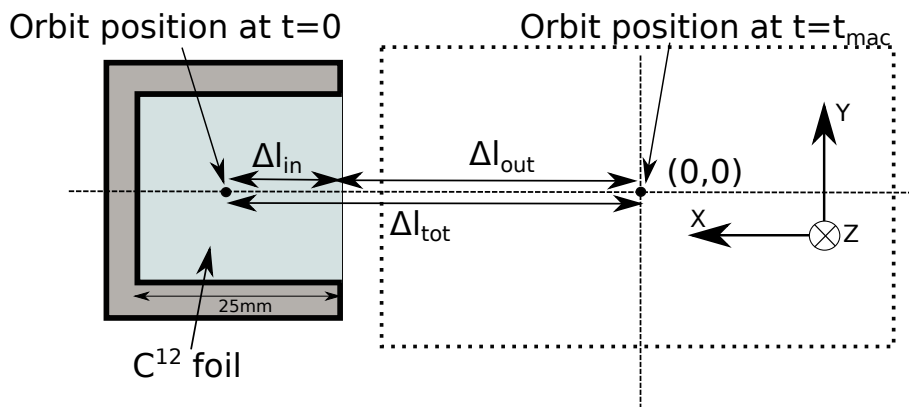


Figure 4.7: Orbit bump parameters.  $t = 0$  is the beginning of the injection process and  $t = t_{\text{mac}}$  corresponds to the end.

of the injected particles become bigger as it is mentioned in Sec. 2.3.1. This also causes emittance dilution effects to be bigger (see Fig. 2.11).

## 4.4 COSY Acceptance

In Sec. 2.2.2 the geometrical acceptance of an accelerator is defined. However, this is not the only definition of the acceptance. Due to different effects which are not considered in the simple definition given by Eq. 2.34, the initial phase space area given by the particles which survive over a certain amount of time in an accelerator is also known as acceptance or admittance. The time the particles need to survive in the accelerator in order to be considered inside the admittance definition is given by the process of interest. For example, for injection it is enough to consider the short term admittance, which is given by the initial phase space of the particles surviving for a few thousand revolutions in the ring. For processes in which long beam lifetime is essential, long term admittance is considered. From now on, the term acceptance denotes the short term admittance of the ring.

For the acceptance calculation  $10^4$  particles are initialized in random phase space locations, at  $\pm 100$  mm and  $\pm 10$  mrad horizontally and vertically from the ideal close orbit at the stripping foil. The  $x$  and  $y$  phase spaces are considered to be decoupled. This is a good approximation for COSY at injection, since there are no longitudinal field components that would couple both phase spaces. The particles are first tracked during  $10^4$  revolutions around the ring using Bmad. It is observed that most of the particles are lost within the first 10 revolutions. Then, the number of particles is increased to  $40 \times 10^3$  but the number of revolutions in the ring is reduced to 50, because it consumes a lot of computational time. The resulting short term admittance for the lattice including the magnet misalignment is shown in Fig. 4.8.

The area of the phase space ellipses from Fig. 4.8 is

$$A \approx \begin{cases} 261 \cdot \pi \text{mm mrad} & \text{in } x - x' \text{ phase space,} \\ 42 \cdot \pi \text{mm mrad} & \text{in } y - y' \text{ phase space.} \end{cases} \quad (4.9)$$

However, when the orbit is horizontally bumped to the position of the injected beam the acceptance also changes with the bump. The evolution of the horizontal acceptance for different orbit bump sizes is shown in Fig. 4.9.

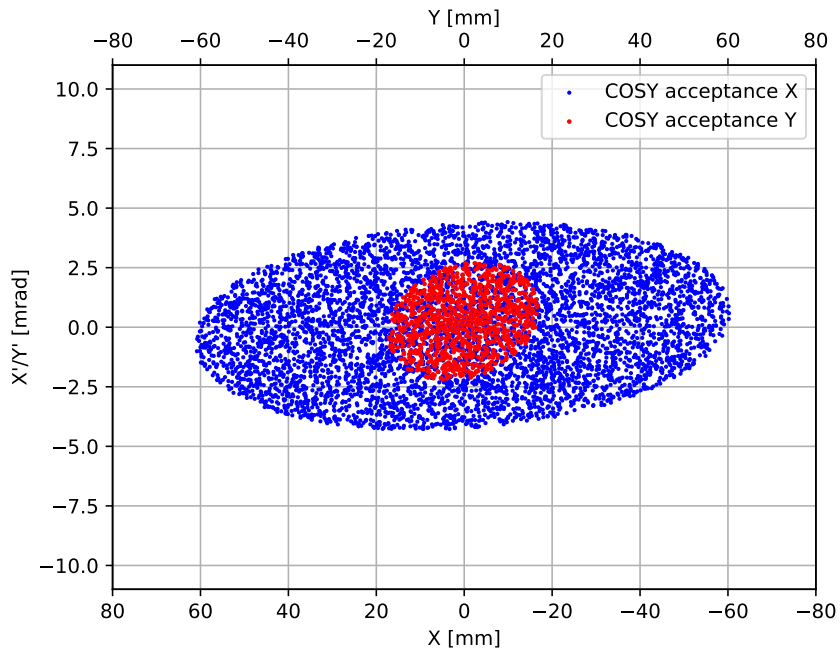


Figure 4.8: Short term admittance of COSY in  $x$  and  $y$  phase spaces.

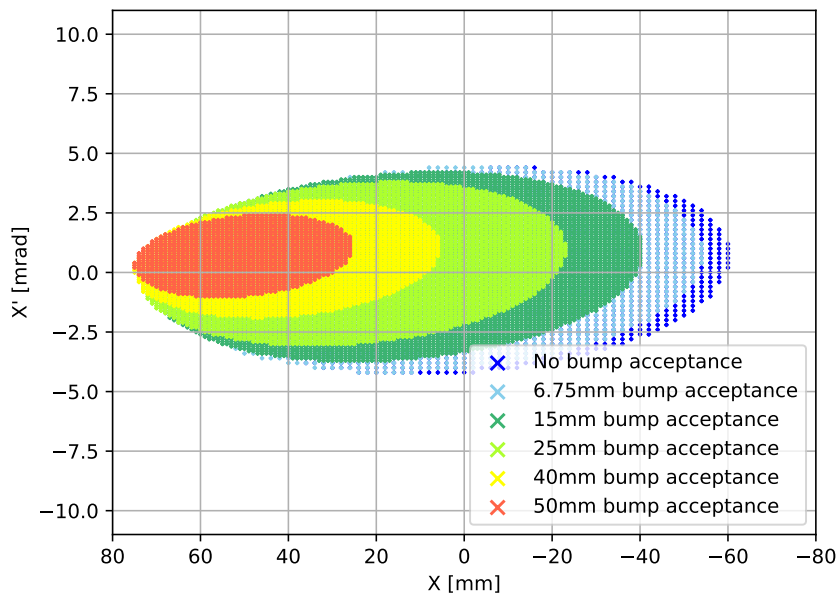


Figure 4.9: Horizontal admittance of COSY for different bump sizes.



# Results

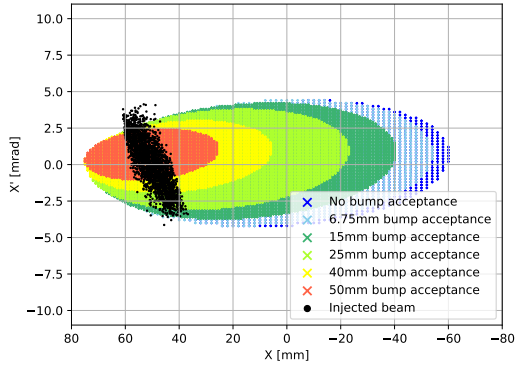
## 5.1 Phase Space Filling

On the one hand, the settings of the IBL are fixed by the optimization and the beam initial conditions are calculated by the emittance measurements (Chapter 3). On the other hand, the COSY acceptance is calculated for different horizontal bumps (Chapter 4). Then, it is finally time to inject the beam in COSY. The filling of the horizontal acceptance of COSY is done by phase space painting, as it is mentioned in Sec.2.3.1. The orbit bump horizontally shifts the center of the acceptance ellipse as seen in Fig. 4.9. When the bump is maximum and the injected beam and the orbit are in the same position, the injected beam phase space center matches the center of the COSY acceptance ellipse. This matching of the centers is not perfect, because the angle of the bump can not be controlled with three bumper magnets (see Fig. 4.6) and this shifts the phase space ellipse also in  $x'$  direction. This problem can be corrected with the steerers in section 8 of the IBL (explained in Sec. 4.1.1) and both beams can be matched in position and angle. As the bump decreases, the center of the COSY acceptance ellipse shifts. However, the injected beam phase space center stays in the same position as the injected beam does not move. Then, the particles are continuously injected in different acceptance areas. The sketch of the process can be seen in Fig. 2.10.

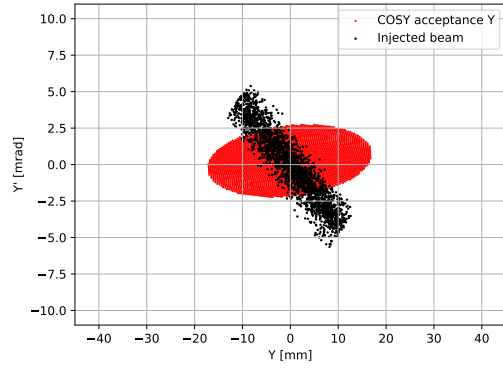
In respect to the vertical direction, the position of the phase space of the injected beam and the acceptance do not move from each other, because the orbit is not bumped vertically. Thus, the injection in the vertical plane is simpler as long as both beam positions are matched together in the stripping foil. The superposition at the stripping foil of the injected beam phase space ellipse under the optimized settings of the IBL (Optics 1 in Table 3.4 and 4.3) and the short term admittance of COSY is shown in Fig. 5.1 for both  $x$  and  $y$  axis. It can be seen that part of the beam falls inside the acceptance, but a non-neglectable amount of particles are injected out of it, being lost.

### 5.1.1 Matching of the Twiss Parameters

There is, however, a problem in the matching. Together with matching the values of  $\beta$  at injection,  $\alpha$  and the dispersion vectors ( $D, D'$ ) are also needed to be matched. How the mismatch of any of these parameters affects the emittance of the injected beam is given by M. Syphers in [33]. The problem in this case is that it is not possible to optimize each section individually and at the same time match all the



(a) Phase space matching for  $x$  axis.



(b) Phase space matching for  $y$  axis.

Figure 5.1: Simulated phase space matching of the injected beam with COSY acceptance. The optimized IBL settings and the calculated beam properties are used. The injected beam shown here is the evolution of the one shown in Fig. 3.12 after the transfer along the IBL.

parameters for both phase spaces. For the results in Table 4.3, only  $\beta$  functions are matched using section 8 of the IBL, while the mismatch in  $\alpha$  is also minimized. The dispersion vector is not considered. If all the quadrupoles in the IBL are varied with the goal of matching the twiss parameters and dispersion vector, but not to optimize the sections, it is possible to achieve a full matching of the IBL to the ring. The resulting quadrupole strengths are given in Table 5.1. The superposition of the emittance of the injected beam for such optimization with the acceptance of COSY in  $x$  and  $y$  is shown in Fig. 5.2. These calculations are done using Eq. 3.41 as a model of the injection dipole in the simulations. This model may have to be further studied in the future.

Table 5.1: IBL quadrupole strengths for  $\beta$ ,  $\alpha$ ,  $D$  and  $D'$  matching in the stripping foil.

Section #	Variable name	Matched optics [ $\frac{1}{m^2}$ ]
1	$k_{11-17}$	0.62
1	$k_{12-16}$	-0.91
1	$k_{13-15}$	1.63
1	$k_{14}$	-4.61
2	$k_{2x}$	-1.11
4	$k_{4x}$	2.11
3&5	$k_{3x-5x}$	1.62
6	$k_{6x}$	0.89
7	$k_{7x}$	0.51
8	$k_{81}$	1.29
8	$k_{82}$	-0.85
8	$k_{83}$	1.79
8	$k_{84}$	-2.13

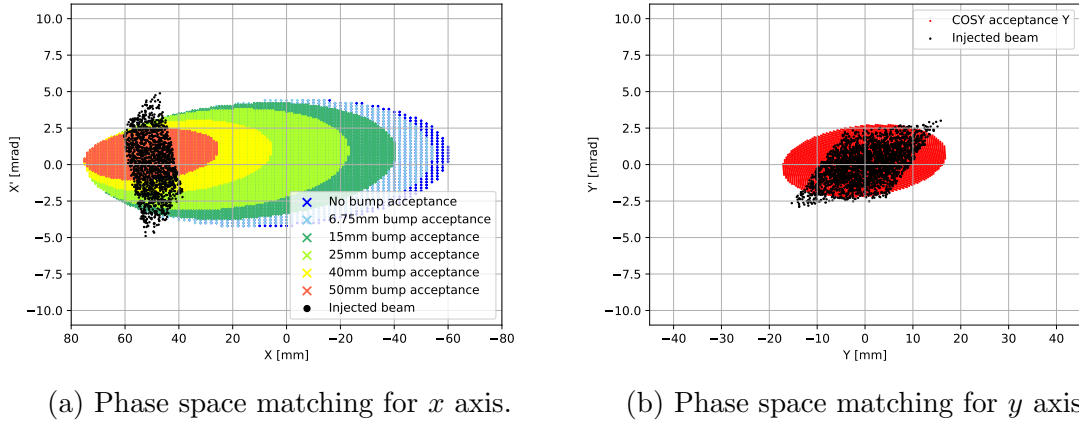


Figure 5.2: Simulated phase space matching of the injected beam with COSY acceptance. The IBL settings from Table 5.1 are used in this case.

## 5.2 Model Testing

In order to test the models of the IBL and COSY and apply the results of the studies in Chapters 3 and 4, different experiments were performed during several beam times in May and June.

Starting from the beginning of the trajectory of the particles from the cyclotron to the ring, the first thing is to analyze the emittance measurements carried out at the beginning of the IBL. Both measurement methods, the quadrupole scan method (3.1.1) and the slit method (3.1.2), are independent. The results in  $x$  are compatible within the uncertainties for both methods, while the results in  $y$  are within  $4\sigma$  from each other. However, the previously expected values for the emittances of the beam at the exit of the cyclotron lay around  $\epsilon_x = 3.3 \text{ mm mrad}$  and  $\epsilon_y = 6.6 \text{ mm mrad}$ . Thus, the measured values are larger than the expected ones. Those expected values are for  $\text{H}^+$  beams and the measurements are carried out using  $\text{H}^-$  beams, hence the origin of the difference could come from the ion sources or the cyclotron. The  $\text{H}^+$  ion source is not longer operational. Therefore, it is not possible to test the emittance measurement methods.

The IBL is optimized using the initial conditions of the beam calculated with the results of the emittance measurements. Then, the optimization of the IBL is tested. First of all, the optimization results are applied to the FODO sections 2,4 and 6. It is confirmed that sections 2,4 and 6 produce an imaging of the beam with  $\pi$  or  $2\pi$  phase advances under the optimized conditions. When applying the optimization results to the rest of the sections in Table 3.4, however, the beam does not reach the stripping foil. The reason behind this may be that the quadrupoles in the IBL are not only used to focus or defocus the beam, but also to steer it. This happens when the beam is not traveling through the center axis of the quadrupole. Therefore, when the quadrupole settings are changed the kick received by the beam is also different. This may cause the beam to hit the vacuum pipe walls. In order to test the full optimized IBL settings the beam coming from the cyclotron needs to be aligned with the quadrupole center axis. There is another observed issue related

to the maximum current provided by the power supply for QI83 and QI85. Even if theoretically the value of  $k_{13-15}$  in Table 3.4 is within the limits of the power supply, an error pops up when trying to set this value.

Many calculations in Chapter 4 are dependent on the COSY model. This model exists for many years, but some changes have been made during this work. The main change is to include the misalignment of all the magnets in the ring. The ring settings for injection are extracted from the COSY control room and then simulated. In order to check the validity of the model, the tune (see Sec. 2.2.3) and momentum compaction factor (see Eq. 2.23) are calculated and also measured in COSY. The results of the tunes and the momentum compaction factor for the simulated machine are:

$$Q_x = 0.536, \quad Q_y = 0.709, \quad \alpha = 0.270, \quad (5.1)$$

where  $Q_x$  and  $Q_y$  represent the fractional tune (only the decimal part of the tune is used, because the integer part is not needed to calculate the working point shown in Fig. 2.4). The momentum compaction factor,  $\alpha$ , is approximated by calculating the sum of the product between the dispersion function value in each dipole magnet and the bending angle of the same dipole magnet. The result of the sum is finally divided by the total length of COSY. On the other hand, the fractional tune measurement is automatized in COSY and yields a result of

$$Q_x = 0.566 \pm 0.007, \quad Q_y = 0.637 \pm 0.002. \quad (5.2)$$

At the same time the momentum compaction factor is measured by changing the intensity through the magnetic dipoles after injection and then measuring the change in the revolution frequency of the particles. According to [45] the change in frequency is given by

$$\frac{\Delta f_{rev}}{f_{rev}} = \frac{1}{\gamma^2} \frac{\Delta p}{p} - \frac{1}{\gamma_{tr}^2} \left( \frac{\Delta p}{p} - \frac{\Delta B}{B} \right) - \frac{\Delta R_0}{R_0}, \quad (5.3)$$

where  $\gamma$  is the relativistic Lorentz factor and  $\gamma_{tr}$  is the transition  $\gamma$ , an important parameter of the ring when accelerating particles. As the only variable changed for the measurement is the magnetic field, the rest of terms vanish and the final relation reads  $\frac{\Delta f}{f} = \frac{1}{\gamma_{tr}^2} \frac{\Delta B}{B}$ . The measured curve can be seen in Fig. 5.3. The slope of the curve directly gives the value for  $\alpha$ , as  $\alpha = 1/\gamma_{tr}^2$ . The fit in Fig. 5.3 gives a result of

$$\alpha = 0.292 \pm 0.006. \quad (5.4)$$

Hence, the measured values of  $Q_x$ ,  $Q_y$  and  $\alpha$  at injection do not match the values calculated using the model and the discrepancies are of

$$\frac{\Delta Q_x}{Q_{x\text{-measured}}} = 0.05, \quad \frac{\Delta Q_y}{Q_{y\text{-measured}}} = -0.11, \quad \frac{\Delta \alpha}{\alpha_{\text{measured}}} = 0.07. \quad (5.5)$$

Thus, the model is not a completely faithful description of the machine and improvements are needed. It could be that the quadrupole strengths used for the simulation do not match the real ones because of some discrepancies in the calibration factors. Another possibility is that the effective lengths of the magnets are affected by the

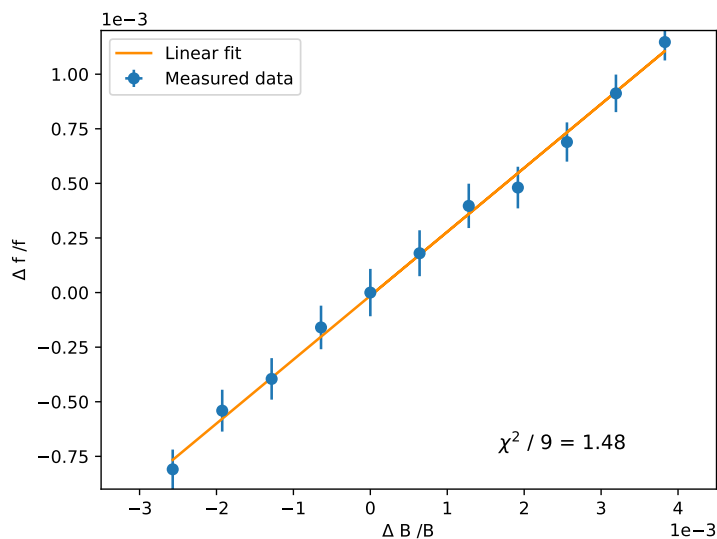


Figure 5.3: Relation between the change of magnetic field in the dipoles with the measured change in revolution frequency.

cross talking of the magnetic fields with neighboring magnets. This is briefly studied in [46] and a discrepancies of up to 0.26% in the effective length are found for dipoles with a steering magnet placed very close to them. This would affect the bending angle of those dipoles in around 1 mrad. There are dipoles in the ring sandwiched between two steering magnets, so the effect would be doubled. In order to check this the orbit in COSY is measured at injection and is shown in Fig. 5.4.

This orbit is compared with the orbit calculated with the model including the misalignment of the magnets (see Fig. 4.4) and big discrepancies of up to 25 mm are found in the horizontal orbit. The measured orbit has a displacement towards the outside of the ring in the arcs and it is more balanced in the straight sections. The steerer magnets in the ring are off when the orbit is measured, so they can not be blamed for the discrepancies. Thus, the hypothesis that the dipoles bend the beam less than required could be accurate, but more measurements are needed to reach any definitive conclusion.

Fig. 5.4 also shows that for  $z = 0$  m the orbit is already out of the ideal axis for a bit less than 7 mm in the vertical direction and for around 20 mm in horizontal one, without any bump. When trying to replicate this orbit in the injection section (in the region of the last 4 dipoles of the arc section in which injection happens, from  $z \sim 171$  m to  $z \sim 10$  m) with the model, different strength horizontal kicks are introduced in the dipole center positions (only in the ones with steering magnets close to them). The results show that in order to get the same orbit in the simulation as the measured one, those kicks would need to be

$$\kappa_{BE21} = 0.12 \text{ mrad}, \quad \kappa_{BE22} = 1.16 \text{ mrad}, \quad \kappa_{BE24} = 1.51 \text{ mrad}, \quad (5.6)$$

where  $BExx$  is the designation for the dipole number  $xx$ . These numbers are compatible with the hypothesis of the effective length shortening.

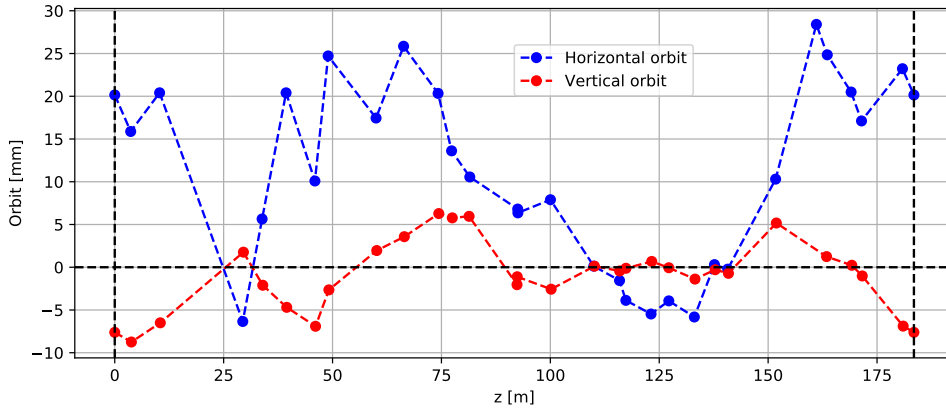


Figure 5.4: Measured horizontal (blue) and vertical (red) orbits at injection in COSY. The horizontal axis of the plot shows the position in the ring, being the left corner  $z = 0$  m the stripping foil position and the right corner  $z \approx 184$  m the end of the ring.

### 5.2.1 Injection Optimization

During these beam times the optimization of the injection process is also tested. Proton beams were available for this beam time. COSY is set at the same conditions as in the acceptance simulations of Fig. 4.9 because those are the usual injection parameters and the calculated acceptance is optimum in those injection conditions (see Fig. 5.2). On the other hand, the optimized conditions of the IBL cannot be applied because the beam is lost in the transfer line as explained in the previous section. Thus, it is decided to keep the quadrupole strengths as in the previous beam times. Then, as the orbit bump builds upon the already existing base orbit, taking into account that the non-bumped orbit is shifted as seen in Fig. 5.4 the bump amplitude to reach the same position has to be smaller than for the case of an ideal orbit.

The injected beam position can be observed with a viewer placed in the stripping foil. For the circulating beam, however, the current induced in the stripping foil has to be used as an indirect measurement. When the circulating beam is bumped for injection it hits the stripping foil and current is induced in it. The measured current tells if the bump is hitting the foil, but not the certain position of the bumped orbit. Thus, relying on the model calculations from Sec. 4.3.1, the orbit is bumped by 35 mm, which added to the already existing 20 mm horizontal offset give a total of 55 mm offset in the stripping foil. The edge of the foil is then placed at 52.5 mm horizontally from the nominal orbit position. Then, looking at the injected beam in the viewer, the steerers in the end of section 8 of the IBL are tuned to match the position of the injected beam horizontally with the calculated bumped orbit position. The measured current in the foil is shown in Fig. 5.5. The vertical position matching with the orbit of Fig. 5.4 is also taken into account using the vertical steerers located along the IBL.

Fig. 5.5 shows that the beam hits the stripping foil for a long time during the injection macro-pulse. This leads to emittance increases given by the product of the

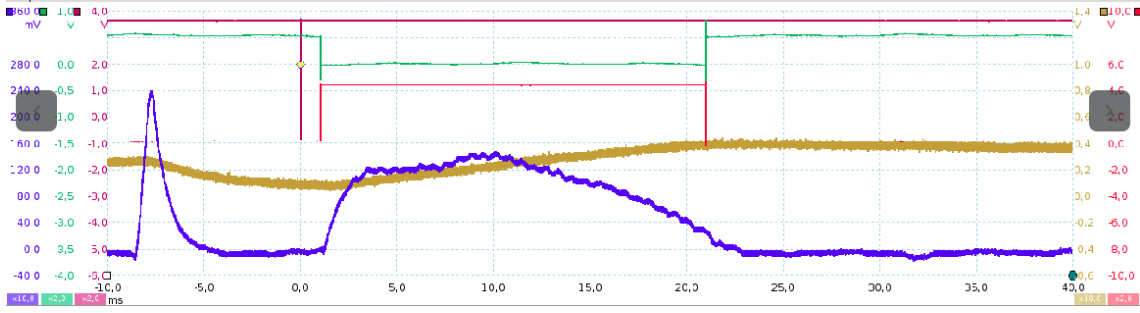


Figure 5.5: Screenshot of the foil current (blue line) together with the injection macro-pulse (red line) and the current measured in COSY (brown line). The sharp foil current peak in the left coincides in time with the ramping up of the bumper magnets. Thus, it means that the beam stored in the ring from a previous injection cycle hits the foil and it is lost, that is why the current in COSY decreases at the same time. When the injection starts (macro-pulse is set to the binary value 1) the particles start to be injected, so the current in COSY starts increasing together with the current in the foil, because the orbit is bumped so the cycling beam is hitting the foil. As the bump goes down with time the intensity of the foil current decreases because the orbit is shifting away from it. However, this decrease is slow because even if the beam center is no longer in the foil position, the outer regions of the beam can still be hitting it. When the injection macro-pulse is finished there is no orbit bump already and the foil current vanishes. From that point the intensity measured in COSY does not increase anymore.

revolution number and the values calculated in 4.3. As an approximation, for  $5 \times 10^3$  revolutions hitting the foil (half of the injection macro-pulse) an emittance increase of 20 mm mrad and 10 mm mrad is expected in  $x$  and  $y$  phase spaces respectively. Comparing to the acceptance values in 4.9 the emittance growth is significant but not too large. However, it has to be taken into account that the direction of the emittance growth is not determined by the acceptance, so particles are lost even if the magnitude of the emittance growth does not surpass the magnitude of the acceptance area.

The spread on the measured revolution frequency shows a value of  $(\Delta p/p)_{rms} = 0.3\%$  for a injection dipole current of 312.2 A, as expected for a longitudinally filled acceptance of  $\Delta p/p \sim 0.6\%$  (calculated by dividing the vacuum pipe radius with the maximum dispersion in the ring). The filling of the longitudinal acceptance is performed by the energy losses when hitting the stripping foil. If a particle losses too much energy it is also lost. Finally, under these settings the intensity shown in Fig. 5.6 is obtained in COSY. At the end of the 2s cycles, the maximum measured intensity is of 4.04 mA. This corresponds to around  $5.41 \times 10^{10}$  particles in the ring. The maximum values at injection peaks are of 5.0 mA, which corresponds to around  $6.25 \times 10^{10}$  particles injected. These measurements are carried out for an intensity of  $1.8 \mu\text{A}$  in BC81 (the last Faraday cup in the IBL before the stripping foil) which corresponds to  $22.4 \times 10^{10}$  particles reaching the end of the IBL. Using the letter  $f$  to denote efficiency, defined as the ratio between the maximum number of particles in the ring and the particles reaching the end of the IBL:

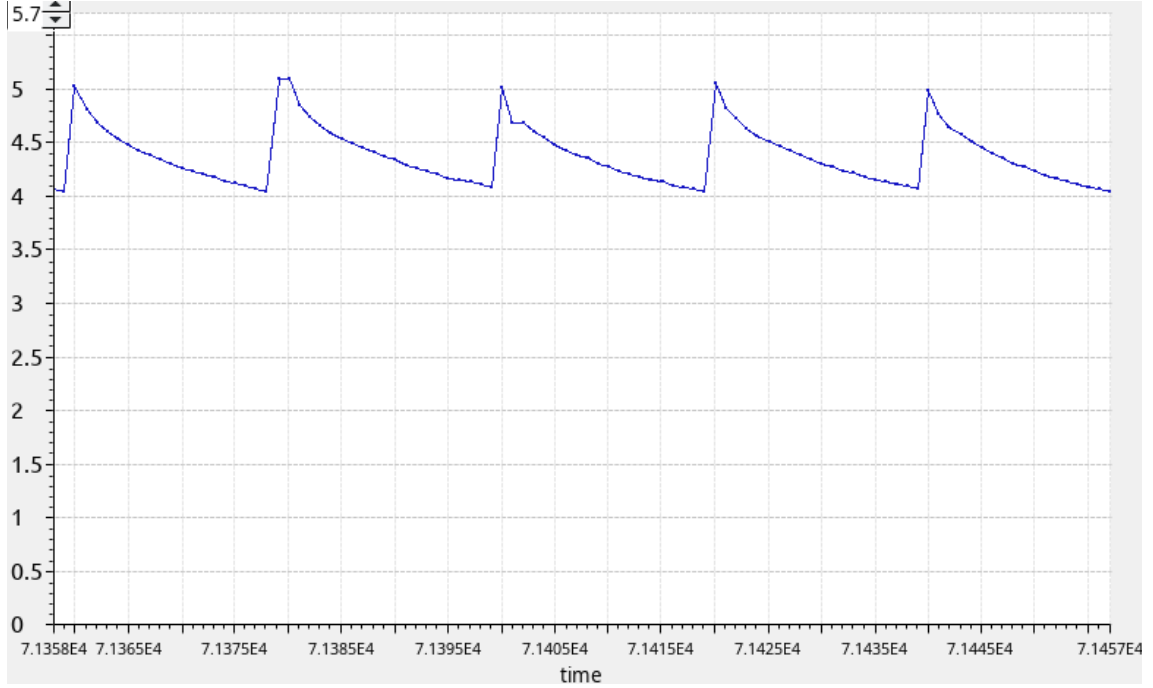


Figure 5.6: Screenshot of the measured intensity in COSY for 2s cycles. The  $y$  axis shows the current in mA.

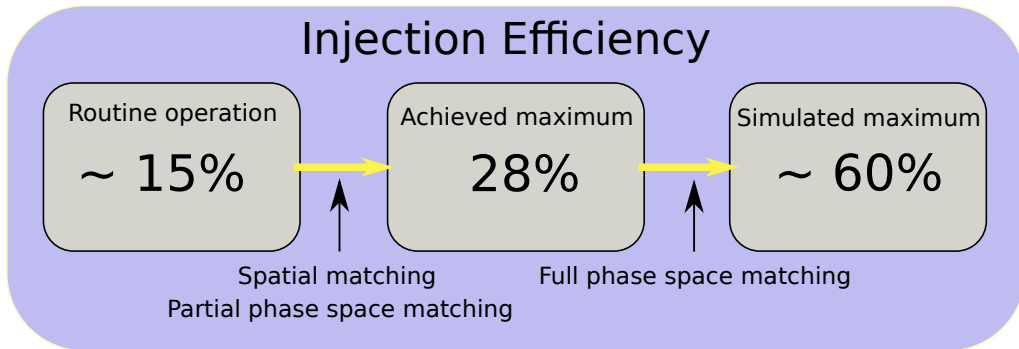


Figure 5.7: Injection efficiencies for different cases.

$$f_{\text{Injection}} = \frac{6.25 \cdot 10^{10}}{22.4 \cdot 10^{10}} = 27.9\%. \quad (5.7)$$

This result shows a very similar injection efficiency than the maximum value of  $f_{\text{Injection}} = 28\%$  achieved in 28/05/2003. As it can be seen in Fig. 5.7, this is superior to the average injection efficiency by a factor  $\sim 2$ , but looking at Fig. 5.1 and 5.2 it can be seen that an efficiency of around 60% (before taking into account the losses in the stripping foil) can be achieved if the position of the beams and the twiss parameters at injection are matched properly. This value is calculated using the simulation results and approximating the number of particles from the emittance of the injected beam that fall inside the acceptance for different orbit bumps during the process. The reason behind the achievement of a lower injection efficiency than the calculated maximum injection efficiency (roughly by a factor 2) is believed to be the impossibility to set the optimized quadrupole strengths in the IBL (Table 3.4) without losing the beam.

## 5.3 Outlook

It is clear that injection studies have to continue in order to increase injection and capture efficiency in the ring. Injection is a complex process and its optimization involves many knobs that have to be all optimized together. The further development of the project could include the following aspects:

- As a first step, the calculated injection dipole transfer matrix could be reviewed. Using the current model for the injection dipole, when the sections in the IBL are optimized according to the design specifications, the twiss parameters and dispersion cannot be matched to the COSY values by using section 8 of the IBL. Furthermore, varying also the first section in order to match the twiss parameters is an interesting idea, but then the achromaticity and the unitarity of the transfer matrix for this section would be lost.
- The optimization of the IBL could be properly applied. This requires a dedicated beam time of several days, in which the beam coming from the cyclotron is aligned with the axis of the IBL, thus the quadrupole strengths can be freely varied without steering the beam. The effect of this optimization in the injection efficiency is believed to be positive.
- Then, the COSY model could be further improved. This could include but not be limited to analyze the effect of neighboring magnets in the effective lengths. The more accurate the model is the better the simulated acceptances and orbit bumps will match the reality.
- Having a flat horizontal and vertical orbit at injection would be very helpful to match the position of the injected beam with the bumped orbit in COSY. This requires to use the COSY steerers at injection to correct the orbit. The beam based alignment research being currently carried out is also essential to measure the real orbit of COSY and then be able to calculate the necessary orbit bump accordingly.
- Finally, the injection process itself can be slightly changed. Instead of injecting 50–55 mm away from the nominal orbit, smaller distances can be considered. This would require a smaller orbit bump in order to match the injected beam and the orbit spatially. Therefore, the acceptance of the ring would not shrink as much as seen in Fig.4.9 and this could lead to a better injection efficiency.



# Acknowledgements

First of all I would like to express my most sincere gratitude to Prof. Dr. Jörg Pretz for giving me the opportunity to work in this thesis and for introducing me to the exciting field of the Electric Dipole Moment search. I would also like to thank the staff from the Nuclear Physics Institute (IKP) in Forschungszentrum Jülich, specially Jochen Stein for his dedication and availability, but also everyone else who has helped me during this year: Sig Martin, Nils Fröhlich, Yury Valdau, Ralf Gebel, Andreas Lehrach, Alexander Nass, Vsevolod Kamerdzhev, Raimund Tolle and Olaf Felden, together with many others. In addition, I am greatly indebted with the Ph. D. students Vera Poncza and Marius Rimmler for all their advice and discussions. I cannot forget to mention my fellow students in IKP for making the commute to Jülich enjoyable every day and for the endless lunch and coffee breaks we have spent together. Furthermore, I need to express my appreciation to Prof. Dr. Christopher Wiebusch for acceding to be the second supervisor of this work.

Finally, I want to thank my parents for all the support they have given me and the effort they have made during the last years. They have made possible for me to be here today following my goals without worrying about anything else than physics. Nothing of this would have happened without their financial and emotional aid.



# List of Figures

1.1	PT transformation . . . . .	3
1.2	COSY facility sketch . . . . .	6
1.3	Source sketch . . . . .	7
1.4	Polarized source sketch . . . . .	8
1.5	Cyclotron classes . . . . .	9
1.6	IBL sketch. . . . .	10
1.7	COSY ring . . . . .	11
2.1	Frenet-Serret coordinate system. . . . .	14
2.2	Face angles . . . . .	17
2.3	Phase space ellipse . . . . .	20
2.4	Tune diagram . . . . .	22
2.5	Orbit bump theory . . . . .	23
2.6	General injection . . . . .	25
2.7	COSY injection sketch . . . . .	27
2.8	COSY injection dipole . . . . .	28
2.9	Injection macro-pulse . . . . .	29
2.10	Phase space filling sketch . . . . .	29
2.11	Emitance dilution . . . . .	30
2.12	Horizontal view of injection . . . . .	30
3.1	Quadrupole scan sketch . . . . .	34
3.2	Beam profiles at MWPC . . . . .	34
3.3	Beam size squared . . . . .	35
3.4	Phase ellipse and beam matrix elements . . . . .	35
3.5	Fourth order fit . . . . .	38
3.6	Slit masks . . . . .	40
3.7	Slits method . . . . .	40
3.8	Slits measurement sketch . . . . .	41
3.9	beam picture . . . . .	42
3.10	Filtered beam and distribution . . . . .	42
3.11	Emitance measurement results . . . . .	45
3.12	Initial beams in the IBL . . . . .	46
3.13	IBL divided in sections . . . . .	49
3.14	Section 1 of the IBL . . . . .	49
3.15	Dispersion for section 1 . . . . .	50
3.16	Section 2 of the IBL . . . . .	51
3.17	IBL simulation . . . . .	53

4.1	Dipole magnet cross section fields . . . . .	56
4.2	Trajectory in dipole magnet . . . . .	57
4.3	GEANT4 simulation results for 45 MeV protons. . . . .	59
4.4	COSY simulation . . . . .	60
4.5	Orbit bump . . . . .	62
4.6	Orbit bump angle and amplitude . . . . .	63
4.7	Orbit bump sketch . . . . .	63
4.8	Short term admittances . . . . .	65
4.9	Orbit bump acceptance . . . . .	65
5.1	Phase space matching 1 . . . . .	68
5.2	Phase space matching 2 . . . . .	69
5.3	Momentum compaction measurement . . . . .	71
5.4	Measured COSY orbit . . . . .	72
5.5	Measured foil current . . . . .	73
5.6	Measured COSY intensity . . . . .	74
5.7	Injection efficiency . . . . .	74

# List of Tables

2.1	Variables used in the Bethe-Bloch formula 2.46. . . . .	26
3.1	Emittance results for <b>quadrupole scan method</b> . . . . .	39
3.2	Emittance results for <b>slit scan method</b> , where $u$ represents any of the coordinates $x$ or $y$ . . . . .	44
3.3	Twiss parameters at the beginning of the IBL. . . . .	46
3.4	Results for IBL optimization. . . . .	52
4.1	Results of the steerer calibration for $H^-$ beams. . . . .	58
4.2	Results of GEANT4 simulations for the stripping foil. . . . .	59
4.3	Results for optimization of the last section in the IBL. . . . .	61
5.1	IBL quadrupole strengths for $\beta$ , $\alpha$ , $D$ and $D'$ matching in the strip- ping foil. . . . .	68



# Bibliography

- [1] COSY-WASA collaboration, *Results on  $\eta/\eta'$  Decays from Hadron Machines*, Nucl.Phys.Proc.Suppl. (2008), pp. 181-182 and 221-225.
- [2] S. Barsov *et al.* *ANKE, a New Facility for Medium Energy Hadron Physics at COSY-Jülich*, NIM A 462 (2001), p. 364.
- [3] Hauenstein, F., *et al.* *Measurement of polarization observables of the associated strangeness production in proton proton interactions*, The European Physical Journal A 52.11 (2016), p. 337.
- [4] B. Sigfrido, D. A. C. Ciofi and G. Mauro, *Perspectives In Nuclear Physics At Intermediate Energies - Proceedings Of The Conference*, World Scientific (1996), p. 545.
- [5] Laurent Canetti, Marco Drewesb and Mikhail Shaposhnikov, *Matter and antimatter in the universe*, New J. Phys. 14 (2012).
- [6] A. D. Sakharov, JETP Lett.-USSR 5 (1967), pp. 24.
- [7] L.H. Thomas, *The kinematics of an electron with an axis*, Phil. Mag. 3 (1927) p. 1.
- [8] V. Bargmann, Louis Michel, and V. L. Telegdi, *Precession of the Polarization of Particles Moving in a Homogeneous Electromagnetic Field*, Phys. Rev. Lett. 2 (1959), p. 435.
- [9] J. Pretz, *Measurement of permanent electric dipole moments of charged hadrons in storage rings*, Hyperfine Interactions, 214 (2013), pp. 1-3.
- [10] R. Maier, *Cooler synchrotron COSY- performance and perspectives*, NIM A 390, (1997) p. 1.
- [11] R. Gebel, O. Felden, R. Maier and P. von Rossen, *Negative ion sources at the injector cyclotron for the cooler synchrotron COSY/JULICH*, Proc. Cyclotrons 2004, Tokyo, Japan (2004), p. 287.
- [12] M. Bai, O. Felden, R. Gebel and H.P. May†, *Status of the COSY/JULICH injector cyclotron JULIC*, Proceedings of Cyclotrons 2016, Zurich, Switzerland.
- [13] W. Haeberli, *Sources of Polarized Ions*, Nuclear instruments and Methods 62, (1968) p. 355.

- [14] R. Weidmann *et al.* *The polarized ion source for COSY*, Review of Scientific Instruments 67, 1357 (1996).
- [15] O. Felden, R. Gebel and R. Maier, *The COSY/JULICH polarized  $H^-$  and  $D^-$  ion source*, Polarized Sources, Targets and Polarimetry (2011), pp. 23-30.
- [16] H. Jungwirth,  *$H^-$  operation of the cyclotron JULIC as injector for the cooler synchrotron COSY-JULICH*, Proceedings of the 15th International Conference on Cyclotrons and their Applications, Caen, France.
- [17] M. Seidel, *Introduction to cyclotrons*, WE-Heraeus-Seminar on accelerator physics for intense ion beams, Bad Honnef (2001).
- [18] K. Strijckmans, *The isochronous cyclotron: principles and recent developments*, Computerized Medical Imaging and Graphics 25 (2001), pp. 69-78.
- [19] P. Brautigam *et al.* *Commissioning of the injector complex of COSY-Julich*, IKP Annual report 1992, p. 233.
- [20] P. Jahn, R. Maier, J. Reich and M. Rogge, *The injection beam line*, IKP Annual report 1991, p. 262.
- [21] H. Labus, J. Dietrich, N. Dolfus and R. Maier, *Measurement of the COSY injection energy*, IKP Annual report 1991, p. 264.
- [22] R. Maier *et al.* *Commissioning of the cooler synchrotron COSY*, Proceedings of the 14th International Conference on Cyclotrons and their Applications, Cape Town, South Africa.
- [23] J. Bojowald *et al.* *Beam diagnostics for COSY*, IKP Annual report 1990, pp. 181-182.
- [24] D. Sagan, *The Bmad reference manual*, internal communication with C. Weidemann.
- [25] S. Agostinelli *et al.* *Geant4 - A simulation toolkit*, Nucl. Instr. and Meth. A506 (2003), pp. 250-303,
- [26] K. Wille, *The physics of particle accelerators: an introduction*, Oxford University Press (1996).
- [27] S. Y. Lee, *Accelerator physics*, World Scientific, second edition.
- [28] H. Widemann, *Accelerator optics*, Springer, third edition.
- [29] W. Magnus, S. Winkler, *Hill's Equation*, Dover-Phoenix Editions.
- [30] J. Liouville, Journ. de Math. 3 (1838).
- [31] J. D. Jackson, *Classical Electrodynamics*, Wiley, Third Edition.
- [32] M. Tanabashi *et al.* *Particle Data Book*, Phys. Rev. D 98 (2018).
- [33] F. Hinterberger and D. Prasuhn, *Analysis of internal target effects in light ion storage rings*, Nucl. Inst. and Meth. A279 (1989), pp. 413-422.

- [34] J. Pfeidder and G. Riepe, *COSY Stripping Target*, IKP Annual report 1991, p. 254.
- [35] J. Stein and C. Weidemann, *R-matrix for the COSY injection dipole magnet*, internal communication with J. Stein.
- [36] M. Syphers, *Emittance dilution effects*, Handbook of Accelerator Physics and Engineering, pp. 280-281.
- [37] A. T. Green and Y. M. Shin, *Implementation of Quadrupole-Scan Emittance Measurement at Fermilab's Advanced Superconducting Test Accelerator (ASTA)*, 6th International Particle Accelerator Conference.
- [38] R. Spesyvtsev, *Implementation of Quadrupole-Scan Emittance Measurement at Fermilab's Advanced Superconducting Test Accelerator (ASTA)*, TESLA-FEL Report (2009).
- [39] Min Zhang, *Emittance Formula for Slits and Pepper-pot Measurement*, No. FNAL-TM-1988, Fermi National Accelerator Laboratory.
- [40] M. Minty, *Diagnostics II*, CERN accelerator school, Sept. 2004.
- [41] C. Runge, *Ueber die numerische Auflösung von Differentialgleichungen*, Math. Ann. 46 (1895), pp. 167–178.
- [42] H. J. Stein, G. Krol, S. Barsov and V. Koptev, *Application and methodological improvements to the floating-wire technique to characterize the magnetic properties of a spectrometer dipole*, Review of scientific instruments, 72 (2001).
- [43] L. Landau, *On the energy loss of fast particles through ionisation*, J. Phys. USSR 8 (1944) p. 201.
- [44] H. Beuscher et al. *The characteristics of the cyclotron JULIC as injector for COSY*, Proceeding of the 12th int. conf. on cyclotrons and applications, Berlin (1989).
- [45] D. Möhl, *Techniques of energy changing and energy monitoring of cooled stored beams*, CERN-PS 85-5 LEA.
- [46] L. H. A. Leunissen, *Non-linear transverse dynamics at the Cooler Synchrotron COSY*, PhD thesis, 1997.
- [47] G. Farren and R. Tolle, *COSY injection simulations*, internal communication with R. Tolle.



### **Selbstständigkeitserklärung:**

Ich versichere, dass ich die Arbeit selbstständig verfasst und keine anderen als die angegebenen Quellen und Hilfsmittel benutzt sowie Zitate kenntlich gemacht habe.

\_\_\_\_\_  
Datum

\_\_\_\_\_  
Unterschrift

### **Statement of authorship:**

I hereby certify that I have done this work independently and without the use of any aids other than those specified. All parts which are taken literally or analogously from published and not published writings of others, are marked as such.

\_\_\_\_\_  
Date

\_\_\_\_\_  
Signature